# A Study of Thin Magnetic Films of Iron Oxides and Yttrium Iron Garnet

By:

Aliaa M. Zaki

*A thesis submitted in partial fulfilment to the requirements for the degree of Doctor of philosophy*

**University of Sheffield**

**Faculty of Science**

**Department of Physics and Astronomy**

July, 2018

# Abstract

The structural, magnetic and magneto-optical properties of iron oxides (wustite, magnetite, Hematite and maghemite), yttrium iron garnet (YIG) and calcium doped YIG (Ca:YIG) thin films prepared by pulsed laser deposition (PLD) technique were studied. The properties of iron oxides films grown on sapphire substrate were found to be dependent on the annealing temperature of the target and the oxygen pressure ($P_{O2}$) during the ablation. For example, the high annealing temperature of the target and base pressure give wustite, whereas a lower annealing temperature with same oxygen pressure and conditions give magnetite. In addition, the fraction of $Fe^{3+}$ ions increases with increasing the oxygen pressure, which leads to pure maghemite at $P_{O2}$ more than 100 mTorr.

YIG thin films were grown on gadolinium gallium garnet (GGG) and yttrium aluminium garnet (YAG) substrates. The GGG substrate was found to cause a lower lattice strain ($\varepsilon$= 0.016%) in YIG lattice compared to YAG substrates ($\varepsilon$=1.12%). The oxygen pressure was also found to affect the magnetic and magneto optical properties of YIG thin films. For example, YIG/GGG films prepared at $P_{O2}$ =400 mTorr were found to have magnetic properties close to bulk YIG with saturation magnetisation ($M_{s=}$ 143 emu/cm$^3$) and coercive field ($H_c$) <1 Oe. These insights were used to prepare Ca:YIG thin films. The Ca:YIG films showed an increase in the oxygen vacancies, a decrease in $M_s$ and high strain; with increasing the amount of doped $Ca^{+2}$ ion. It also found that all the Ca:YIG/GGG films contain about 5% $Fe^{2+}$ at this $P_{O2}$. For example, the film that contains $x$=0.05 has a reduction in the magnetisation of about 18% from the pure YIG/GGG thin film. Lower $P_{O2}$ led to the occurrence of $Fe^{2+}$ ions in the tetrahedral sites of YIG and increased the oxygen vacancies that reduced $M_s$.

# Dedication

To the light of my life, my first teacher whom believed I can do it, my mother

“Anwar”

To the memory of my father whom gave me motivation

“Majid”

To the memory of the smart woman whom I still miss, my grandmother

“Aliah”

# Acknowledgments

I would like to express my deepest gratitude to my supervisor Professor Gillian Gehring for her encouragement, guidance, patience and friendship during the time of this study.

I would like to thank my financial sponsor: University of Baghdad, the Ministry of Higher Education and Scientific Research (MOHESR) and the Iraqi Cultural Attaché in London, who provided me with the funding and support for this work.

I also thank my secondary supervisor Professor A. Mark Fox and Dr. Harry Blythe for their assistance and helpful advice in the experimental work.

I would like to thank Dr. Lisa Hollands from Quarrel Lab/ dept. of Materials Science and Engineering of the University of Sheffield for her help in the annealing process. My thanks also to Dr. Steve Heald of the Argonne national laboratory, USA for his help in XAFS measurements, Dr. Li Xiaoli From Shanxi University, China and Dr. Mannan Ali From E. C. Stoner Laboratory, University of Leeds, for their help in measure the resistivity of Ca:YIG films.

Many thanks also to all my group colleagues Dr. Wala Dizayee, Dr. Hassan Albargi, Fatma Gerriu, Ahmed Saeedi and William Fall, for being friendly and supportive.

I would thank my beloved husband and best friend, Ghaiath, for being encouraging and helpful during these past years. I also thank my little princess; my lovely daughter Noor for bringing me happiness and joy.

I would like to express my greatest thanks to my mother, Anwar, for her patience and support throughout all stages of my life.

I would like also to thank my mother-in-law ‘Iman’, my father-in-law ‘Abbas’, my Grandmother “Adeeba”, my in-laws, my aunts and uncles and their families, my friends and all who immersed me by their love, encouragement, concern and moral support they have shown on me throughout my life.

# Publications

- **Aliaa M. Zaki**, Harry J. Blythe, Steve H. Healed, A. Mark Fox and Gillian A. Gehring. *"Growth of high quality yttrium iron garnet films using standard pulsed laser deposition technique".* Journal of magnetism and magnetic materials 453 (2018): 254-257.
- **Aliaa M. Zaki**, Harry J. Blythe, Steve H. Healed, A. Mark Fox and Gillian A. Gehring. *"Growth iron oxides thin films by pulsed laser deposition technique".* Paper in preparation.
- **Aliaa M. Zaki**, Harry J. Blythe, Steve H. Healed, A. Mark Fox and Gillian A. Gehring. *"Growth of Ca doped YIG thin films in PLD technique*". Paper in preparation.

# Conferences and workshops:

- IoP Postgraduate Magnetism Techniques Workshop, IoP Magnetism Winter School, 12th -13rd of Dec, 2016, University of York, York, UK.
- Aliaa Zaki, Steve M. Heald, Harry J. Blythe, A. Mark Fox and Gillian Gehring, **"Preparation of thin iron oxides films by PLD"**, the IoP Magnetism 2016, 4th-5th of April 2016, University of Sheffield, Sheffield, UK.
- Aliaa Zaki, Steve M. Heald, Harry J. Blythe, A. Mark Fox and Gillian Gehring, **"Preparation of YIG and Ca:YIG thin films"**, the IoP Magnetism 2017, 3rd-4th of April, 2017, University of York, York, UK.
- Aliaa Zaki, Steve M. Heald, Harry J. Blythe, A. Mark Fox and Gillian Gehring, **"Preparation of Ca:YIG thin films by PLD"**, the IoP Magnetism 2018, 9th-10th of April 2018, University of Manchester, Manchester, UK.

# List of abbreviations

Here is a list of abbreviations that used in this thesis:

| | |
|---|---|
| YIG | Yttrium iron garnet |
| Ca:YIG | Calcium doped yttrium iron garnet |
| PLD | Pulsed laser deposition |
| $P_{O2}$ | Oxygen pressure |
| GGG | Gadolinium gallium garnet |
| YAG | Yttrium aluminium garnet |
| m | Magnetic moment |
| A | Area |
| I | Current |
| L | Orbital angular momentum |
| S | Spin angular momentum |
| r | Radius |
| e | Charge of the electron |
| $v$ | Speed of the electron |
| $m_e$ | The electron mass |
| $m_l$ | The orbital magnetic moment |
| $l$ | The orbital quantum number |
| $\mu_B$ | Bohr magneton |
| s | Spin quantum number |
| $g_s$ | g-factor |
| $m_s$ | Spin magnetic moment |
| J | Total angular momentum |
| H | External magnetic field |
| B | Magnetic induction |

| | |
|---|---|
| M | Magnetisation |
| $M_s$ | Saturation magnetisation |
| $H_c$ | Coercive field |
| V | Volume |
| $\chi$ | Susceptibility |
| $\mu$ | Permeability |
| $\mu_0$ | Permeability in free space |
| $\mu_r$ | Relative permeability |
| C | Curie constant |
| N | Number of atoms per unit volume |
| p | Effective magnetic moment |
| $k_B$ | Boltzmann’s constant |
| $\chi_p$ | Pauli paramagnetic susceptibility |
| $T_N$ | Neel temperature |
| $E_F$ | Energy of Fermi level |
| $T_C$ | Curie temperature |
| T | Temperature |
| $\gamma$ | Molecular field constant |
| $\omega$ | Angular frequency |
| $S_i$,$S_j$ | Spin of the nearest neighbour |
| $\omega_q$ | Frequency of spin wave |
| $g(\omega)$ | Density of the states |
| $K_1$, $K_2$ | Anisotropy constant |
| $M_r$ | Remnant magnetisation |
| LPE | Liquid phase epitaxy |
| $\lambda$ | Wavelength |

| | |
|---|---|
| E | Energy |
| XRD | X-ray diffraction |
| $d_{hkl}$ | The lattice plane spacing |
| $hkl$ | Miller's indices |
| $a$ | Lattice constant |
| D | Grain size |
| $\beta$ | The full width at half maximum (FWHM) |
| XAFS | X-ray absorption fine structure |
| XANES | X-ray absorption near edge structure |
| EXAFS | Extend x-ray absorption fine structure |
| SQUID | Superconducting quantum interference device |
| t | Thickness |
| $\tilde{n}$ | Refraction index |
| $n_o$ | Real refractive index |
| k | Extinction coefficient |
| $\alpha$ | Absorption coefficient |
| c | Speed of light |
| $T_s$ | Substrate temperature |
| $T_{ann}$ | Annealing temperature |
| $T_V$ | Verwey transition temperature |
| $T_M$ | Morin transition temperature |
| $\theta_F$ | Faraday rotation |
| $\eta_F$ | Faraday ellipticity |
| MCD | Magnetic circular dichroism |
| $\varepsilon$ | Strain |

# Table of Contents

# 1. Introduction and thesis structure

## 1.1 Introduction:

Magnetic oxides are important materials for electronic applications due to their structural and magnetic properties. They can be divided into three groups: spinels, garnets and hexaferrites. This classification is according to their crystal structure, which can accommodate many cations on different sites [1, 2]. These oxides are used in electronic applications, such as radars, telecommunications and microwave devices [3].

YIG is the most useful oxide due to its unique properties of being a ferrimagnetic insulator [2]. It was discovered by S. Geller and M. A. Gilleo in 1956 [4]. YIG has a high Curie temperature, good chemical stability and the lowest damping of spin waves at room temperature compared to other oxides. It has a low Gilbert damping coefficient ($\alpha$= 2× $10^{-5}$). The spin waves have long life time in YIG due to three main reasons; there are no carriers in YIG, its good crystal property and weak magnetocrystalline anisotropy [5]. Hence, it is an excellent medium for spin wave propagation [6]. A spin wave is the wave resulting from the propagation of disorder in the local magnetic ordering in magnetic materials. It was firstly observed by F. Bloch in 1929 [7]. It is related to the collective excitations of electron spin in ferromagnetic and ferrimagnetic materials [8]. Spin waves are used currently as potential data carriers in computer devices with less than 1 μm wavelength, which provides low frequency and hence; spin information can transfer over macroscopic distances [9]. The characteristics of spin waves are based on two main types of interactions of electron spins coupling, which are strong short distance of exchange interaction and weak long range of dipole-dipole interactions [8]. It is used in a number of devices that are based on microwave signals, such as circulators [12]. Nanometre thickness of YIG films insulators are used in spintronics and magnonics [13, 14].

Spintronics (short for ‘spin electronics’) is an emerging field that takes a benefit of the charge of electrons and their spin to be used to transfer spin in a magnetic material through an electric current [15, 16]. It is a promising solution for data storage applications, such as: magnetic memory, because it provides high speed of data processing, high density of storage and consumes a low amount of energy. These devices use spintronics to store various types of information [17].

On the other hand, ‘magnonics’ refer to transporting information by spin waves, which are mainly related to the magnons associated with the flip of single spin [18]. Magnonics were discovered in 2005 [12] and they provided many advantages for spintronics due to their relation with electron-carried spin current. Figure 1.1 illustrates the transformation between the magnon sub-systems, electron-carried spin and charge currents. This transformation is linked between the magnonics circuitry with electronic and spintronics systems [8, 12].

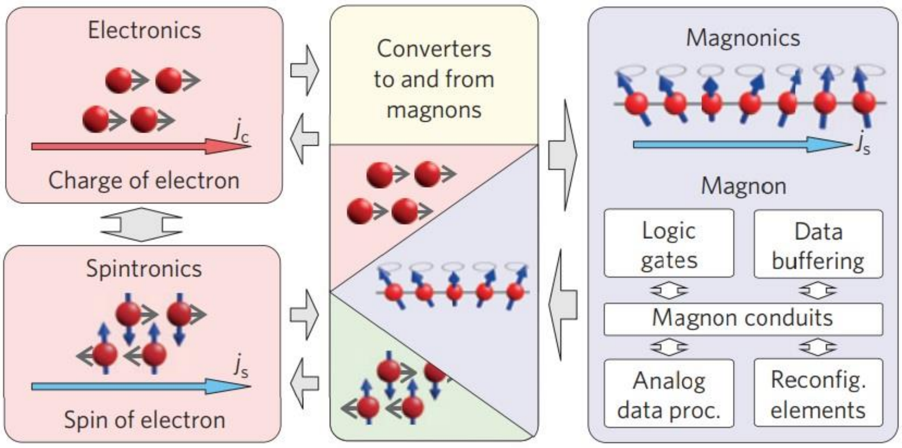

Figure 1.1: The idea of magnon spintronics (magnonics). Reprinted with permission of Journal of Physics D. [12].

Magnons can provide many additional advantages for spintronics. For example, the spin information can be transferred and processed without electrons movement and without generation of heat. The information can transfer with magnons for several micro-distances due to the magnons long free path. In addition, the wave nature of magnons allows producing new and more efficient solutions for data processing [7].

Other than spintronics and magnonics, YIG is also used in ferromagnetic resonance and spin pumping application due to its small ferromagnetic resonance line width [19]. YIG is an insulator with resistivity about $10^{12}$ Ωcm. Therefore, the electron mediated can be transferred only through specific metals; such as platinum (Pt), which has large spin-orbit coupling [6]. In this case, the pure spin current can be generated through spin Hall Effect (SHE). When a charge current passes through normal metal such as Pt, a pure spin current is generated with density of $J_s$. However, to detect the pure spin current that could occur by converting the spin current into a charge current with density of $J_c$ with the direction of transfer. This is called 'inverse spin Hall effect' (ISHE), as shown in fig. 1.2 [20]. These applications require YIG thin films with nanometres thickness range with properties close to bulk YIG properties, such as: $M_s$~143 emu/cm$^3$ and $H_c$ less than 1 Oe.

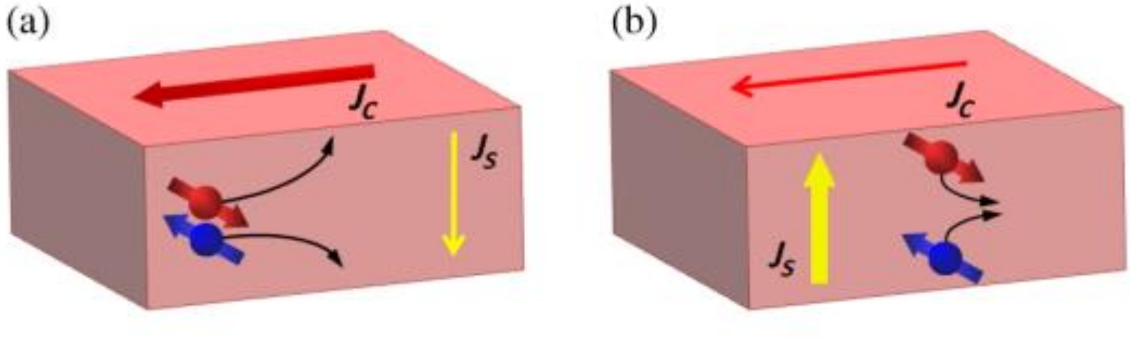

Figure 1.2: (a) Spin Hall Effect (SHE) and (b) Inverse Spin Hall Effect (ISHE). Reprinted with permission of Physical Review Letters [20].

YIG has a wide insulating energy gap ~ 2.86 eV and has non-close packed structure, which allows the substituting of the metal from any site. Hence, it can be doped with variety of magnetic and non-magnetic ions to improve its properties. For instance, YIG is doped with $Bi^{3+}$ ion produces a magneto optical crystal with high Faraday rotation. Bi doped YIG is used as an optical current transformer for the electric current sensor [21].

On the other hand, YIG usually doped with tetravalent or divalent ions to improve its conductivity and produce n-type or p-type magnetic semiconductors with resistivity between $10^2$- $10^4$ Ωcm. In addition to the conductivity, the charge- uncompensated produces electrical charge imbalance that gives interesting properties. For example: the anomaly behaviour of the magnetisation near 0 K and ferromagnetic resonance due to formation of $Fe^{2+}$ at low temperature, when the YIG doped with tetravalent ion or the formation of $Fe^{4+}$ at low temperature, when YIG is doped with divalent ion. To produce n-type magnetic semiconductors, YIG is doped with $Si^{4+}$ [22]. However, to produce p-type magnetic semiconductors, YIG is doped with $Ca^{2+}$ ion. The resistivity was reduced to 100 Ωcm with Ca concentration of 0.4, which made it widely used as an alternative dilute semiconductor.

## 1.2 Thesis structure:

The aims of this thesis are:

- Prepare magnetic oxides thin films by PLD with lower cost and properties close to the bulk sample properties.
- Investigate the structural, magnetic and magneto optical properties of iron oxides thin films that are prepared by pulsed laser deposition (PLD) technique.
- Prepare YIG thin films by PLD with higher quality than previous work. The films are prepared with substrate temperature cooler than the previous work, higher

oxygen pressure during the ablation and higher annealing temperature in air. In addition, study the thin films structural, magnetic and magneto optical properties.

- Prepare p-type semiconductors of Ca:YIG thin films by PLD, which is the first attempt to grow Ca:YIG thin films by PLD technique, and characterize their properties.

This thesis consists of seven chapters (this being chapter one), which are as follows:

- **Chapter two** provides a brief overview of basic concepts and principles of magnetisation. It also includes a brief discussion of exchange interactions and spin waves.
- **Chapter three** lists the experimental techniques that were used in this study and their basic principles. In addition, it details the settings and parameters used in these techniques in this work.
- **Chapter four** describes the preparation of iron oxides thin films and the analysis used to determine their structural, magnetic and magneto optical properties.
- **Chapter five** describes the process of preparing high quality YIG thin films and the results studies of their structural, magnetic and magneto optical properties.
- **Chapter six** investigates the properties of Ca:YIG thin films with different concentrations of $Ca^{2+}$ ions and the effect of their concentration on the structural, magnetic, magneto optical and electrical properties.
- **Chapter seven** is a summary of the main findings of this work and suggested proposals for future studies.

## 1.3 References:

1. Bahadur, D., *Bulletin of Materials Science* **15.5** (1992): 431-439.
2. Mallmann, E. J., Sombra A. S., Goes J. C. and P. B. Fechine. *InSolid State Phenomena, Trans Tech Publications* **202**. (2013): 65-96.
3. Adam, J. D., et al. *IEEE Transactions on Microwave Theory and Techniques* **50.3** (2002): 721-737.
4. Geller, S. and M. A. Gilleo. *Acta Crystallographica* **10.3** (1957): 239-239.
5. Vittoria, C. and N. D. Wilsey. *Journal of Applied Physics* **45.1** (1974): 414-420.
6. d'Allivy Kelly, O., et al. *Applied Physics Letters* **103.8** (2013): 082408.
7. Bloch, Felix. *Zeitschrift für Physik* **61.3-4** (1930): 206-219.
8. Chumak, A. V., et al. *Nature Physics* **11.6** (2015): 453.
9. Chumak, A. V., Alexander A. S., and B. Hillebrands. *Nature communications* **5** (2014): 4700.
10. Cherepanov, V., Kolokolov, I., & L'vov, V. *Physics reports* (1993): 81-144.
11. Serga, A. A., A. V. Chumak, and B. Hillebrands. *Journal of Physics D: Applied Physics* **43.26** (2010): 264002..
12. Stamps, R. L., *et al*. *Journal of Physics D: Applied Physics* **47.33** (2014): 333001.
13. Pirro, P., *et al*. *Applied Physics Letters* **104.1** (2014): 012402.
14. Hahn, C. *et al*. *Appl. Phys. Lett*. **104** (2014): 152410
15. Felser, C., Gerhard H. F., and B. Balke. *Angewandte Chemie International Edition* **46.5** (2007): 668-699.
16. Nikitov, S. A., *et al*. Physics-Uspekhi **58.10** (2015): 1002.
17. Žutić, I., Jaroslav, F., and S. Das Sarma. *Reviews of modern physics* **76.2** (2004): 323.
18. Kruglyak, V.V., Demokritov, S.O., and D. Grundler. "Magnonics." *Journal of Physics D: Applied Physics* **43.26** (2010): 264001.

19. Spencer, E.G., LeCraw, R.C., and C. S. Porter. *Journal of Applied Physics* **29.3** (1958): 429-430.
20. Miao, B. F., *et al*. *Physical review letters* **111.6** (2013): 066602.
21. Hayashi, H., *et al*. *Applied surface science* **197** (2002): 463-466.
22. Antonini, B., *et al*. *Journal of Magnetism and Magnetic Materials* **31** (1983): 149-150.

# 2. Introduction to magnetism and magnetic materials

## 2.1 Introduction:

Magnetic materials are essential in many widely used applications of modern life, such as; power generation, microwave applications, data storage, medical equipment and transportation [1, 2]. To understand the magnetic behaviour of these materials, the magnetic principles and their possible interactions are introduced in this chapter.

The principles of magnetism in this chapter have been obtained mainly from the following text books: “magnetism and magnetic materials” by J. M. D. Coey [3], “Physics of Magnetism and Magnetic Materials” by K. J. Buschow and F. R. D. Boer [4], “Introduction to Solid State Physics” by C. Kittel [5], “Solid State Physics” by J. R. Hook and H. E. Hall [6], “physics of ferromagnetism” by Chikazumi *et al* [7] and “Magnetism in Condensed Matter” by S. Blundell [7].

## 2.2 The Origin of Magnetism:

### *2.2.1 Isolated atoms:*

A magnetic moment results when a current ($I$) moves through a loop with an area ($A$). It is perpendicular to the loop [1-5]:

$$m = IA \tag{2.1}$$

There are three principal types of current that produce a magnetic moment in atoms of a material subjected to an applied magnetic field:

1- The current due to an applied magnetic field, which changes the orbital momentum.
2- The current from the motion of the electron around the nucleus which changes the orientation of the orbital angular momentum, $L$.
3- Intrinsic spin of the electron around itself, S.

The classical model of an atom assumes that there is an internal current due to rotation of an electron around the nucleus in an atom in radius (r); the current will be:

$$I = -\frac{ev}{2\pi r} \tag{2.2}$$

and

$$A = \pi r^2 \tag{2.3}$$

The negative sign in eq. 2.2 is related to the charge of the electron (e), and v is the speed of the electron. By substituting eq. 2.2 and 2.3 in eq. 2.1:

$$m = -\frac{|e|vr}{2} \tag{2.4}$$

Where, $v$ and $r$ are perpendicular to each other. The orbital angular momentum of any electron rotating around the atom is:

$$\vec{L} = m_e vr \tag{2.5}$$

where $m_e$ is the electron mass and:

$$m_e vr = m_l \hbar \tag{2.6}$$

where, $m_l \hbar$ is the orbital angular momentum of a magnetic field ($L$) and $m_l$ are the magnetic quantum numbers. $\hbar = \frac{h}{2\pi}$ where $h$ is Planck's constant. The magnetic moment of electron in term of its orbital angular momentum is:

$$\overrightarrow{m_l} = \frac{-e}{2m_e}\vec{L} \tag{2.7}$$

From the quantum mechanics, the angular momentum of an orbital electron is:

$$L = \frac{lh}{2\pi} = l\hbar \tag{2.8}$$

Where, *l* is the orbital quantum number.

The magnetic moment of electron can be represented as a function of its orbital angular momentum ($m_L$) by substituting equation 2.8 in equation. 2.7

$$\overrightarrow{m_L} = \frac{-el\hbar}{2m_e} = \mu_B\vec{l} \tag{2.9}$$

where $\mu_B$ is known as Bohr magneton and it can be calculated to be:

$$\mu_B = \frac{e\hbar}{2m_e} = 9.27 \times 10^{-24}\, J/T \tag{2.10}$$

In addition, there is another angular momentum, as mentioned above, which is due to the spin of electrons. It is defined by another quantum number called “spin quantum number” (s). The spin angular momentum can be found from $S = \hbar s$.

The electron spin direction is along z-axis and takes the operator value $\hat{S}_z$, which gives the spin magnetic moment *($m_s$)* and takes the eigenvalue of ±1/2 depending on whether it is parallel or antiparallel spin to z-axis. If s=1/2, the eigenvalue of the operator $\hat{S}^2$ will be [7]:

$$\hat{S}^2 = s(s+1) = \frac{3}{4} \tag{2.11}$$

and the spin magnetic moment is:

$$\overrightarrow{m_s} = -g_s\mu_B\vec{s} \tag{2.12}$$

where $g_s$ is a factor termed as "g-factor" of the electron and g=2. Therefore, the spin magnetic moment along the field direction is one Bohr magneton.

### *2.2.2 Hund's rules for atoms:*

Hund's rules are used to explain the lowest energy state of the electrons for the partially filled shell by assuming that the electron-electron repulsion is higher than the spin-orbit coupling. These rules are defined in order of their importance as being:

1- The total spin ($S$) has to be maximized. This means each electron occupies one orbital with a specific spin until all orbitals are half-filled. Then, the next electron shares the orbital as pair to a previously available electron but with an opposite spin. This rule is compatible with the Pauli Exclusion Principle.

2- The maximized value of total atomic orbital momentum ($L$) obtains the lowest energy. This occurs when electrons occupy all the orbitals with same spin. This arrangement reduces the Coulomb repulsion.

3- The total angular momentum ($J$) of atoms of less than half-filled shell is $J=|L\text{-}S|$. However, for the atoms with more than half filled shell; it is $J=|L+S|$. This minimises the spin-orbit coupling energy due to the lower energy when the moments align opposite to each other. The moments aligned parallel to each other lead to higher total energy.

Fig 2.1 illustrates examples of Hund's rules, which are used to calculate the value of $L$, $S$ and $J$ for the ground state of the transition. The figure shows the Hund's rules comparison between vanadium $V^{3+}$ ion, which has less than half full shell, and iron $Fe^{2+}$, which has more than half full shell.

Figure 2.1: The Hund's rules for the ground state of less than half filled shell $V^{3+}$ and more than half filled shell $Fe^{2+}$. Adapted from reference [6]. Courtesy of John Wiley and Sons Ltd.

### *2.2.3 Atoms and ions in solid:*

It is important to understand the role of atomic orbitals shape on materials. The shape of the atomic orbitals determines the distribution of the electrons in the molecules, which explains the electronic and optical properties of materials. The electrons density for *p* and *d* orbitals depend on the distance from the centre of the atom and the direction as shown in fig. 2.2. *s* orbital has a spherical symmetry while *p* and *d* orbitals depend on the angle. This explains the orbital behaviour in different way due to its non-spherical symmetry. For example *p* orbitals have three possibilities of electrons distribution $p_x$ along *x*-axis, $p_y$ along *y*-axis and $p_z$ along *z*-axis [8].

Figure 2.2: The s,p and d orbitals as a function of angular distribution. Adapted from reference [8]. Courtesy of Oxford University Press.

The crystal field is an electric field produced from neighbouring ions in the crystal. This crystal field depends on the symmetry of the local environment. The octahedral environment is an example, which can be found in many metal oxides transition such as magnetite. The ion metal in the octahedron occupies the centre of octahedral sites and is surrounded by an oxygen ion in each corner. The crystal field, in this case, occurs due to the electrostatic repulsion from the negative orbital (oxygen sites). Fig. 2.3 illustrates the $d$ orbital of octahedral and tetrahedral environments. The $d$ orbital has two groups. The $t_{2g}$ orbitals are $d_{xy}$, $d_{xz}$ and $d_{yz}$ orbitals. The $e_g$ orbitals are $d_{z^2}$ and $d_{x^2-y^2}$ orbitals. In the octahedral environment, the five states of d orbitals are splitting into two groups of states. The three orbitals of $d_{xy}$, $d_{xz}$ and $d_{yz}$ have lower energy and two orbitals of $d_{z^2}$ and $d_{x^2-y^2}$ have higher energy [8]. However, the tetrahedral environment has opposite distribution of state as shown in fig. 2.3.

Figure 2.3: The crystal field and *d* orbitals distribution for (a) octahedral environment and (b) tetrahedral environment [8]. Courtesy of Oxford University Press.

The electronic distribution in orbitals is governed by the crystal field energy. These two energies compete to define the distribution. This should be compared with Hund's rule energies (electron-electron interaction). There are two cases of filling the orbitals if there are 4 electrons or more:

1- Weak-field case that occurs when the pairing energy is higher than the crystal field energy. The electrons will occupy each orbital as single electron and the spin in this case is parallel. Then, another electron will add to the orbital to create a double occupied orbital.
2- Strong-field case, which occurs when the crystal field is higher than the pairing energy. The electron will double occupy in the lower state, which is $t_{2g}$ in the octahedral environment and the spin in this case is antiparallel.

For octahedral environment, it is allowed to add 1, 2, 3, 8, 9 or 10 electrons to the orbitals. However, adding 4, 5, 6 or 7 electrons are an interesting case. For instance, the iron ion $Fe^{2+}$ has 6 electrons of $3d^6$. In weak-field case, one electron will add to each orbital in $t_{2g}$ and $e_g$ states. Four states will be unoccupied and the total spin $S$=2. This case is called “high-spin configuration”. However, in the strong-field case, each orbital in $t_{2g}$ will be occupied by two electrons and the $e_g$ will be unoccupied. This case is called “low-spin configuration” and the total spin is $S$=0.

## 2.3 Magnetism and Magnetic materials:

A material is classified as magnetic according to its response to an applied external magnetic field ($H$). The response of the material is known as the magnetic induction ($B$), which is the flux of the magnetic field ($\varphi$) per unit area ($A$). The total magnetic induction is:

$$B = \mu_o(H + M) \tag{2.13}$$

where $\mu_o$ is the permeability in free space, which is $4\pi \times 10^{-7}$ $Hm^{-1}$. The magnetic moment per unit volume is called the magnetisation ($M$). It is an important factor that indicates the magnetic response of materials and it represents on the total magnetic moments ($m$) of the material per unit volume:

$$M = \frac{m}{V} \tag{2.14}$$

Materials are classified as a magnetic not only according to their magnetisation but also by the variation of the magnetisation with the applied field, which is called susceptibility ($\chi$). The susceptibility could be found from:

$$x = \frac{\partial M}{\partial H}\bigg|_T \tag{2.15}$$

It is related to the permeability of the materials ($\mu$), which is the material response to applied magnetic field.

$$\mu = \frac{B}{H} \tag{2.16}$$

and

$$\mu_r = \frac{\mu}{\mu_o} = 1 + x \tag{2.17}$$

where $\mu_r$ is the relative permeability of the material. Materials can be classified due to the values of its susceptibility into:

### *2.3.1 Diamagnetic materials:*

These materials have negative and small susceptibility values ($\chi$~ $-10^{-5}$) (fig 2.4). When an external magnetic field is applied on a diamagnetic material, the magnetic moments are induced and align opposite to the direction of applied magnetic field. Diamagnetic materials atoms have filled electron shells. Therefore, they have no net magnetic moments. Diamagnetism exists in all materials.

Diamagnetism is temperature independent and the magnetisation has the same value at low and high temperature. Examples of diamagnetic materials are sapphire ($Al_2O_3$) and YAG ($Y_3Al_5O_{12}$).

Figure 2.4: An illustration of diamagnetism with negative susceptibility. Adapted from ref.[9]. Courtesy of University of Birmingham.

### *2.3.2 Paramagnetic materials:*

The susceptibility of paramagnetic materials is positive and usually small ($\chi \sim 10^{-5} - 10^{-3}$) (fig. 2.5). There are three main cases of paramagnetic behaviour:

#### I) Magnetic ions in crystals:

The atoms of these materials have partially filled shells and their magnetic moments are aligned randomly in the absence of external magnetic field (the net magnetisation is zero). When an external magnetic field is applied to the material, the magnetic moments try to align with the direction of the magnetic field and the magnetisation becomes higher than zero.

The susceptibility of the paramagnetic materials is temperature dependent due to the competition between the magnetic moment alignment effect in same direction of the field and the thermal disorder. When temperature is increased; the susceptibility and magnetisation decrease. This relation in low field is given by Curie's law:

$$x = \frac{C}{T} \qquad (2.18)$$

where $C$ is Curie's constant of the materials:

$$C = \frac{Np^2\mu_B^2\mu_o}{3k_B} \tag{2.19}$$

$$p^2 = g^2J(J+1) \tag{2.20}$$

where $N$ the number of atoms per unit volume, $p$ is the effective magnetic moment and $k_B$ is Boltzmann's constant ($k_B$= 1.38X $10^{-23}$ J/K).

Figure 2.5: An illustration of the Paramagnetism's magnetic moments and susceptibility. Adapted from ref.[9]. Courtesy of University of Birmingham.

### II) Pauli paramagnetic:

This case is for the metals when each state can be occupied by two electrons. Each electron has spin up or down. If an external magnetic field is applied on a metal, the energy of the electron will be increased or decreased according to its spin. Then, the paramagnetic susceptibility of the electron will increase. In the present of the external magnetic field, the electron band split into two sub-bands and the difference between them is $(g\mu_B B)$, where

$g$=2, as shown in fig. 2.6. The energy of the splitting is very small and Pauli paramagnetic susceptibility ($\chi_p$) is:

$$\chi_P = \frac{3N\mu_o\mu_B^2}{2E_F} \qquad (2.21)$$

where $E_F$ is Fermi energy. From equation 2.21, the susceptibility of the metal is temperature independent. The Pauli paramagnetism is weak and smaller than the paramagnetism in insulators because one electron at least in the magnetic atom insulator participates. However, only electrons which are close to Fermi surface; can contribute in a metal. Example of paramagnetic metals: Na and Al.

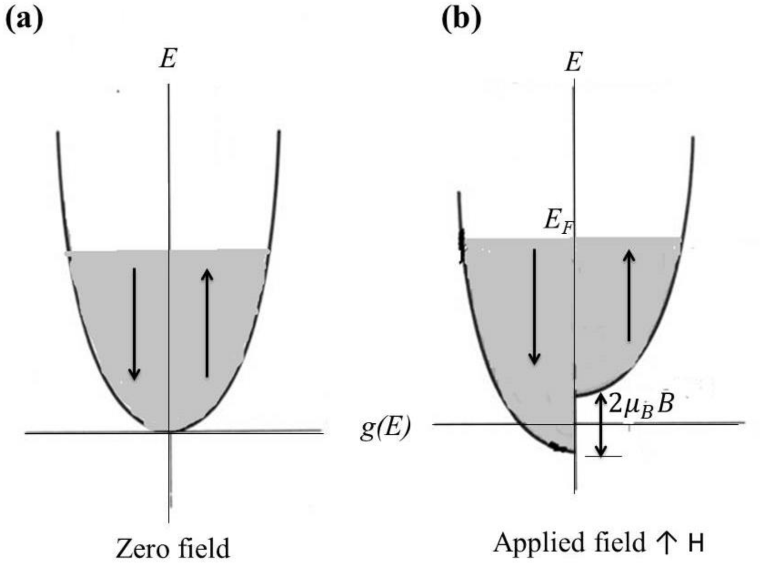

Figure 2.6: The density of states in free electron gas (a) with no applied magnetic field and (b) with applied magnetic field parallel to the spin up magnetic moments. Adapted from ref [10]. Reprinted with permission of Cambridge University Press.

**III) Antiferromagnetic and ferromagnetic order:**

Many paramagnetic materials deviate from Curie's law and follow Curie-Weiss law, which is used when the moments interact antiferromagnetically. Curie-Weiss law is given by:

$$x = \frac{C}{T+\theta} \qquad (2.22)$$

where $\theta$ is a Weiss temperature where below it; the material behaves as antiferromagnet. Above a specific temperature known as 'Neel temperature' ($T_N$), the material behaves as a paramagnetic material but its susceptibility increased with decreasing the temperature and can be found from Curie-Weiss law:

The negative $\theta$ used due to anti-align of magnetic moments as shown in fig. 2.10 and $\theta \geq T_N$. These cases both are above ordering temperature. Below ordering temperature is discussed in §2.3.4. An example of a paramagnetic material at room temperature is GGG ($Gd_3Ga_5O_{12}$).

### *2.3.3 Ferromagnetic materials:*

Ferromagnetic materials have a large positive susceptibility ($\chi \sim 50 - 10000$) and shows hysteresis loop (figure 2.7), which is discussed in detail in §2.8. In the presence of an external magnetic field; the majority of magnetic moments align in the direct of the applied magnetic field. In the absence of the magnetic field; the neighbouring magnetic moments align in the same direction. This means that a ferromagnetic material has a spontaneous magnetisation. Examples of ferromagnetic materials are iron, nickel and cobalt. These materials have unfilled d-shells.

Figure 2.7: An illustration of the parallel alignment of the magnetic moments in ferromagnetic materials and their susceptibility. Adapted from ref [9]. Courtesy of University of Birmingham.

These materials have 4$s$ and 3$d$ partially filled bands. $s$ bands have parabolic structure and the electrons in these bands are delocalized (their mobility is high). However, $d$ bands have flat structure and the electrons in these bands are localized.

In the absence of applied magnetic field, a small number of electrons with spin down in region of energy $(E_F - \delta E)$ flip and place the spin up bands above Fermi level with energy of $(E_F + \delta E)$, as illustrated in fig. 2.8. In this case, the number of spin up electrons (majority) increased whereas, the spin down decreased (minority). This unbalance between the number of electron with spin up $(n\uparrow = \frac{1}{2}(n + g(E_F)\delta E))$ and the number of electrons with spin down $(n \in\downarrow = \frac{1}{2}(n - g(E_F)\delta E))$ increases the magnetisation where:

$$M = \mu_B(n\uparrow - n\downarrow) \tag{2.23}$$

If the Coulomb's energy $Ug(E_f) \geq 1$, the material will have spontaneous ferromagnetism. This condition for spontaneous ferromagnetism is called 'the Stoner criterion'. When an external magnetic field is applied, the *d* band will split and this affects the magnetisation. In ferromagnetic metals, the responsible of the magnetic properties is 3$d$ bands because weak exchange interaction in 4$s$ bands led to a balance in the spins up and down distribution.

Figure 2.8: Density of states in ferromagnetic metal in the absence of applied magnetic field. Adapted from ref [7]. Courtesy of Oxford University press.

The susceptibility of a ferromagnetic material is temperature dependent and for every ferromagnetic material there is a specific temperature known as the 'Curie temperature' ($T_C$). Below this $T_C$, magnetic moments align parallel and the material behaves ferromagnetically. On the other hand, the material exhibits a paramagnetic behaviour above $T_c$ due to the thermal fluctuation that disturbs the parallel alignment of magnetic moments. The susceptibility is given by the Curie-Weiss law:

$$x = \frac{C}{T - T_c} \tag{2.24}$$

### *2.3.4 Antiferromagnetic materials:*

The susceptibility of these materials is small, positive and temperature dependent. Antiferromagnetic materials have no net spontaneous magnetisation due to their magnetic moments where half of them align parallel to the direction of applied magnetic field and exactly half of them align to the opposite direction, as shown in fig.2.9. This arrangement of magnetic moments can be observed below Neel temperature ($T_N$). These magnetic moments are divided into two sublattices A and B. Examples of antiferromagnetic materials: wustite (FeO) and hematite (α-$Fe_2O_3$).

Figure 2.9: An illustration of the anti-parallel alignment of the magnetic moments in antiferromagnetic materials and their susceptibility. Adapted from ref.[9]. Courtesy of University of Birmingham.

Fig. 2.10 shows that there is a phase transition at $T_N$ in the antiferromagnet. Below $T_N$, the susceptibility starts decreasing. In addition, it depends on the angle between the magnetisation of the two sublattices and the direction of the external magnetic field. If the magnetic field is parallel to the magnetisation of A sublattice ($M_A$), $M_A$ will increase with increasing the magnetic field while the magnetisation of B sublattice ($M_B$) will decrease accordingly (as shown in fig 2.11).

$$M = M_A - M_B \tag{2.25}$$

The overall susceptibility of the antiferromagnetic material can be found from:

$$x_{\parallel} = \frac{2Nm^2B\prime(J,\alpha)}{2K_BT+Nm^2\gamma B\prime(J,\alpha)} \tag{2.26}$$

Where, $N$ is the number of atoms per unit volume, $B^{'}$ is the derivative of the Brillouin function and $\gamma$ is the molecular field constant.

If an external magnetic field is applied perpendicular to the magnetisation, the magnetic moments rotate (see fig. 2.11) and the susceptibility will be:

$$x_{\perp} = \frac{1}{\gamma} \tag{2.27}$$

According to equation 2.26, the susceptibility of antiferromagnetic materials is constant. The total susceptibility of polycrystalline antiferromagnetic materials ($\chi_p$) below $T_N$ is shown in fig. 2.11 and can be found through:

$$x_P = \frac{1}{3}x_{\parallel} + \frac{2}{3}x_{\perp} \tag{2.28}$$

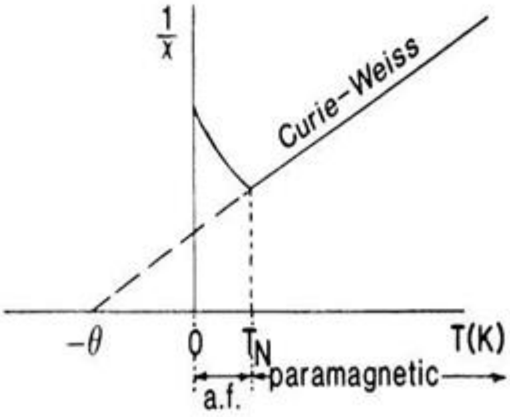

Figure 2.10: The temperature dependence of the susceptibility in antiferromagnetic materials [10]. Reprinted with permission of Cambridge University Press

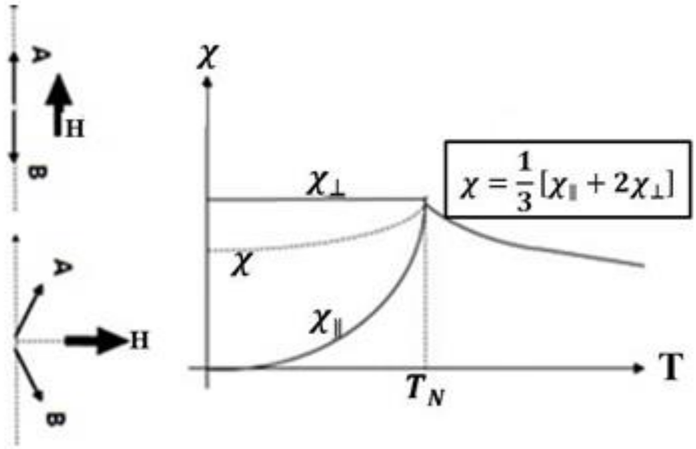

Figure 2.11: The parallel and perpendicular susceptibility in antiferromagnetic materials below $T_N$ [10]. Reprinted with permission of Cambridge University Press

### *2.3.5 Ferrimagnetic materials:*

Ferrimagnetism links the antiferromagnetism and ferromagnetism phenomena. It represents two sublattices with moments opposite to each other similar to antiferromagnets. However, the total magnetisation is not zero due to higher magnetisation in one sublattice than the other. This difference in the magnetisation creates a spontaneous magnetisation similar to ferrimagnets below $T_C$ even in the absence of the external magnetic field. The curve of ferrimagnet magnetisation is different from ferromagnet magnetisation as shown in fig. 2.12.

The ferrimagnetic materials become useful for many applications that require insulator materials with high saturation magnetisation ($M_s$). Examples of ferrimagnetic materials are magnetite ($Fe_3O_4$), maghemite ($\gamma$-$Fe_2O_3$) and YIG ($Y_3Fe_5O_{12}$).

Figure 2.12: The susceptibility and magnetisation of (a) ferromagnetic materials compared to these of (b) ferrimagnetic materials [11]. Courtesy of University of Liverpool.

## 2.4 Energy of a magnetic system:

There are four main energies that determine the behaviour of a magnetic system, which the system tries to minimise their total to get to an equilibrium state. These energies are:

1- **Exchange energy (Ee):** this energy results from the long-range ordering force, which is tended to align the magnetic moments parallel to each other even in the absence of applied magnetic field. The exchange energy depends on the alignment of the neighbouring spins. The exchange energy could be calculated from:

$$\mathrm{E_e} = -2\mathrm{J_{ex}} S_{\mathrm{i}} S_{\mathrm{j}} \tag{2.29}$$

2- **Magnetocrystalline anisotropy energy (Ea):** is defined as the required energy to deflect the magnetic moment from its preferred direction. The magnetocrystalline anisotropy can be known through measuring the magnetisation of a sample in different directions. Fig. 2.13 shows the magnetisation curve of magnetite ($Fe_3O_4$), which is has six easy directions along <111>. The hard direction is on <100> and the intermediate along <110>.

The cubic magnetocrystalline anisotropy energy found from:

$$E_a = K_1(\alpha_1^2\alpha_2^2 + \alpha_2^2\alpha_3^2 + \alpha_3^2\alpha_1^2) + K_2\alpha_1^2\alpha_2^2\alpha_3^2. \tag{2.30}$$

Where, $K_1$ and $K_2$ are the anisotropy constants and $\alpha_1$, $\alpha_2$, $\alpha_3$ are the direction cosines, which represent the angles between a certain direction and the crystallographic axes.

Figure 2.13: The magnetic moment of magnetite along easy and hard directions at room temperature [12]. Courtesy of Institute for Rock Magnetism.

3. **The magnetostatic energy ($E_m$):** is the energy creates a magnetic field opposite to the direction of the magnetisation. This field is known as 'demagnetisation field' ($H_d$). The magnetostatic energy can be calculated from:

   $$E_m = \frac{1}{2}\mu_o H_d M \tag{2.31}$$

4. **Zeeman energy ($E_Z$):** this energy is a result of the interaction between the applied magnetic field and the magnetic moments:

   $$E_Z = -\mu_0 MH cos\theta \tag{2.32}$$

   where θ is the angle between H and M.

## 2.5 Direct exchange interaction:

Direct exchange represents the interaction between the electrons of neighbouring atoms with no any intermediate atom. It is has a little importance on magnetic properties due to the direct overlap between orbitals of the neighbouring atoms. Examples for this interaction can be observed in rare earth elements and some transition metals such as Fe. The latter has a direct interaction due to the overlapping of 3d orbitals, which extends further the nucleus.

## 2.6 Exchange interaction in insulators:

The magnetic and electric behaviour of the materials is classified according to the interaction between the atoms or ions. Antiferromagnetic and ferrimagnetic materials are usually insulators such as; YIG or weak conducting materials such as; $Fe_3O_4$. They have no direct exchange [13].

### *2.6.1 Super exchange:*

This mechanism occurs between nearest non-neighbouring magnetic ions where there is non-direct interaction between them. This interaction is mediated by non-magnetic anion between two magnetic ions (fig 2.14). It is common in some oxides and fluorides such as MnO and $MnF_2$. The super exchange interaction occurs when there is unfilled shell of transition metal such as $Mn^{2+}$. The oxygen ion of 2 electrons in *p* orbital mediates the $Mn^{2+}$ ions. There are two types of super exchange interaction depends on the configuration of Mn-O-Mn bonds.

### *2.6.2 Goodenough-Kanamori rules:*

The two types of super exchange are classified by Goodenough-Kanamori rules. These rules depend on the geometry of magnetic ion-anion- magnetic ion. These rules are:

1- If two magnetic ions have lobes of single occupied orbital (such as 3-*d* orbital), which indicate that each other giving large overlap and hopping integrals. The super exchange is antiferromagnetic and strong. In this case, the configurations of the spins are antiparallel. This spins arrangement is preferable due to its lower kinetic energy. The exchange depends on geometry of the angle between M-O-M. If the angle is 180˚, the super exchange is antiferromagnetic, which can be shown in fig. 2.14a.

2- If two magnetic ions have configuration that indicate to be in contact but without overlap integral; the super exchange is ferromagnetic and relatively weak. The configuration of the spins in this case is parallel. The angle between M-O-M is 90˚, which can be seen in fig. 2.14b.

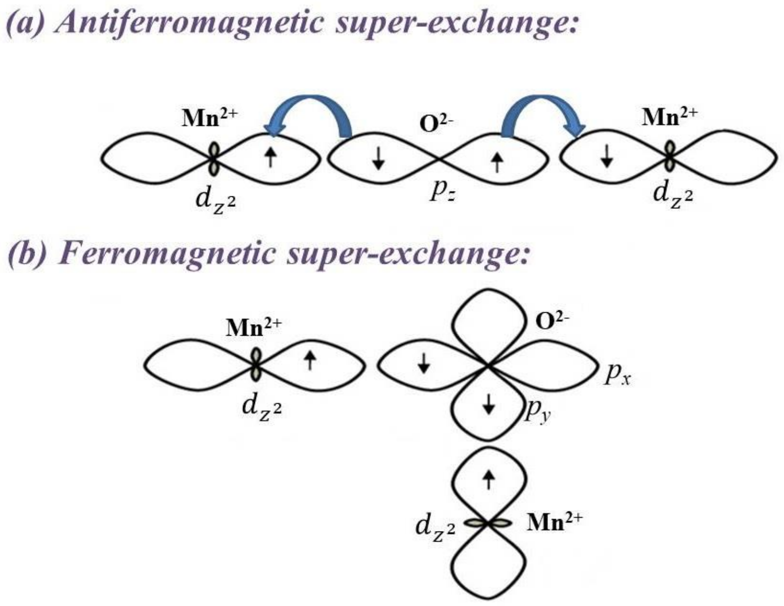

Figure 2.14: The super exchange interaction in MnO as (a) antiferromagnetic (b) ferromagnetic [14]. Reprinted with permission of Journal of Physics D.

## 2.7 Exchange interaction in conductive materials (Double exchange interaction):

Double exchange occurs in some magnetic oxides that have ferromagnetic exchange interaction due to mix valency of the magnetic ions. It occurs in more than one oxidation state. The hopping of an electron occurs when two neighbours of transition metals ions have different number of electrons in the ground state. The double exchange depends on the alignment of the electron spin. According to Hund’s rules (§2.2.1), the electron hops to unoccupied $e_g$ state of $Mn^{4+}$ from $e_g$ state of $Mn^{3+}$ as shown in fig. 2.15. This case occurs if all electrons in $t_{2g}$ state has same spin orientation due to the strong exchange interaction between the spins in $e_g$ and $t_{2g}$ states, which need to be kept in same orientation. In addition, the electron should hop to an unoccupied $e_g$ state as shown in fig 2.15a. However, there is no hopping of the electron, if the electrons of $t_{2g}$ state have anti-parallel orientation, as shown in fig. 2.15b. Ferromagnetic configuration of both neighbours (donating and accepting) is important due to the kinetic energy saving, which is given by the electron hopping and decreases the energy of overlapping.

Figure 2.15: An illustration of (a) the hopping of an electron from $e_g$ state of $Mn^{3+}$ to unoccupied $e_g$ state of $Mn^{4+}$ that can only accept an electron with spin parallel to the occupied $t_{2g}$ state according to double exchange interaction and (b) the case of no electron hopping [7]. Courtesy of Oxford University press.

The double exchange interaction also occurs in magnetite ($Fe_3O_4$). Magnetite contains equal number of both $Fe^{2+}$ ($3d^6$) and $Fe^{3+}$ ($3d^5$) on the octahedral sites (with same number of $Fe^{3+}$ ($3d^5$) in the tetrahedral sites). Those ions have ferromagnetic alignment of double exchange on the octahedral sites. However, the tetrahedral sites have an equal amount of $Fe^{3+}$ ions. These ions coupled with the $Fe^{3+}$ ions of the octahedral sites by antiferromagnetic super exchange interaction.

The difference between super exchange and double exchange interactions is that the super exchange occurs between two ions, which have the same number of valence electrons. On the other hand, double exchange occurs between two ions that have different number of valence electrons.

## 2.8 Spin-waves:

In solid materials, the material is fully ordered at T=0. However, at T≠0; the order is disrupted by the thermal excitation of lattice vibration, which is called a 'phonon'. The phonon describes the relation between the angular frequency ($\omega$) and the wave vector ($q$). In the same roles, the ferro/ferrimagnetic material disrupts its order by spin-wave at $T \neq 0$ and produces a 'magnon'. The producing of magnon requires a small energy. This is an important feature of the spin-waves. If the continuous symmetry of the solid or ferromagnet is broken, there will be a possibility of producing a long-wavelength excitation due to the small vanishingly energy. This excitation is called 'Goldstone mode' or 'bosons'.

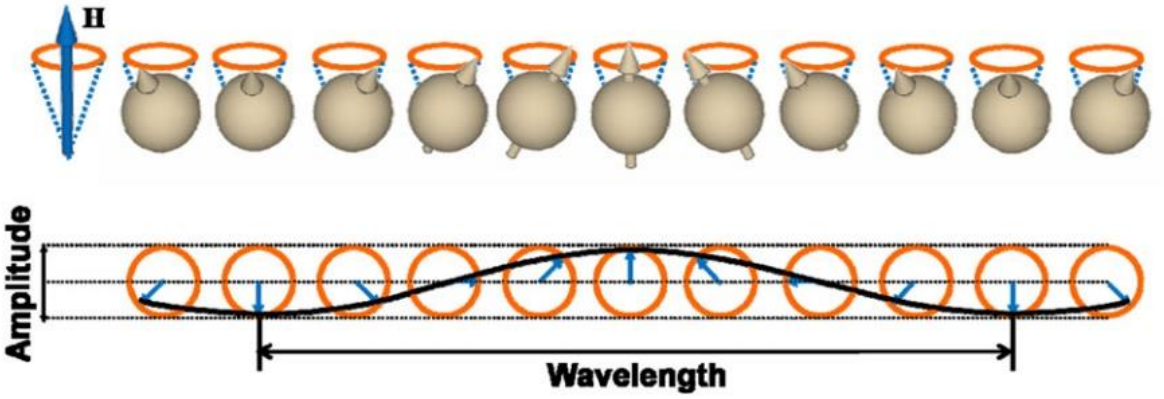

Figure 2.16: A schematic illustration of the spin-wave [15]. Reprinted with permission of Journal of Physics D.

The total exchange energy in the ground state of a ferromagnet per magnetic sites is:

$$E_g = -2z\, J_{ij} S^2 \tag{2.33}$$

where $z$ is the number of the nearest neighbours and $J_{ij}$ is the nearest neighbours exchange interaction. The first excitation from ground state of ferromagnet will flip the spin and the magnetisation will drop from ($M=S$) to $M=(S-1)$ due to reduction of an atomic moment. Classically, the spin-wave dispersion can be found from the Hamiltonian of the Heisenberg model:

$$\hat{H} = -\sum_{\langle ij\rangle} J\hat{S}_i \,.\hat{S}_j \tag{2.34}$$

where $\langle ij\rangle$ is the sum over nearest neighbours. $S_i$ and $S_j$ are the spin of the nearest neighbours. For one dimensional chain, each spin has two neighbours, hence:

$$\hat{H} = -2J\sum_i \hat{S}_i \,.\hat{S}_{i+1} \tag{2.35}$$

The spin $\langle\hat{S}_j\rangle$ can be calculated depends on time:

$$\frac{d\langle\hat{S}_j\rangle}{dt} = \frac{1}{i\hbar}\langle[\hat{S}_j.\hat{H}]\rangle = \frac{2J}{\hbar}\langle\hat{S}_j \times (\hat{S}_{j-1} + \hat{S}_{j+1})\rangle \tag{2.36}$$

By assuming that all the spins in the ground state align along $z$-axis, hence, $S_j^z = S,\ S_j^x = S_j^y = 0$. In addition, assuming there is a state, which is a small departure from the ground states $S_j^z \sim S\ ,\ S_j^x, S_j^y \ll S,$ so:

$$\frac{dS_j^x}{dt} \approx \frac{2JS}{\hbar}\left(2S_j^y - S_{j-1}^y - S_{j+1}^y\right)$$

$$\frac{dS_j^y}{dt} \approx \frac{-2JS}{\hbar}\left(2S_j^x - S_{j-1}^x - S_{j+1}^x\right) \tag{2.37}$$

$$\frac{dS_j^z}{dt} \approx 0$$

The solutions of equation 2.37 are:

$$S_j^x = Ae^{i(qja-\omega t)} \tag{2.38}$$

$$S_j^y = Be^{i(qja-\omega t)} \tag{2.39}$$

where $q = \frac{2\pi}{\lambda}$ and (a) is the interatomic space and $A$= $iB$. Equations 2.38 and 2.39 can be substituted into equation 2.37 and multiply the results to get:

$$\hbar\omega_q = 4JS(1 - \cos qa) \tag{2.40}$$

where $\omega_q$ is the frequency of the spin-waves. The spin-wave dispersion can be calculated from:

$$\lim_{q\to 0} \hbar\, \omega_q \approx D_{sw} q^2 \tag{2.41}$$

Where, $\varepsilon_q = \hbar\omega_q$ and the spin-waves stiffness parameter is $D_{sw} = 2JSa^2$.

The number of magnons can be determined from the density of states, $g(\omega)$, of magnons, so:

$$n_{magnon} = \int \frac{g(\omega)d\omega}{e^{(\hbar\omega/K_B T)-1}} \tag{2.42}$$

Each magnon gives a single reverse spin. This reduces the total magnetisation by 1. This reduction at zero temperature can be found through:

$$\frac{M(0)-M(T)}{M(0)} \propto T^{3/2} \tag{2.43}$$

$T^{3/2}$ is called ‘Bloch $T^{3/2}$ law’ as shown in fig. 2.17, which is experimentally correct at low temperature.

Figure 2.17: The experimental results of the spontaneous magnetisation for ferromagnet by using spin-waves. This curve follows Bloch $T^{3/2}$ law [7]. Courtesy of Oxford University press.

## 2.9 Domains and domain walls:

Ferromagnetic and ferrimagnetic materials are divided in to small magnetic regions known as domains. Each domain has parallel magnetic moments due to the exchange energy (see §2.4). The magnetic moments in different domains in the absence of external magnetic field align in different orientation and the total magnetisation has the lowest value. The magnetic moments of adjacent domains are likely to align in same direction in the presence of an applied external magnetic field [12].

Single domain particles have large demagnetising energy, which is the energy required to remove the magnetic properties of a magnet (see §2.4). Therefore, they magnetically prefer to be divided into several domains to minimise the demagnetising energy. The region at the boundaries of domains is known as the 'domain wall'. The domain walls thickness is in the range 5 nm-10 μm, which depends on the magnetic properties of the materials. In the domain walls, the magnetic moment changes its orientation gradually, as illustrated in fig. 2.18. The magnetocrystalline energy prefers thin domain walls whereas; the exchange energy, which is the energy of two or more electrons with same spin exchange their position in the orbitals and it increases with the number of similar spin electrons. The exchange energy prefers wide domain walls.

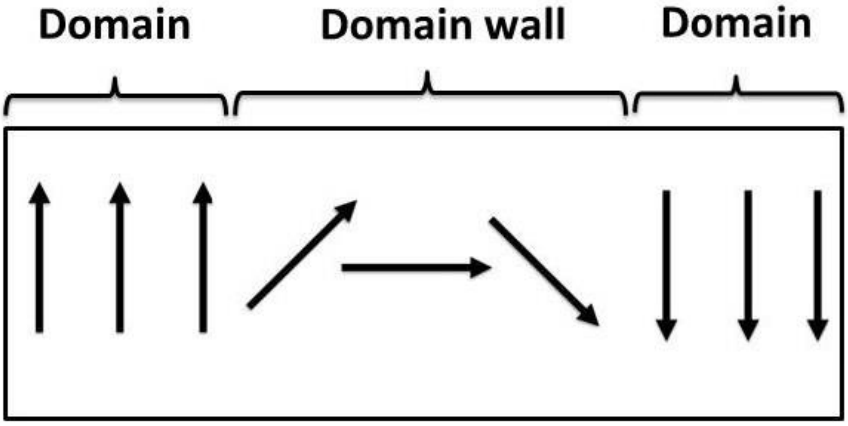

Figure 2.18: An illustration of magnetic moments alignment in domains and domain walls [16]. Courtesy of the University of Sheffield.

## 2.10 The hysteresis loop:

The magnetisation of ferromagnets and ferrimagnets has a non-linear relationship with the applied magnetic field, as shown in fig. 2.19a & b. This relationship is referred to as the ‘hysteresis loop’. When the applied field is increased; the magnetisation increases until it reaches the maximum value of the magnetisation, which is called “saturation magnetisation” ($M_s$). Further increase to the applied magnetic field produces no change to the magnetic structure of the point. When the applied field drops back to zero, the magnetisation does not go back to zero but reaches a special point known as the “remnant magnetisation” ($M_r$), which represents the amount of magnetisation stored in the material after applied field removal. The coercive field ($H_c$) refers to the reverse magnetic field required to return the magnetisation to zero. $M_r$ and $H_c$ are considered as characteristic of ferromagnetic and ferrimagnetic materials. If the magnetic field is removed, the domain structure and domain walls will not retrace back to their original position. Some domains will maintain their orientation and energy. The magnetic materials where domains return to their original structure are called ‘permanent magnet material’. The magnetic field applied in opposite direction is needed in order to remove all the reminding magnetisation [17].

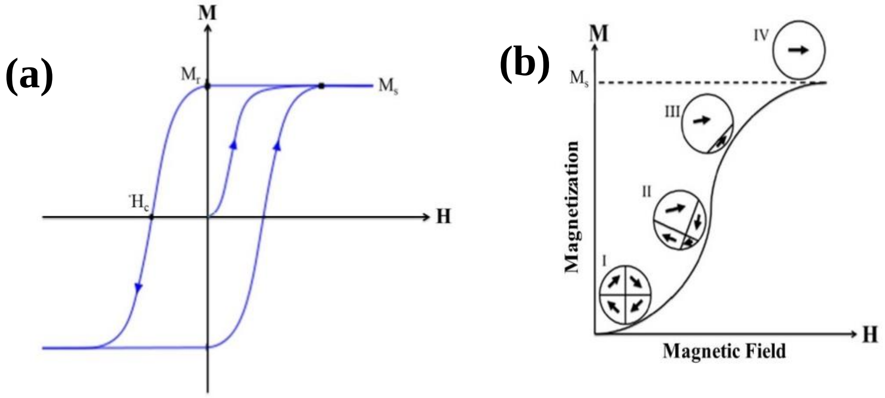

Figure 2.19: (a) The hysteresis loop of ferromagnetic materials and (b) the effect of applied magnetic field on the magnetic domains from $H$=0 until reaching saturation [10]. Reprinted with permission of Cambridge University Press.

## 2.11 References:

1- Jiles, D. “*Introduction to magnetism and magnetic materials”*. CRC press, (2015).

2- O'handley, R. C. “*Modern magnetic materials: principles and applications”*. Wiley (2000).

3- Coey, J. M. “*Magnetism and magnetic materials”*. Cambridge University Press (2010).

4- Buschow, K. H. J., & F. R. Boer. “*Physics of magnetism and magnetic materials”* (Vol. 92). New York: Kluwer Academic/Plenum Publishers (2003).

5- Kittel, C., McEuen, P., & P. McEuen. “*Introduction to solid state physics”* (Vol. 8, pp. 323-324). New York: Wiley (1996).

6- Hook, J. R., & H. E. Hall. Solid State Physics (The Manchester Physics Series) (1991).

7- Blundell, S. “*Magnetism in Condensed Matter*”, 2nd ed. Oxford University press, (2003).

8- Chikazumi, S., and C. D. Graham. “*Physics of Ferromagnetism 2e”*. Vol. 94. Oxford University Press on Demand. (2009).

9- Harris, I. R., and A. J. Williams. "*Material Science and Engineering, Vol. II, Magnetic Materials*". School of *Metallurgy and Materials-University* of Birmingham–Birmingham-UK (2000).

10- Spaldin, N. A. “*Magnetic materials: fundamentals and applications”*. Cambridge University Press, (2010).

11- Bland, J. "*A Mössbauer spectroscopy and magnetometry study of magnetic multilayers and oxides*". (2002).

12- Moskowitz, Bruce M. "*Hitchhiker’s guide to magnetism*". *Environmental Magnetism Workshop (IRM)*. Vol. 279. No. 1. Univ. of Minn., Minneapolis, Minn: Inst. for Rock Magnetism, 1991.

13- Cullity, B. D., and C. D. Graham. “*Introduction to magnetic materials”*. John Wiley & Sons, (2011).

14- Opel, M. *Journal of Physics D: Applied Physics* **45.3** (2011): 033001.

15- Kim, S. *Journal of Physics D: Applied Physics* **43.26** (2010): 264004.

16- Allwood, D., J. Dean, and T. Hayward, ‘*MAT6390 Magnetic materials and devices’*. 2014, University of Sheffield: University of Sheffield, Sheffield, UK.

17- Moskowitz, B. M. "*Hitchhiker’s guide to magnetism*". *Environmental Magnetism Workshop (IRM)*. Vol. 279. No. 1. Univ. of Minn., Minneapolis, Minn: Inst. for Rock Magnetism, (1991).

# 3. Methodology

## 3.1 Introduction:

This chapter details the sample preparation and characterisation methods used in this work. This includes the techniques that were used to measure the thickness and structure measurements which were performed for the thin films. In addition, more details are given for the methods that were used to measure the magnetic and magneto-optical properties of the thin films.

## 3.2 Targets preparation:

All the samples in this work were prepared as thin films through ablation of bulk targets. These targets were prepared by a standard solid state reaction route in Magnetic Oxides group laboratory at the University of Sheffield. Stoichiometric amounts of powders were mixed together for 15 minutes in a mortar and pestle. Then, the powder was annealed in air in a furnace at a specific temperature depending on the materials used for 12 hours (the specific temperature for each of the targets will be detailed later). This grinding and sintering was repeated twice for same period and temperature in order to optimise the reaction of the mixture to form oxide the compound. The powder was pressed to form a pellet at 25000 KPa using a hydraulic press into a disc of 25 mm diameter and thickness of 5 mm. The pellet was annealed again for 15 hours before it was used for ablation in the chamber.

## 3.3 Pulsed laser deposition technique (PLD):

There are many techniques that can be used to prepare iron oxides thin films. The most common techniques are: liquid phase epitaxy (LPE), radio frequency (rf) magnetron sputtering and pulsed laser deposition (PLD). In LPE, grown films are high quality and single-crystal structure but they are not suitable for materials to be used in microwave applications [1]. In addition, it is not possible to grow films with thicknesses less than a few hundred nanometres [1]. Radio frequency magnetron sputtering is a convenient and economical low temperature technique compared with LPE. It can be used to sputter dielectric thin films but with off- stoichiometry due to have oxygen vacancies [2, 3].

PLD is used to grow high quality iron oxides thin films. This technique has several advantages:

- The possibility to control the oxygen pressure in the chamber, which is necessary to produce new materials such as the metastable phase materials and novel device structure [4].
- The stoichiometry of the target can reproduced in the films since all elements are vaporised at the same time according to the high rate of ablation [5].
- Easy to control the thickness of films and ability so films of a few nanometres to few micrometres may be grown [6].
- The using of UV energy of laser cuts chemical bonds.
- Easy to control the process by an independent laser and chamber since the laser source is placed outside the chamber.
- Small cross contamination from other compounds grown in chamber.
- Using energy near the threshold to stop the splashing.

However, the major disadvantage of PLD is “the splashing” or particular deposition. Under the thermal shock, the surface defects are separated. To reduce this effect, the targets used had a high density and were polished before each use [5].

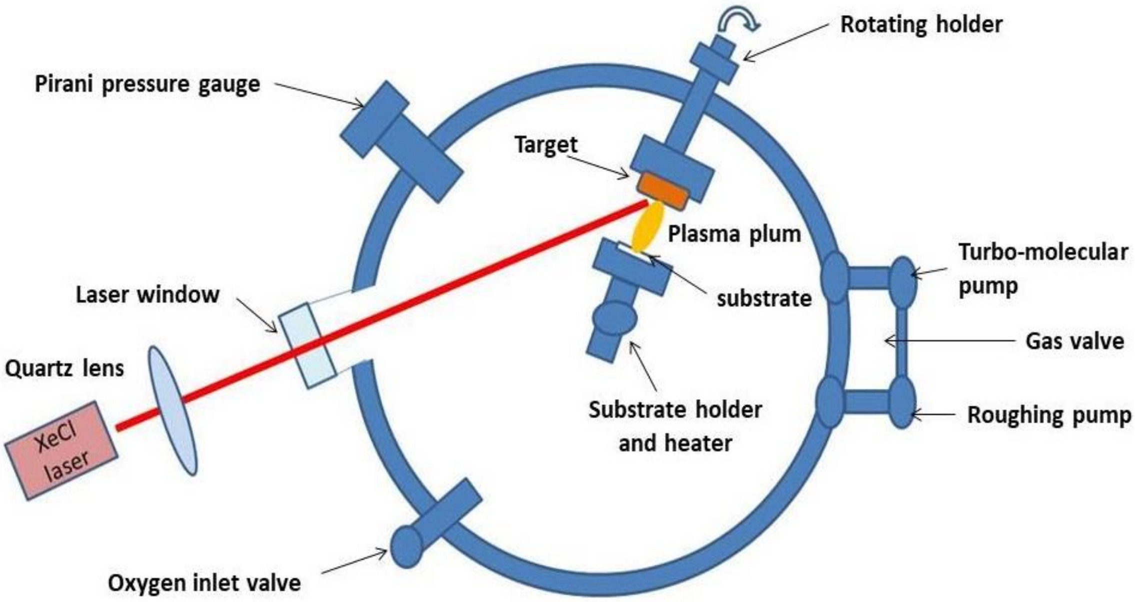

Figure 3.1: A schematic sketch of pulsed laser deposition (PLD) showing the main chamber parts.

The PLD system shown in fig. 3.1 is divided into three main parts:

### *3.3.1 The laser:*

There are four categories of laser sources: solid, gas, chemical liquid and semiconductors with wavelengths ranging from far UV to mid-IR [7].

The Excimer laser is one of the most common molecular gas lasers, which are used in PLD devices [7]. It contains Argon (Ar), Krypton (Kr) or Xenon (Xe), which are all inert gases that are mixed in the excited state with a halogen atom such as, fluorine (F) or chlorine (Cl) to form a gas-halide excimer [7].

The 'Excimer' name comes from two words, excited and dimer. This name comes from the electronic states of excimer gas, which are unstable. The ground state is repulsive with a potential energy curve, hence; the occupation is zero (fig. 3.2). However, the excited state is a metastable bound state. The transition in the Excimer is called 'bound-free transition' because it occurs between upper states [8].

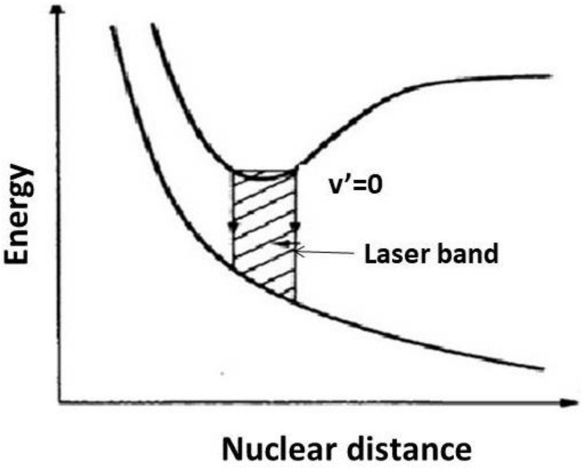

Figure 3.2: Electronic states of Excimer [8]. Reprinted with permission of Springer Nature.

The wavelength of excimer is dependent on the gases contained. For example, ArF (λ= 193 nm), KrF (λ= 248 nm), XeF (λ= 351 nm) and XeCl (λ= 308 nm). All Excimer lasers work in the UV spectral region [8].

In this work, a Lambda Physik LEXTRA 200 excimer laser XeCl (λ= 308 nm) was used to ablate the thin films. The pulsed energy was about 300 mJ with pulsed laser repetition rate of 10 Hz.

### *3.3.2 The optical system:*

The PLD optical system contains a quartz lens. This lens is used to focus the laser beam on a rotating target surface. This lens is mounted on a rail between the laser and the chamber. The light of laser also passes through optical window of the chamber. The incident angle is 45˚ and the spot size of the laser beam about 3 mm$^2$.

### *3.3.3 The deposition chamber:*

The deposition chamber is made from stainless steel and can be evacuated to a base pressure of 10$^{-5}$ Torr. This pressure is controlled by a Baratron in junction with three turbo-molecular pump (TMP) valves: a gas valve, a roughing valve and a gate valve.

The target is fixed on a stainless steel target holder rotated by an external motor. The advantage of the rotation is to protect the target from the damage, which occurs as a result to the laser pulses. If the target is not rotated, a hole will be created in the target. The rotation also decreases the rate of the splashing on to the substrate. The stainless steel substrate holder is mounted at the centre of the chamber and parallel to the target holder. The distance between the target and the holder is about 3 cm. The substrate holder is connected to a Chrome-Alumel thermocouple, which is used to control the substrate temperature during the deposition and it is connected to ice-bath as a reference. The substrate holder contains two wires that are connected to an ammeter and voltmeter as shown in fig. 3.3. The holder is cleaned by acetone before each use to remove any dirt and debris from the previous use.

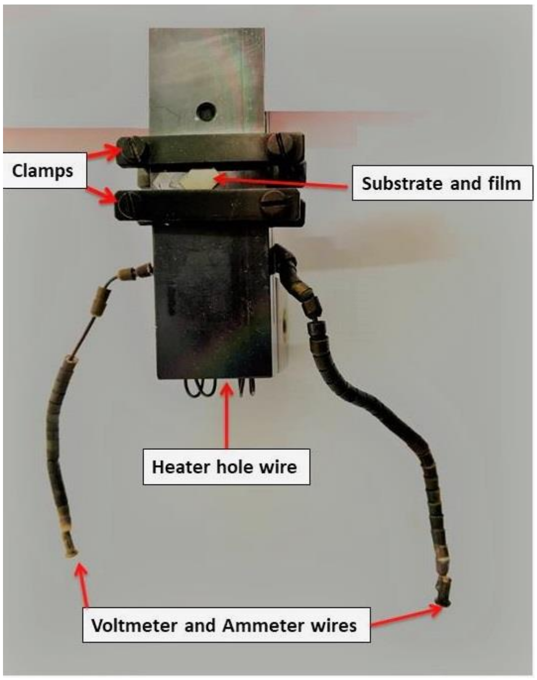

Figure 3.3: A screenshot of the heated substrate holder.

The sample preparation procedure starts by preparing a substrate of 4x4 mm, which was cleaned in an ultrasonic bath and in acetone before it was clamped on the holder by two small clamps as shown in fig. 3.3. These clamps had another advantage, which is to provide a clear area in the substrate after the deposition. This area acts as a reference in measuring the thickness by Dektak, which will be discussed in next section. All the films were grown at a temperature of 500 ˚C.

The continuity of the heater connectors was checked every time before vacuuming the chamber. The chamber was sealed off and pumped down to the base pressure by using the roughing pump and TMP. The two pressure gauges, pirani gauge and penning gauge were used to control the pressure. After the pressure reached $10^{-5}$ Torr, $O_2$ was added to the chamber through a gas-inlet valve in a controlled manner.

When the substrate temperature and the pressure reached the required values, the laser was turned on and the ablation started. The substrate temperature, pressure, laser energy and laser plume quality were monitored and recorded during the ablation process.

The laser beam pulsed at 10 Hz and it hit the rotating target surface. The target surface evaporated in the form of a plasma plume out of the target. This consists of atoms, molecules, ions and electrons. The quality of the plume depends on the laser energy and oxygen pressure. The ablation time depends on the thickness required which is also, affected by the quality of the plasma plume.

When the ablation finished; the film was left to cool down to room temperature, which can take a few hours or can be quenched rapidly. Nitrogen gas was used to vent the chamber to atmosphere pressure in order to release the lid and extract the film.

## 3.4 Dektak surface profile:

Dektak measures the surface shape and texture. It has a stylus that measures the vertical surface profile of the material by measuring the difference of steps on the sample [9]. The stylus contacts with the surface of the sample and moves front and back to measure the difference in sample surface height. It can provide thickness measurements for thin films in the range between 50 nm and 1000 nm [9].

The device is placed in a dark plastic isolation case to prevent any external noise that affects the measurement. The main two parts of the equipment are the scanner, which consists of the stylus (needle) that can move up and down with radius of 2.5 μm. It scans three dimensions. The sample is located on the stage of the device in the correct position and perpendicular to the stylus. When the measurement starts, the stylus starts scanning the thin film in a certain path length, which is determined. The stylus run starts at a clean region, which was covered before and during the ablation. Then, it runs along the thin film to measure the difference between the clear surface and the thin film edge. The error estimated in dektak measurements is around ~10 % [10].

## 3.5 X-ray Diffraction (XRD):

XRD is a technique that can provide information about the crystal structure of materials [11]. When the x-ray beam is applied to a sample, the electric field of the X-ray interacts with the electrons in the atom cores. These electrons oscillate and release X-rays [12]. The diffracted X-rays are collected and the lattice spacing is calculated through Bragg's law [12]:

$$n\lambda = 2d_{hkl}sin\theta \tag{3.1}$$

where n is the order, θ is the angle of diffraction, $d_{hkl}$ is the lattice plane spacing and *hkl* are Miller's indices (illustrated in fig. 3.4). Miller's indices refer to the orientation of the plane in the crystal [12]. The *d* spacing of a plane is dependent on both the Miller indices and lattice constants ($a$, $b$ and $c$) [12]. All the materials studied for this thesis have a cubic structure, which means the $d$- plane spacing can be found through the equation [11]:

$$d = \frac{a}{\sqrt{h^2+k^2+l^2}} \tag{3.2}$$

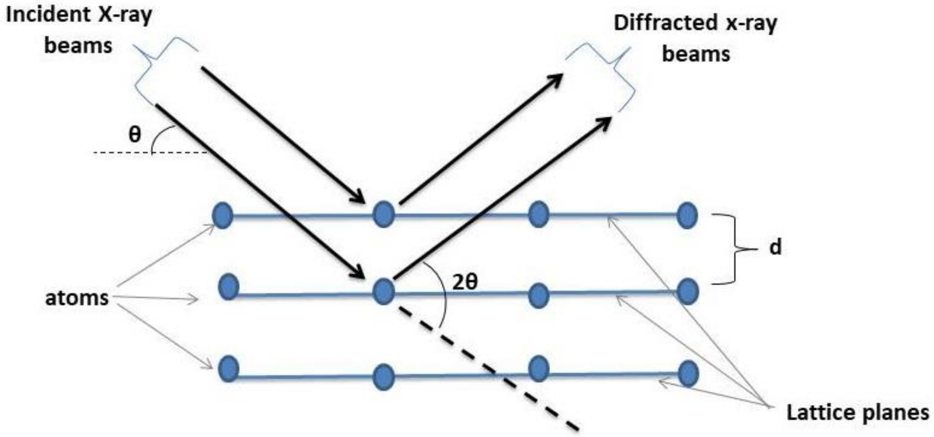

Figure 3.4: A schematic sketch of the interaction of x-ray with matter.

XRD measurements were performed using Bruker D2 phaser device, which has a copper source (Cu Kα) with a wavelength (λ= 1.54 Å). The x-ray was applied to the sample, which was fixed on cleaned stable holder. The diffracted x-ray beam from the sample was collected by a detector to record the intensity of the beam. The angle of the applied X-ray beam was varied between 10˚ to 40˚. The grain size of the films was measured from XRD data by using Scherrer's equation:

$$D = \frac{K\lambda}{\boldsymbol{\beta cos\,\theta}} \tag{3.3}$$

Where, $K$ is a constant related to crystal shape and always taken as 0.94. β is the full width at half maximum (FWHM) of the XRD peak in radian [11].

## 3.6 X-ray absorption fine structure (XAFS):

XAFS is an element specific technique that is used to study the phase purity of thin films since it has a high sensitivity to secondary phases. The measurement output is usually divided into two parts. The first is the x-ray absorption near edge structure (XANES), which provides information about the oxidation states The second part is known as 'extended x-ray absorption fine structure' (EXAFS), which gives information about the coordination environments and the geometry of crystals [13] as shown in fig. 3.5 [14].

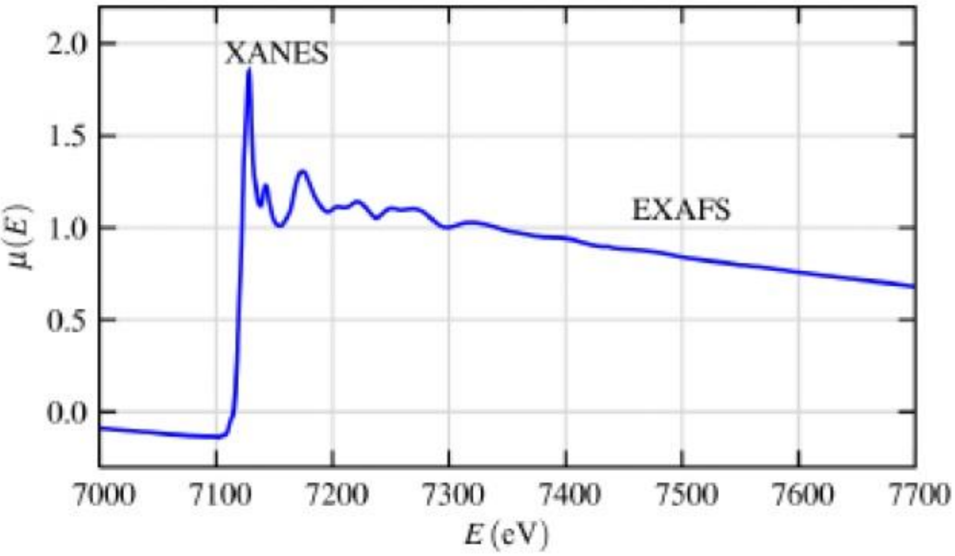

Figure 3.5: Normalised X-ray absorption fine structure (XAFS) spectra of a FeO thin film [14]. Courtesy of Mineralogical Society of America.

If an x-ray beam passes through a homogeneous film of thickness ($t$), the transmitted beam will have an intensity ($I(E)$) of [13]:

$$I(E) = I_o e^{-\mu(E)t} \tag{3.4}$$

Where, $I_o$ is the intensity of the incident x-ray beam and μ(E) is the linear absorption coefficient.

At the absorption edge, the absorption increases when a specific energy of the incident electron is enough to excite the electron from an inner state (1*s*) in K level to an unoccupied state above the Fermi energy level $E_f$ with producing a photoelectron.

EXAFS occurs when x-ray beam applied to an atom in a thin film. The beam is absorbed and the atom releases an electron (as a photoelectric wave) from lower atomic state. This photoelectric wave scatters from the atom and interferes with the leaving part of the photoelectric wave for the nearest neighbour atom [14].

XAFS gives information about crystal structure, the atomic number of the thin film elements, disorder and the thermal motion of the neighbouring atoms. It is divided into two parts according to its energy from edge. XANES is from the edge to 40 eV above the edge and EXAFS is from 40 eV to 1000 eV [13].

All X-ray absorption measurements described in this work were performed at the Advanced Photon Source in Argonne National Laboratory in the USA by Dr. Steve Heald and the data was analysed using Athena analysis program.

## 3.7 Superconducting Quantum Interference Device (SQUID) magnetometer:

A SQUID is a sensitive magnetometer device used to investigate the magnetic behaviour of the material due to its ability to detect small magnetic field [15, 16]. There are two types of the SQUID, direct current (DC) which contains two Josephson junctions (weak-links) parallel in the superconducting loop. The second type is called ‘radio frequency’ (RF) SQUID, which contains a single Josephson junction (weak-link) and this is more popular than the DC SQUID because it is more powerful [17]. All magnetic measurements of this work were performed using a RF SQUID magnetometer model MPMS-5 manufactured by Quantum Design. The measurements can be taken at temperature from 2.5 – 400 K in a magnetic field up to 5 T. In this work, the temperature used was in range of $5<T<300$ K with a magnetic field up to 1 T.

A SQUID measures the voltage induced by a magnetic induction from the sample in a field sensing coil. It consists of a superconducting ring interrupted by a very thin Josephson junction, which works as a resistive and resonant RF circuit [15, 16].

When a magnetic field is applied through the ring at normal temperature (the ring is not superconducting), the magnetic field passes through the ring. However, when the temperature of the ring decreases, the ring will be a superconducting material. The flux ($\phi_o$), which is passing through the ring, will remain restricted due to the induced surface current. This flux equals an integer value of $2.1\times10^{-15}$ $\mathrm{Tm}^2$, which are called ‘fluxons'. That provides the ability of detecting a very small fraction of fluxons. The superconducting ring interrupts by Josephson junction, which is thin resistive region in the ring. The ring can remain superconducting, if the electron pair tunnelled through the junction but the critical supercurrent will reduce to about 50 µA. This critical supercurrent oscillates with the flux [18, 19]. If the current exceeds the critical current, only the flux will pass through the ring and small fraction of the flux quantum will be detected.

When the magnetic field is varied in the system near the inductively coupled field-sensing coil, it will change the critical supercurrent in the junction. As a result, the flux will change. This will cause a damping of the resonance of the RF circuit. The movement of the sample through the pick-up coil changes the flux. This flux change is proportional to the magnetic moments of the sample. The output signal is detected by the SQUID output sensor. The computer program converts the variation in the flux to a magnetic moment [17-19]. The SQUID parts illustrate in fig. 3.6.

Figure 3.6: An illustration of SQUID system parts [20]. Courtesy of Quantum Design, Inc.

### *3.7.1 SQUID operation:*

Thin films samples with dimensions of 4×4×0.5 mm were measured by the SQUID. They were mounted onto an uniform plastic, clean straw by squeezing the sample in the centre of the straw and stitching it or by placing the sample in a gelatine capsule then, wedging the capsule in the centre of the straw. The straw is connected to the brass end of the stainless steel sample holder rod. The length of the holder about 1.5 m, which is introduced into the SQUID via an access port existed at the top of the system. An air lock prevents the atmosphere gasses from contaminating the chamber of the SQUID. The sample is centred in the field-sensing coil, which will enable the magnetic moments to be detected. The scan length used is usually about 2 cm for accuracy.

During the scan, the sample is stepping through a set of pick-up coil, which consists of two wired ring opposite to each other used to remove the external noise and the external magnetic field generated from a superconducting magnet. The field sensor coils set in the form of second order gradiometer. This gives more accurate measurements due its sensitivity to regular field and regular field gradient.

There are two types of measurements performed by the SQUID:

- The hysteresis loop measurement of the sample at constant temperature (5-300K) and the magnetic moments are measured as a function of the magnetic field, which is ramped from 1000 Oe to -1000 Oe and back again during the run. The raw data of the hysteresis loop are measurements shown in fig. 3.7.

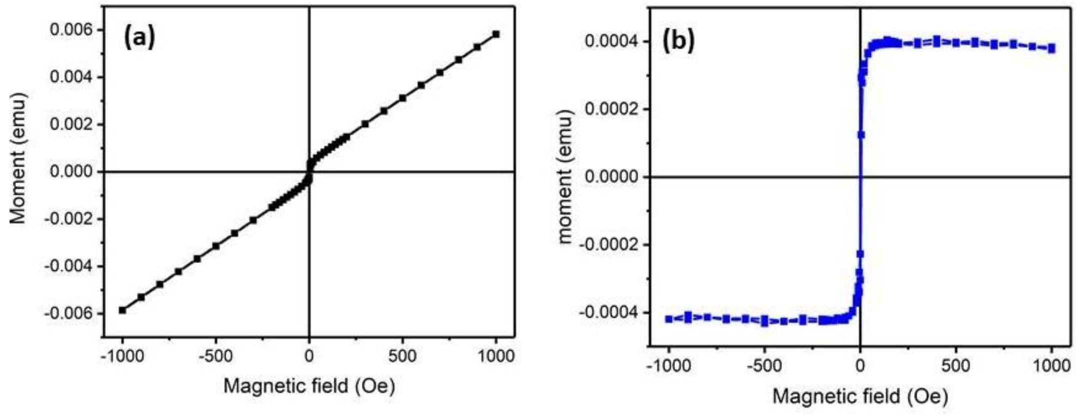

-

Figure 3.7: The hysteresis loop for YIG/GGG thin film at room temperature (a) the raw data and (b) the data after the linear contribution has been subtracted off.

- Zero field cooled and field cooled measurements: are used to measure the magnetic moments as a function of temperature which is varied between 5- 350 K with constant field (in this work usually was about 100 Oe). These measurements tell us if the system is irreversible in the temperature range considered. It works into two steps, as shown in fig.3.8:

1. ZFC: the sample is cooled down to 5K in the absence of the field. Then, when the temperature is stable, a small field about 100 Oe is applied and the magnetic moment measured as a function of the temperature (5-350 K).
2. FC: the sample is cooled down from 350 to 5K in the presence of the small field (100 Oe).

The ZFC and FC measurements are usually measured in a single run.

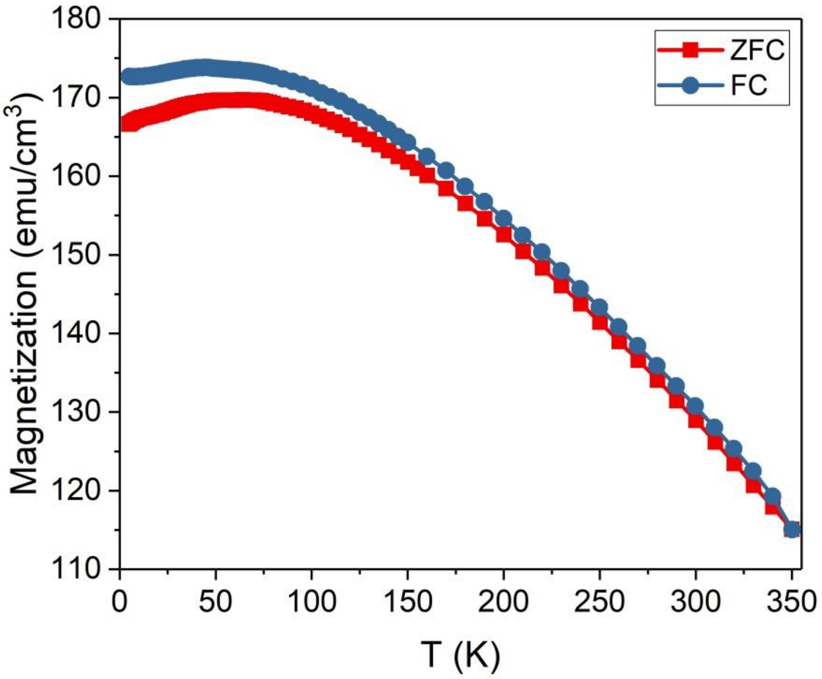

Figure 3.8: ZFC and FC magnetisation for YIG/YAG thin film taken with applied magnetic field of 100 Oe.

## 3.8 The magneto optics measurements:

### *3.8.1 Introduction:*

Magneto optics phenomena occur when an electromagnetic wave of light interacts with a magnetic media. The light propagates through the material at a different speed with left and right rotating polarization.

When the light passes through an absorbing material, the material will have a complex refractive index ($\tilde{n}$), which is divided into real and imaginary part [21]:

$$\tilde{n} = n_o + ik \tag{3.5}$$

where $n_o$ is real refractive index and $k$ is the extinction coefficient, which has a relation with the absorption coefficient[21]:

$$\propto = \frac{2k\omega}{c} = \frac{4\pi k}{\lambda} \tag{3.6}$$

where $\omega$ is the angular frequency, $c$ is the speed of light in space and $\lambda$ is the wavelength of the light. In this case, the refractive index will be written as [21]:

$$q = \frac{\omega\tilde{n}}{c} = \frac{2\pi}{\lambda} \tag{3.7}$$

where $q$ is the wave vector. The linear polarization of the light includes two opposite circular polarised components: right circular polarised (RCP) and left circular polarised (LCP). Both RCP and LCP have the same magnitude but with opposite vector rotation [22]. The refractive index can be obtained through [22]:

$$\tilde{n}_{\pm} = n_{o\pm} + ik_{\pm} \tag{3.8}$$

When the linear polarized light passes through a magnetic media, RCP and LCP will have different magnitude and refractive index ($\tilde{n}_{+} \neq \tilde{n}_{-}$). This gives a Faraday rotation ($\theta_F$), which is the difference in phase between the initial and final polarization. The Faraday rotation depends on the real part of the refractive index where ($n_{+} \neq n_{-}$)[21].

$$\theta_F = \frac{\omega t}{2c}(\Delta n) = \frac{\omega t}{2c}(n_{+} - n_{-}) \tag{3.9}$$

where *t* is the thickness of the magnetic media [21]. If the linear polarized light passes through a magnetic material, the light becomes elliptically polarized. This happens because of the difference between the imaginary parts of the refractive index for the RCP and LCP. This phenomenon called ‘magnetic circular dichroism’ (MCD) [22]:

$$MCD = \frac{\omega t}{2c}\Delta k = \frac{\omega t}{2c}(k_{+} - k_{-}) \tag{3.10}$$

MCD is a very effective technique to determine the nature of magnetic states and the spectrum with high energy-resolution [22].

### *3.8.2 Magneto optics setup:*

The setup of the magneto-optics measurement is based upon the method of Sato [23]. This method allows for a continuous and simultaneous measurement of MCD and Faraday rotation ($\theta_F$) of the sample. An illustration of the setup is shown in fig. 3.9. The setup may be between Kerr effect, which is used in reflection, and Faraday rotation, which is used in transmission. This can be performed by moving the photoelastic modulator (PEM), photomultiplier (PMT) and the analyser. The setup can work in wide range of wavelengths.

Figure 3.9: A schematic sketch of magneto optics setup according to Sato method [23]. Courtesy of Japanese Journal of Applied Physics.

In our setup, a Xenon lamp of 150 W was used. The energy of light is between 1.5 and 4.5 eV and wavelength of 827-276 nm. The lamp was placed at right angle to the rest of setup. The light passes through a spectro-275 spectrometer (monochrometer) to give a monochromatic light. Then, it passes through a selected three gratings. The light was then filtered by band passed filter dependent on the energy range, which is required. Those filters are used to remove the unwanted wavelength. Afterwards, the light passes through a Glan-Tayler UV prism polariser to allow the required plane polarised to go through the sample. The prism is placed 90° to the optical axis and 45° to analyser.

The sample was placed between the two poles of an electromagnet, which provides a magnetic field in a direction parallel to the light. If the measurements are required at room temperature, the sample will be mounted on sample holder, which has a hole allowed the light to pass through the sample and the magnetic field is about 18000 Oe. However, if the measurements are required at low temperature, the sample will be mounted on cold finger cryostat, which has an optical window. Before the run, the cryostat is evacuated to lower than $10^{-2}$ Torr then cooled down by helium gas to any temperature required that is between 10 and 300 K. The temperature was controlled automatically by an Oxford $\mathrm{ITC}^{03}$ temperature controller. The magnetic field, in this case, was about 5000 Oe because the separation between the two poles, which had been increased to fit the cryostat between them.

In addition, the light was reflected from a series of mirrors direct the light onto the sample. This alignment of mirrors helps maximising the amount of light passing through the aperture of the sample's holder.

A Hinds PEM instrument (50 KHz) was used to produce the signal proportional to the rotation and the ellipticity. This device is based on the photoelastic effect. The PEM is content birefringent crystal mounted on piezo-vibrator. When the piezo-vibrator is vibrated, the birefringence of the crystal will be changed and the polarization of the light will be modulated with a fixed frequency, $f$ (50 Hz) [24]. Then, the intensity of light oscillates with frequency of $f$ or $2f$ to show the MCD or the rotation. If there are no magneto optical effects in the sample, the intensity will remain constant at the detector. The light is passed through the analyser and focused on a PEM (Hamamatsu H8567-03 PEM module (6.7-1.4 eV)). This detector is used to transform the intensity of the light to an electrical signal. Then, it feeds it to a Hinds signal conditioning unit to split the signal into three parts: the first part is the DC component ($I_1(0)$), which was used as reference signal. DC is measured using Keithley voltmeter. The other parts were: a component with the modulation frequency, $I_2$ ($f$) and a component with twice the modulation frequency $I_3$ ($2f$), which are measured by lock-in amplifier. These three intensities $I_1(0)$, $I_2(f)$ and $I_3$ $(2f)$ have been calculated by Sato through [23]:

$$I_1(0) = I_oT\{1 + J_o(\delta_o)\sin(\Delta\theta + 2\emptyset)\} \tag{3.11}$$

$$I_2(f) = I_o\Delta TJ_1(\delta_o) \tag{3.12}$$

$$I_3(2f) = 2I_oTJ_2(\delta_o)\sin(\Delta\theta + 2\emptyset) \tag{3.13}$$

$$\Delta T = (t_+^2 - t_-^2) \tag{3.14}$$

$$T = \frac{1}{2}(t_+^2 + t_-^2) \tag{3.15}$$

where $I_o$ is the intensity constant, $J_o$, $J_1$ and $J_2$ are the Bessel function that are proportional to the light intensity, which are used to determine the maximum sensitivity of the magneto optics measurements. $\delta_o$ is the amplitude of the retaration applied by the PEM, which was set to 0.383 when $J_o$=0 and $J_1$ and $J_2$ were close to the maximum value. $\Delta\theta$ is the difference in LCP and RCP of the analyser. $t_+$ and $t_-$ are the Fresnel coefficients of RCP and LCP transmitted light, respectively. $\emptyset$ is the analyser angle, which is always set to be zero ($\emptyset = 0$).

Sato reported that [23] the Faraday rotation $\theta_F$ and Faraday ellipticity $\eta_F$ (MCD) can be calculated from the following equations:

$$\theta_F = -\frac{1}{2}\,\Delta\theta \tag{3.16}$$

$$\eta_F = \frac{1}{4}\,(\frac{\Delta T}{T}) \tag{3.17}$$

The value of $\Delta\theta$ and $\Delta T/T$ can be found from the experimental value of $I_1(o)$, $I_2(f)$ and $I_3(2f)$ through:

$$\frac{I_2(f)}{I_1(0)} = A\,\frac{J_1(\delta_o)\Delta T/T}{1+J_o(\delta_o)\sin(\Delta\theta+2\phi)} \tag{3.18}$$

$$\frac{I_3(2f)}{I_1(0)} = B\,\frac{2J_2(\delta_o)\sin(\Delta\theta+2\phi)}{1+J_o(\delta_o)\sin(\Delta\theta+2\phi)} \tag{3.19}$$

where, $A$ and $B$ are the calibration factors.

If $J_o$=0, $\phi$=0 and $\Delta\theta \ll 1$, the above equations become:

$$\frac{I_2(f)}{I_1(0)} = AJ_1(\delta_o)\frac{\Delta T}{T} \approx \eta_F \tag{3.20}$$

$$\frac{I_3(2f)}{I_1(0)} = 2BJ_2(\delta_o)\Delta\theta \approx \theta_F \tag{3.21}$$

## 3.9 Substrates:

The substrate is an important factor for growing good quality thin films because lattice match is important. Due to the complex structure of YIG, It is important to choose the substrate that has a structure and a lattice constant close to the one of YIG.

In this work, three types of the substrates were used:

### ***3.9.1 Sapphire substrate:***

Sapphire or (aluminium oxide) has a chemical formula of $Al_2O_3$. It has a corundum structure with lattice constant of $a$=4.785 Å and density of 3.98 g/cm$^3$. It is widely used with semiconductors and oxides thin films because it has a high resistivity and transparency up to 6 eV.

In this work, the sapphire substrate (0001) with two polished sides was used as a learning exercise because of its low cost. The disadvantage of the sapphire is the big mismatch with the structure of YIG. For that reason, it was impossible to obtain good quality of YIG thin films with it. Sapphire is a diamagnetic material. That means its susceptibility is temperature independent. It is used widely to study the magnetic behaviour of the films as a function of temperature [25].

### *3.9.2 YAG substrate:*

Yttrium aluminium garnet (YAG) has the chemical formula of $Y_3Al_5O_{12}$. It has a cubic structure with a lattice constant *a*=12.013 Å, which is different from the lattice constant of YIG (*a*=12.376 Å) hence there is mismatch between YIG and YAG due to the lattice mismatch ($\varepsilon$), which can be calculated from:

$$\varepsilon = \left|\frac{a_{YIG}-a_{sub}}{a_{sub}}\right| \times 100\% \tag{2.22}$$

. It has a density of 4.56 g/cm$^3$ and a good transparency to more than 4.5 eV. For this reason, it is widely used with optical applications. YAG is weak diamagnetic material; therefore, it can be used to study the YIG thin film magnetic behaviour at low temperatures [26]. In this work, YAG (100) two sides polished substrate was used.

### *3.9.3 GGG substrate:*

Gadolinium gallium garnet (GGG) has the chemical formula $Gd_3Ga_5O_{12}$. It is widely used with YIG thin films especially in microwave applications. It has a cubic structure close to the structure of YIG with lattice constant *a*= 12.383 A° compared to *a*=12.376 Å for YIG. It is best substrate used in YIG thin film applications due to the small mismatch between YIG and GGG. The density of GGG is 7.08 g/cm$^3$. GGG (100) two side polished substrates were used in this work to prepare good quality YIG thin films and Ca doped YIG [27].

GGG is a strong paramagnetic material, which causes a problem for magnetic measurements of the films due to the very large magnetic signal from the substrate. The large signal from GGG needs to be subtracted from YIG magnetic results, which is possible at high temperatures but it is difficult at low temperature measurements. The susceptibility of GGG follows Curie's law ($x = \frac{C}{T+\theta}$). GGG transforms to an antiferromagnetic state below the Curie-Weiss constant (θ=2.3K) [28]. The paramagnetic behaviour of pure GGG substrate was measured using the SQUID and the results are shown in fig. 3.10, 3.11a and 3.11b.

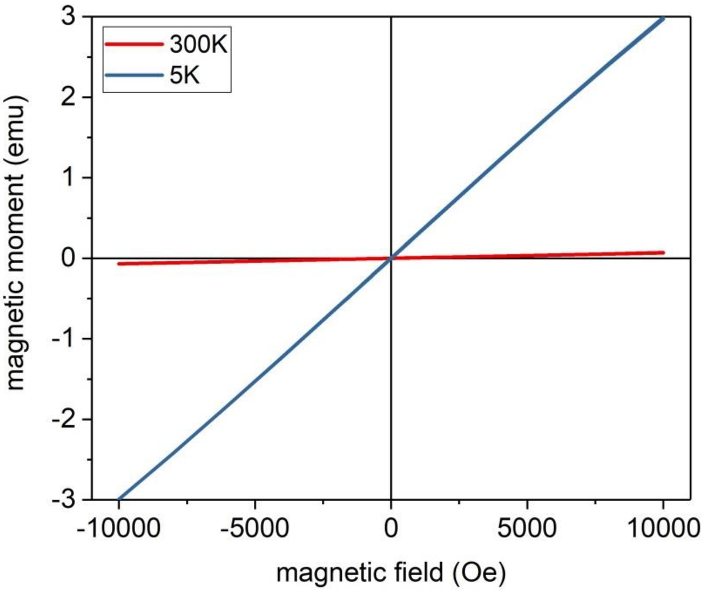

Figure 3.10: The magnetic moment for GGG blank substrate at 300 K and 5K as a function of applied magnetic field up to $10^4$ Oe. It is shows the strong paramagnetic behaviour of GGG at low temperature.

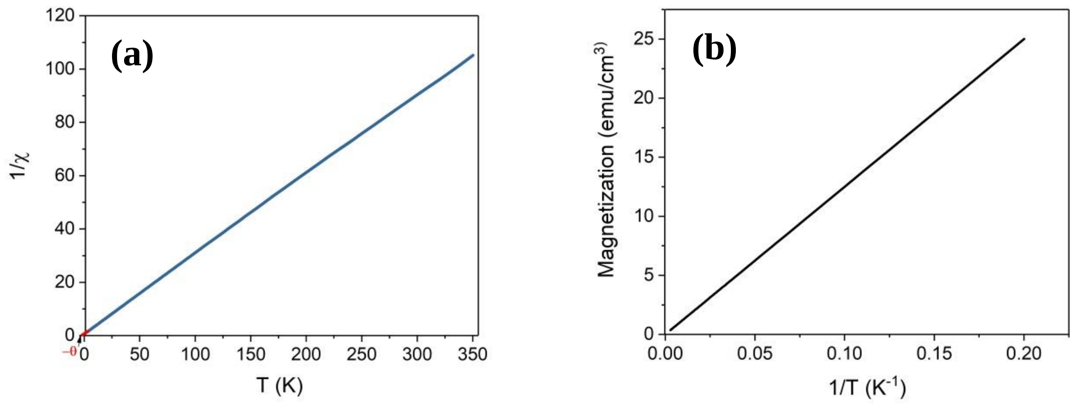

Figure 3.11: (a) the effect of temperature decreasing on the susceptibility (b) Curie law for GGG substrate.

The GGG substrate is transparent between 0.2-4eV, which is enough for our optical purposes. Due to the transparency of all substrates used, the magneto-optics behaviour at room temperature was the same for all substrates at room temperature (RT). Fig. 3.12 shows the MCD and Faraday rotation for GGG blank substrate at RT with applied magnetic field about 18,000 Oe. The scattered signal of the MCD below 1.7 eV is to reduce the sensitivity of the fall-off in the intensity of the Xenon lamp.

The MCD was measured at room temperature of the GGG substrate in the cryostat at RT and 10K with applied magnetic field about 5000 Oe, as described earlier in §3.8.2. This reduction in the applied magnetic field due to use the cryostat, which is required for the separation between the pole pieces to be increase. Fig. 3.13 shows that MCD increased with decreasing the temperature. At low temperature, the spectrum of GGG substrate shows 4*f* transition in the near UV region above energy of 3.5 eV [29]. This transition occurs between $^8$S ground state of the Gd$^{3+}$ ion and $^6$P, which is the first excited state [29]. However, for the sapphire and YAG substrates, there were no changes in the MCD with temperature according to their diamagnetic behaviour.

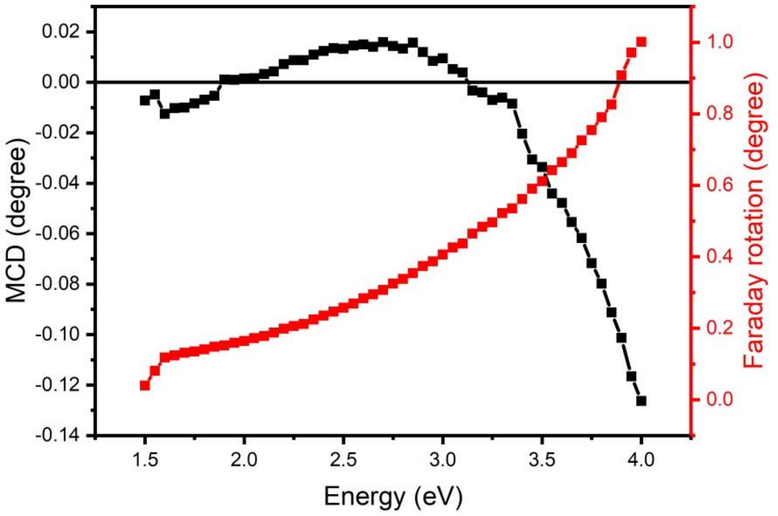

Figure 3.12: the MCD and Faraday rotation of a blank GGG substrate as a function of energy at RT with applying magnetic field of 18000 Oe.

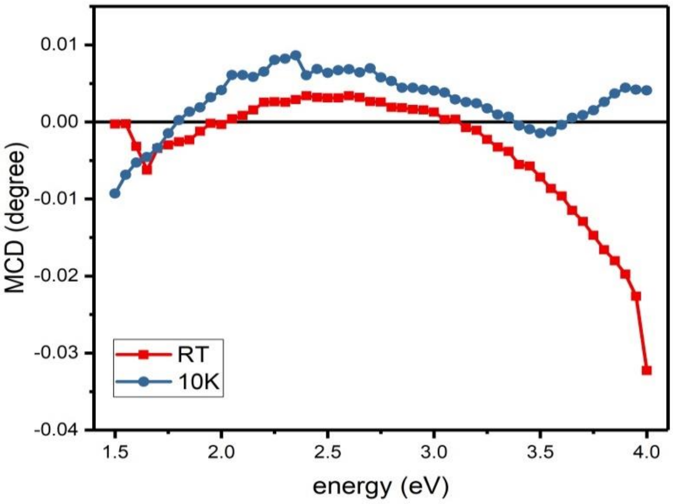

Figure 3.13: the MCD of GGG substrate at RT and 10 K as a function of energy with applying magnetic field of 5000 Oe.

## 3.10 References:

1- Karim, R., Oliver, S. A., and C. Vittoria. *IEEE Transactions on Magnetics* **31.6** (1995): 3485-3487.

2- Yang, Q., Huai-Wu Zhang, Q. W., and Ying-Li Liu. *Journal of Applied Physics* **108-7** (2010): 073901.

3- Mansour, M., et al. *Journal of Physics: Conference Series* **592** (2015): 012138.

4- Onbasli, M. C. et al *APL Mater.* **2** (2014): 106102.

5- Bao, Q., *et al*. *Applied Surface Science* **252.5** (2005): 1538-1544.

6- Dorsey, P. C. et al. *Journal of applied physics* **74** (1993): 1242-1246.

7- Delmdahl, R., and R. Pätzel. *Journal of Physics D: Applied Physics* **47.3** (2014): 034004.

8- Stvelto, O. and D.C Hanna, *Principle of lasers*. 3rd ed. (1986): 457-460.

9- Chi, T., *et al*. Veeco Instruments Inc (2004).

10- Ziese, M., Sena, S. P., and H. J. Blythe. *Journal of magnetism and magnetic materials* **202.2** (1999): 292-300.

11- Hammonds, C., "*The basics of crystallography and diffraction fourth edition*". (2015). Oxford University press, P 198.

12- Yoshio Waseda *et al*., *X-ray diffraction crystallography* (2011): 21.

13- Gaur, A., Shrivastava, B. D., and H. L. Nigam. *Proceedings of the Indian National Science Academy* **79** (2013): 921-966.

14- Newville, M. **78.1** (2014): 33-74.

15- Clarke, J. and A. I. Braginski. *"The SQUID handbook, vol. 1"*. I Fun (2004).

16- Jaklevic, R. C., *et al*. *Physical Review Letters* **12.7** (1964): 159.

17- Fagaly, R. L. *Review of scientific instruments* **77.10** (2006): 101101.

18- Janawadkar, M. P., *et al*. **77** (1999): 759-769.

19- Everitt, M. J., *et al*. *Physical Review* B **63.14** (2001): 144530.

20- McElfresh, M. *Quantum Design* **11578** (1994): 132.

21- A. Behan, "*Characterisation of Doped ZnO Thin Films for Spintronic Applications*". Thesis. Department of Physics and Astronomy, the University of Sheffield. (2008).

22- Wang, J. T., *et al*. *Journal of superconductivity and novel magnetism* **23.6** (2010): 1155-1160.

23- Sato, K. *Japanese Journal of Applied Physics* **20** (1981): 2403.

24- Wang, B., Hinds, E., and E. Krivoy. *Polarization Science and Remote Sensing IV* **7461** (2009): 746110.

25- Dobrovinskaya, E.R., Lytvynov, L.A. and V. Pishchik. *Applications Springer* (2009):55–176.

26- Sposito, A., *et al*. *Optical Materials Express* **3.5** (2013): 624-632.

27- Rossnagel, S. M., Ulman, A. and H. Maurice. Vol. 28. *Academic Press,* (2000).

28- Kinney, W. I., and W. P. Wolf. *Journal of Applied Physics* **50.3** (1979): 2115-2117.

29- Wettling, W., *et al*. *Physica status solidi* (b) **59.1** (1973): 63-70.

# 4. Iron Oxides thin films

## 4.1 Introduction:

Iron oxides are interesting inorganic materials due to their characteristic structural, magnetic and magneto optics properties. They are promising materials for storage media as supercapacitors since they are relatively easy to synthesize, have a low cost and are environmental friendly materials [1]. In this chapter, the previous research efforts on iron oxides are reviewed briefly. The structural, magnetic and magneto optics properties of the fabricated iron oxides are studied using X-ray diffraction (XRD), X-ray absorption fine structure (EXAFS), the superconducting quantum interference device (SQUID) and magnetic circular dichroism (MCD) technique.

## 4.2 Previous work:

Iron oxides of interest are FeO, $Fe_3O_4$, $\alpha$-$Fe_2O_3$ and $\gamma$-$Fe_2O_3$, which are known as wustite, magnetite, hematite and maghemite, respectively [2]. The difference between these oxides is the increased state of oxidation. These oxides are reviewed here with highlighting the most recent studies that are relevant to this work.

### *4.2.1 Wustite:*

The wustite ($Fe_{1-x}O$) is a non-stoichiometric material with Fe deficiency [3]. It has a closed-packed *fcc* (rock salt) crystalline structure with a lattice constant $a$=4.296 A° [4]. Wustite is an unstable phase below 560 ˚C [4]. Therefore, it was not studied extensively in previous research. In FeO sample, $Fe^{2+}$ atoms always donate an electron and turn to $Fe^{3+}$ with some vacancies. These vacancies occupy the interstitial (*A*) tetrahedral sites [5, 6]. Figure 4.1 illustrates the stoichiometric and nonstoichiometric structures of wustite.

Figure 4.1: An illustration of wustite cubic structure (a) pure FeO and (b) $Fe_{1-x}O$ where $Fe^{2+}$ donated an electron and became $Fe^{3+}$ [7]. Courtesy of Walter De Gruyter and Company.

Bulk stoichiometric FeO is an antiferromagnetic material below Neel temperature ($T_N$), which is about 198 K [6]. It has an interesting magnetic behaviour below $T_N$ where the magnetic moments of $Fe^{2+}$ arrange antiparallel to (111) planes and lie along [111]. The non-stoichiometry wustite has a formula of $Fe_{1-x}O$ where $x$=0.04 – 0.12. The FeO sample in this case has $Fe^{2+}$ with vacancies, which create $Fe^{3+}$ iron ions. Then, the ferromagnetic signal may appear due to the interaction between $Fe^{2+}$ and $Fe^{3+}$ ions in the nearest vacancy. As a result, wustite has $M_s$ ~ 49 emu/cm$^3$ [6].

The optical behaviour of the wustite nanoparticles show a red shift in the absorption spectra with decreasing particle size, which is different from other iron oxides and can be useful for optical applications [5]. Wustite is a promising semiconductor because of its unusual electronic properties. These properties result from its ability to change from p-type semiconductor to n-type semiconductor when $x$ becomes 0.2. In addition, it can be used in many applications such as green heat-absorbing glasses, enamels, pigments, cosmetics and tattoo inks. The Wustite nanoparticles are used as catalysis and gas sensor applications [4, 6].

### *4.2.2 Magnetite:*

Magnetite ($Fe_3O_4$) has a cubic inverse spinel structure (as shown in fig. 4.2) and its chemical formula is $(Fe^{3+})_A[Fe^{2+}\,Fe^{3+}]_BO_4$. $Fe^{2+}$ cations occupy the octahedral B-sites. $Fe^{3+}$ cations are distributed on two sites: the tetrahedral A-sites and the octahedral B-sites [8, 9]. The lattice constant of the magnetite is $a$=8.399 Å [10, 11].

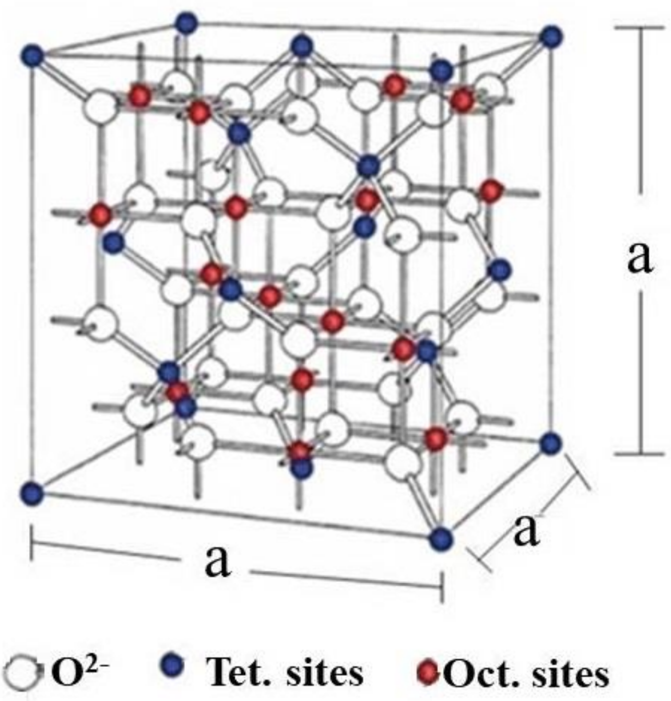

Figure 4.2: An illustration of the inverse spinel structure of magnetite [12]. Reprinted with permission of Chemical Society Reviews.

Magnetite is a chemically stable ferrimagnetic material; hence, it is used extensively in medical applications, such as: magnetic resonance imaging, magnetically guided drug delivery and also as an absorbent to remove heavy metals. It is also used in supercapacitors as an anode as well as in lithium batteries [8].

To study the magnetic properties of thin films, Parames *et al* grew magnetite films by PLD from magnetite target on Si substrates. The oxygen pressure ($P_{O2}$) was varied ~0.07 – 4 mTorr. They reported that the good quality of magnetite thin film depends on the deposition temperature. The high quality magnetite film was the film grown with temperatures higher than 600 K. In addition, the ratio of maghemite/magnetite decreased with decreasing the $P_{O2}$ [13]. On the other hand, Zhang *et al* had also grown magnetite thin films by PLD from magnetite target onto MgO substrates. The deposition temperature was 410 ˚C and different oxygen pressure was used [10]. They started with high vacuum (HV) about $7.5\times10^{-9}$ Torr and increased to $3.8\times10^{-4}$ Torr and reported that $M_s$ of the film grown in HV is close to the bulk magnetite. However, $M_s$ dropped with increasing the oxygen pressure as shown in fig. 4.3. This was as a direct result of the increased the amount of $\gamma$-$Fe_2O_3$ phase with increasing the oxygen pressure [10].

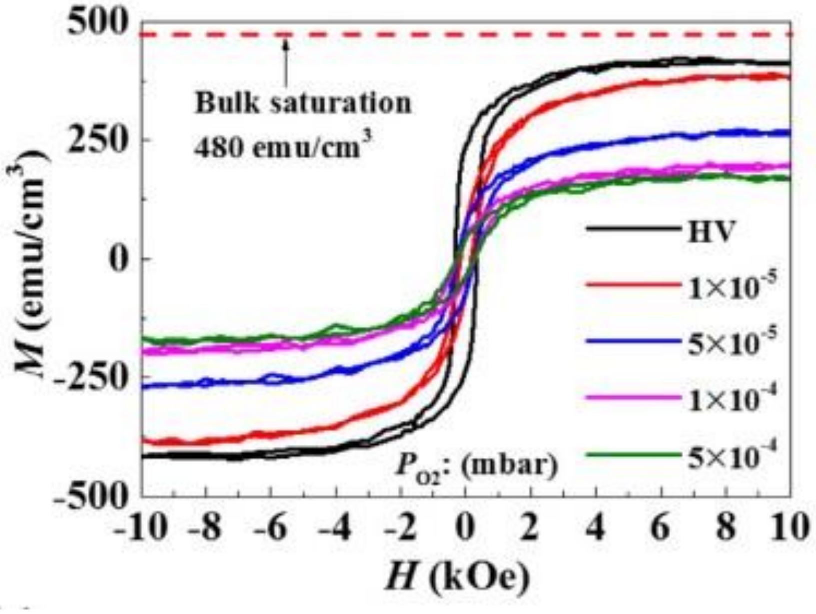

Figure 4.3: The hysteresis loops for thin films grown on MgO from magnetite target at different oxygen pressure (1mbar = 0.75 Torr). These results were measured by SQUID [9]. Reprinted with permission of Journal of Magnetism and Magnetic Materials.

The Verwey transition is one of the most important transitions in metal oxides. It occurs in magnetite below Verwey transition temperature $T_V \sim 125$ K where the symmetry of cubic spinel structure transferred to monoclinic Cc supercell structure [14, 15]. Above $T_V$, there are mobile electrons of octahedral sublattices but these become localised to $Fe^{2+}$and $Fe^{3+}$ below $T_V$ [16].

At temperatures slightly above $T_V$, the magneto crystalline anisotropy constant ($K_1$) changes its sign and its easy direction from cubic spinel [111] to cube edge [001] [17]. However, at $T=T_V$, the anisotropy constant changes its sign and the direction of its easy magnetisation from [100] to [111] [18]. This change decreases the magnetisation, coercivity, remanence and susceptibility [19]. In addition, Verwey transition affects the electrical conductivity. At $T>T_V$, the electron hopping occurs between ferrous ($Fe^{2+}$) and ferric ($Fe^{3+}$) ions with random arrangement in the octahedral sites of the cubic spinel structure hence the material is quasi metallic [18, 19]. At $T=T_V$, new electron sub-band appears and Coulomb band decreases with increasing carrier concentration. Therefore, the conductivity increases [18]. However, at $T<T_V$, the electron hopping is blocked again according to the ordering of ferrous/ferric ion in the monoclinic structure and hence the conductivity drops. In this case, the resistivity increases 100 times more than above $T_V$ and magnetite behaves as an insulator [18, 20].

The Verwey transition can be determined from ZFC/FC measurements that show the change in anisotropy. Sena *et al* prepared magnetite thin films by PLD from Fe metal target on sapphire substrates. The temperature of substrates was 575 ˚C with oxygen pressure of 3.7 mTorr [18]. They reported the Verwey transition for these films as a function of the thickness changes by using low field (50 Oe) susceptibility as shown in fig. 4.4. The strain of film increased with decreasing the thickness of the films due to the lattice mismatch, which is sufficient to exclude the transition for the films thickness less than 30 nm. However, the strain decreased with increasing the thickness up to 200 nm when the transition was found close to the Verwey transition of bulk magnetite [18].

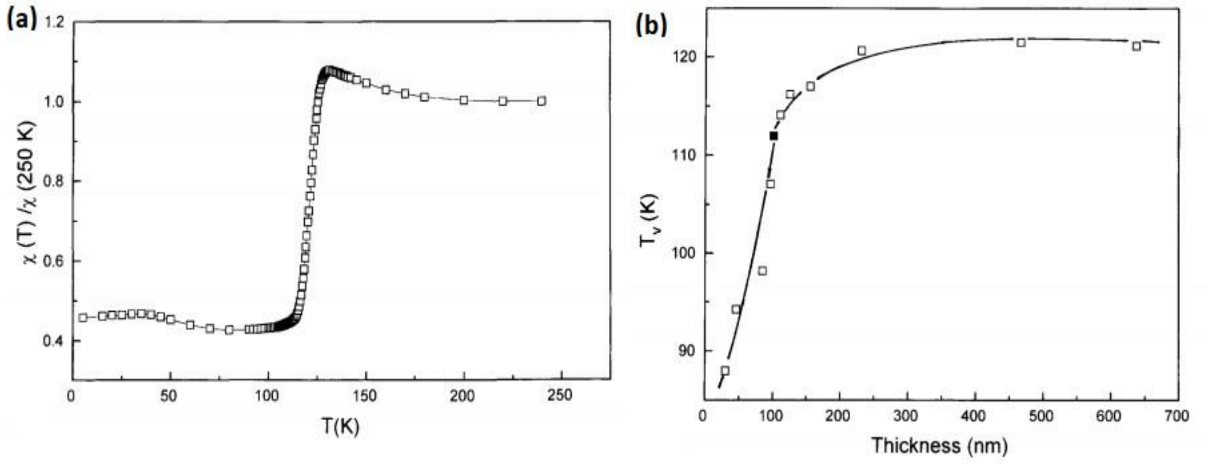

Figure 4.4: (a) Susceptibility as a function of the temperature for magnetite thin film in present of low field ~ 50 Oe. The thickness of the film was 390 nm and $T_V$ ~130 K. (b) The Verwey transition of magnetite dependence on the thickness of the films [18]. Reprinted with permission of Journal of Magnetism and Magnetic Materials.

Magnetite thin films are widely used for magneto-transparent applications due to their magnetic and magneto-optical properties [13]. The electronic structure of magnetite has a transition metal oxide structure. The valence band consisting of mostly oxygen 2p states is separated from empty the 4s states by energy gap (4-6) eV [21]. The 3d electrons interact with the oxygen ion around them to form new localized state due to the strong Coulomb repulsion between *d* electrons [21, 22]. Xuxin *et al* explained the transitions in the magnetite crystal as orbital promotion processes Fe $3d^n - 3d^{n-1}$ $4s$ model [23]. The scheme in fig. 4.5 illustrates these transitions. From fig 4.5, the right hand side indicates the band states of oxygen 2*p* and Fe 4*s*. However, the left hand side indicates the three different 3*d* localized states of iron sites. The first transition occurred in the Fe$^{2+}$ octahedral sites [$3d^6 - 3d^5$ ($^6A_{1g}$) $4s$] at energy of 0.75 eV. The second transition is also for the Fe$^{2+}$ in the octahedral sites [$3d^6 - 3d^5$ ($^2T_{1g}$) $4s$ at energy of 1.89 eV. Third transition is Fe$^{3+}$ in the tetrahedral sites [$3d^5 - 3d^4$ ($^5T_2$) $4s$ ] at energy of 2.9 eV [23].

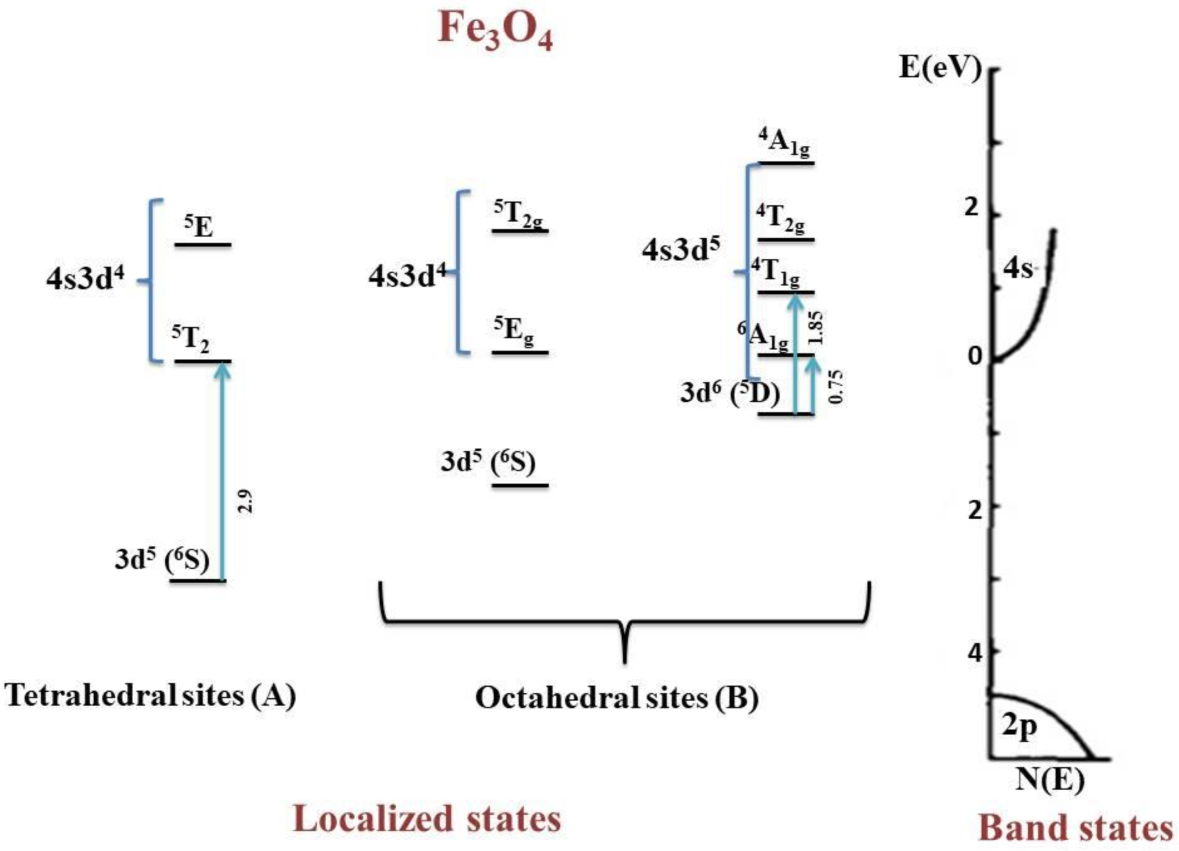

Figure 4.5: The transitions in energy level of magnetite crystal at 300 K. Adapted from ref [23]. Reprinted with permission of Solid State Communications.

Theoretically, magnetite has a 100% spin polarization near fermi level. Experimentally, Dedkov *et al* found that it has 80% polarization, which led to the use of the magnetite as a model of half metallic material [24]. Neal *et al* reported the effect of Verwey transition on the magneto-optical properties of magnetite thin films in energy range 1.5-4.5 eV [15]. The film was grown on MgO by PLD with thickness of 100 nm. $T_V$ of the film was found by SQUID measurements ~ 118 K. The MCD found from the imaginary part of dielectric tensor ($\varepsilon_{xy}''$), which was measured at different temperatures 450, 120 and 10 K as shown in fig. 4.6a. The film had two features positive at 2 eV and negative at 3 eV, which increased with decreasing the temperature. These features are due to two different transitions (fig. 4.6b). The transition at 2 eV occurs at B-sites when an electron is excited from the occupied $T_{2g}$ band to unoccupied $E_g$ band. On the other hand, the transition at 3 eV occurs due to excitation of the electron from occupied state in A-sites. However, the increase in the positive features with reducing the temperature is due to reduction the energy at the occupied state of $T_{2g.}$ In addition, there was a sharp increase in the peaks height at $T_V$ due to the increase the energy in the unoccupied states [15].

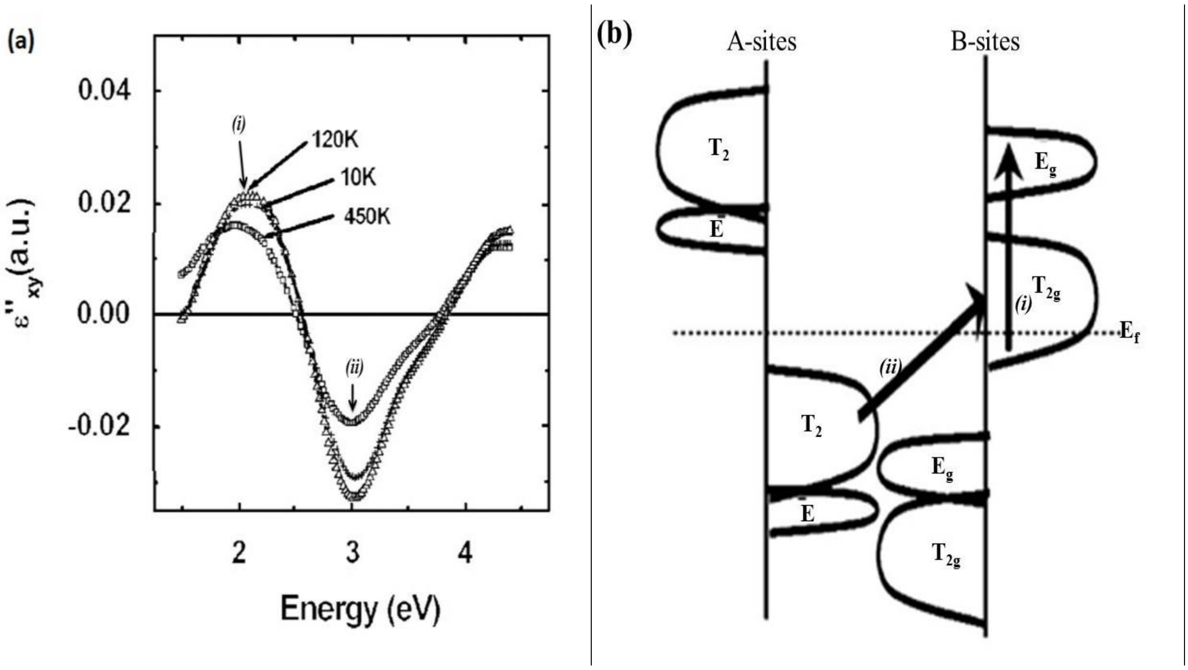

Figure 4.6: (a) The imaginary part of dielectric tensor $\varepsilon_{xy}''$ for magnetite thin film at 450, 120 and 10 K. (b) Diagram of the electronic structure of the magnetite thin film, which indicates to the transitions at energies ~ (*i*) 2 eV and (*ii*) 3 eV [15]. Reprinted with permission of Journal of Magnetism and Magnetic Materials.

### *4.2.3 Hematite:*

Hematite (α- $Fe_2O_3$) is the most thermodynamically stable type of the iron oxides. It has a low cost, is a nontoxic material and is highly available in nature [25]. This iron oxide is the traditional iron well-known as orange rust. It has a rhombohedral-hexagonal closed packed corundum structure. The oxygen ions occupy the hexagonal sites and the iron ions sites are located at the centre between the oxygen ions and surround the octahedral sites as shown in fig. 4.7 [26, 27]. This structure is close to $Al_2O_3$ structure [27].

Figure 4.7: An illustration of the rhombohedral structure of the hematite representing $Fe^{3+}$ ions (red) and $O^{2-}$ ions (green) [28]. Courtesy of National Institute for Materials Science.

Hematite can be produced from $\gamma$-$Fe_2O_3$ by phase transition from cubic structure of $\gamma$-$Fe_2O_3$ to rhombohedral structure of $\alpha$-$Fe_2O_3$. This transition depends on many factors such as: heating rate, preparation methods and grain size [27]. The temperature of this phase transition for bulk samples is between 500-600 ˚C. This temperature drops with decreasing the grain size. For nanoparticles, the range is between 200-500 ˚C; since they have a high amount of excess free energy [27].

Bulk hematite is an antiferromagnetic material but it behaves as a weak ferromagnetic material above the Morin transition ($T_M$=260 K) [29, 30]. Below $T_M$, the two magnetic sublattices of hematite are aligned antiparallel along *c*-axis with up and down spins in *c*-plane, as shown in fig. 4.8a [31, 32]. On the other hand, the magnetic sublattices canted slightly away from the antiparallel alignment and lie perpendicular to *c*-plane with weak ferromagnetism above $T_M$, as seen in fig. 4.8b [31, 32].

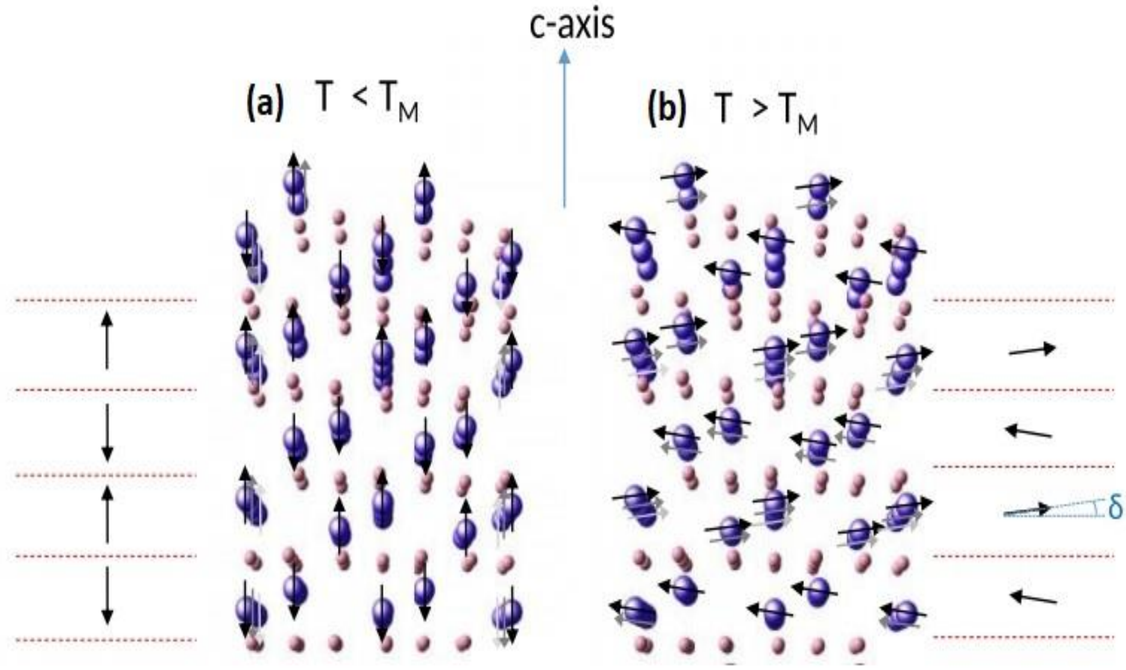

Figure 4.8: An illustration of the spin in hematite at (a) $T < T_M$ and (b) $T > T_M$. The large blue spheres are indicating the iron atoms with their spin direction and the small purple spheres are oxygen atoms. Above $T_M$, the spins canted away of the basal plane in angle ($\delta$), the arrow (↑) represents the magnetic moments [31]. Reprinted with permission of Physical Review B.

The temperature of the Morin transition depends on many factors such as: strain, applied magnetic field and grain size. This transition temperature decreases with decreasing the grain size and the Morin transition disappears at grain size below 8 nm [30, 32]. $T_M$ can be determined from ZFC and FC measurements by taking the derivation of $M$ as a function of temperature, as shown in fig. 4.9a [33]. ZFC and FC measurements were performed for micro/nanoparticles hematite with applied magnetic field of 1000 Oe in temperature range 300 – 10 K. Figure 4.9 illustrates the magnetic measurements for particle size of 1 µm, which showed an overlap for ZFC and FC curves. This overlap is expected at this particle size with $T_M$ = 245 K. $T_M$ increased with increasing the particle size. Figure 4.9.b shows the $M$-$H$ loops for the same particle size with applied magnetic field of 70 KOe and temperature of 300 and 10 K. $M_s$ of hematite at 300 K is larger than $M_s$ at 10 K. This behaviour is expected for antiferromagnetic materials below $T_M$ [33]. $M_s$ of hematite below Neel temperature (and above $T_M$) $T_N$ = 960 K is about 2.5 emu/cm$^3$ with high $H_c$ ~1000-8000 Oe [29].

The energy band gap of hematite lies in the visible wavelength range and it is about 2.2 eV with high refractive index, $n$ ~ 3. This has encouraged its use in many optical devices and as a potential candidate for solar energy conversion [25].

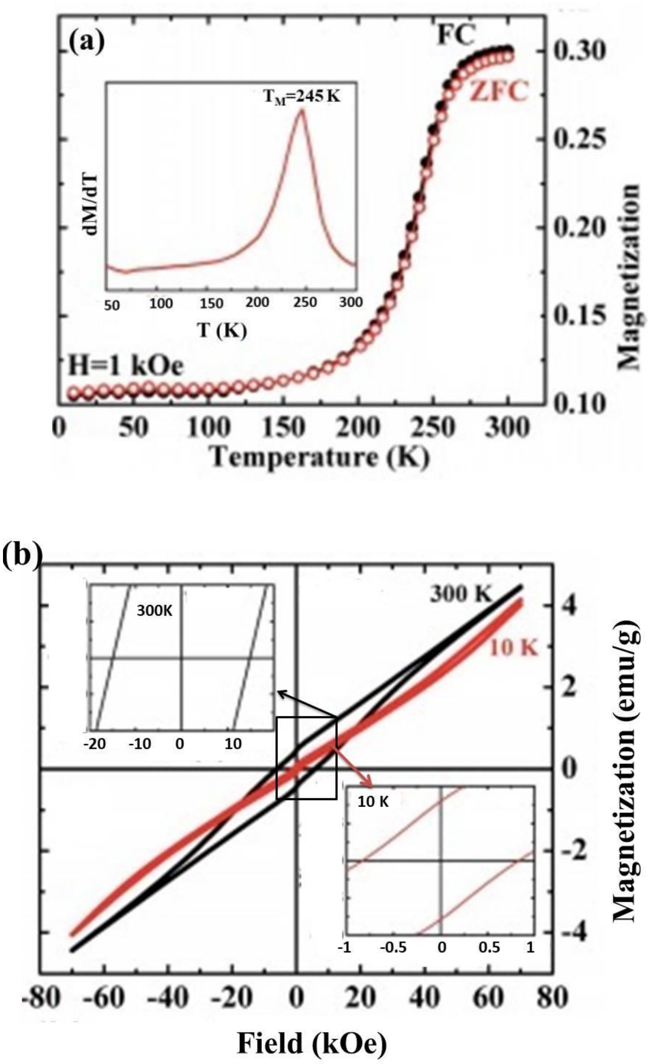

Figure 4.9: (a) ZFC and FC magnetisation and (b) *M-H* loops at 300 and 10 K. For hematite sample, which has particle size 1μm [33]. Reprinted with permission of RSC Advances.

### 4.2.4 Maghemite:

Maghemite (γ-$Fe_2O_3$) has magnetic properties that are useful for magnetic data storage media [34]. Recently, maghemite has been used in microwave devices since it is an insulator material with high resistivity ($\rho$=15 MΩcm) and energy gap (~2 eV) [34]. Maghemite thin films became promising materials for spintronic applications as a magnetic tunnelling barrier in spin filter devices. These devices require a good insulating ferrimagnetic material to control the spin current electron [35]. In addition, maghemite nanoparticles are chemically stable and non-toxic; hence, they are widely used in medical applications and drug delivery [35].

Maghemite has a metastable cubic spinel structure with lattice constant $a$= 8.51 Å [34, 36]. It transfers to the stable phase of iron oxide, hematite, above 400 ˚C [37]. Maghemite can be found in nature in soil or by weather oxidisation of the $Fe_3O_4$. This occurs by losing about 1/9 of Fe ions from the octahedral sites of $Fe_3O_4$ with keeping the crystal structure unchanged [35, 38]. All iron cations in the maghemite are in the tetrahedral sites and the change comes from present vacancies in the octahedral sites, which are distributed randomly as shown in fig. 4.10 [28, 36].

Figure 4.10: An illustration of cubic spinel structure of maghemite. The red spheres are $Fe^{3+}$, greens are oxygen and blacks are vacancies [38]. Courtesy of Zeitschrift für Naturforschung B.

Maghemite is a ferrimagnetic material with $M_s$ = 400 emu/cm$^3$ and high Curie temperature ($T_C$ ~ 950 K [35, 37]. In addition, the coercive field ($H_c$) is between 50-800 Oe [37]. However, maghemite nanoparticles are superparamagnetic materials at grain sizes less than 13 nm and their $M_s$ reduces slightly to 300 emu/cm$^3$ at room temperature [36]. Tipper *et al* fabricated iron oxide thin films by PLD from pure $\alpha$-$Fe_2O_3$ target at oxygen pressure that ranges from base pressure of $7.5\times10^{-4}$ mTorr to 53 mTorr [39]. The substrate was heated up to 500°C during the ablation and the film was annealed at same temperature. The thicknesses varied between 30 to 570 nm. They found that with increasing the oxygen pressure, the hematite phase appeared in $P_{O2}$~52 mTorr. In addition, $M_s$ reduced with increasing the thickness. The film of thickness 100 nm had $M_s$ close to the bulk maghemite ~ 390 emu/cm$^3$ as shown in fig. 4.11 [39].

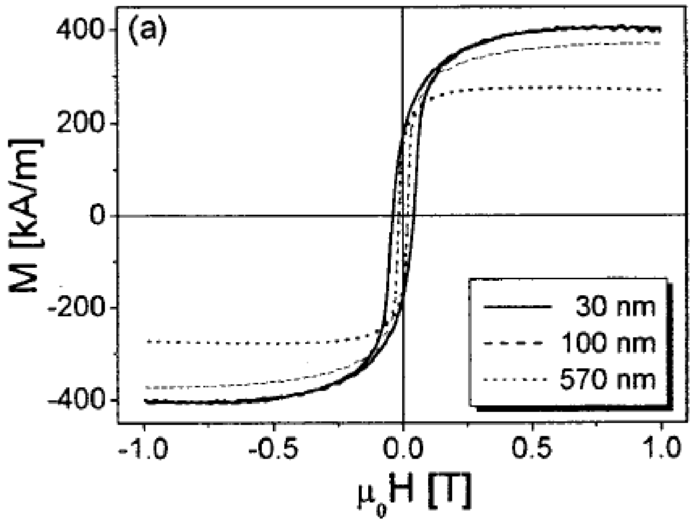

Figure 4.11: In-plane hysteresis loops of films of maghemite in different thickness. (kA/m=emu/cm$^3$) and $\mu_o H(T)$= $10^4$ Oe [39]. Reprinted with permission of Journal of Applied Physics.

The MCD measurements of iron oxides showed a phonon transition due to transiting an ion between the ground and excited state in crystal field [40]. The transition in maghemite is called '*d-d* transitions' and it occurs for the $F^{3+}$ ($d^5$-configuration). These transitions are shown in fig. 4.12, which illustrates two main positive features. First transition is at energy of *E*= 18520 cm$^{-1}$ ~ 2.3 eV, which belongs to the transition of $^6A_{1g}$ ($^6S$) – $4A_{1g}$, $^4E_g$ ($^4G$). The second feature is at *E*= 20830 cm$^{-1}$ ~ 2.6 eV, which belongs to the transition of $^6A$ ($^6S$) – $4A_{1,}$ $^4E$ ($^4G$) [40]. The MCD spectrum shows negative feature at *E*= 24390 cm$^{-1}$ ~ 3.02 eV, which represents charge transfer or transition of $^6A_1$ ($^6S$) – $^4T_2$ ($^4D$) [40].

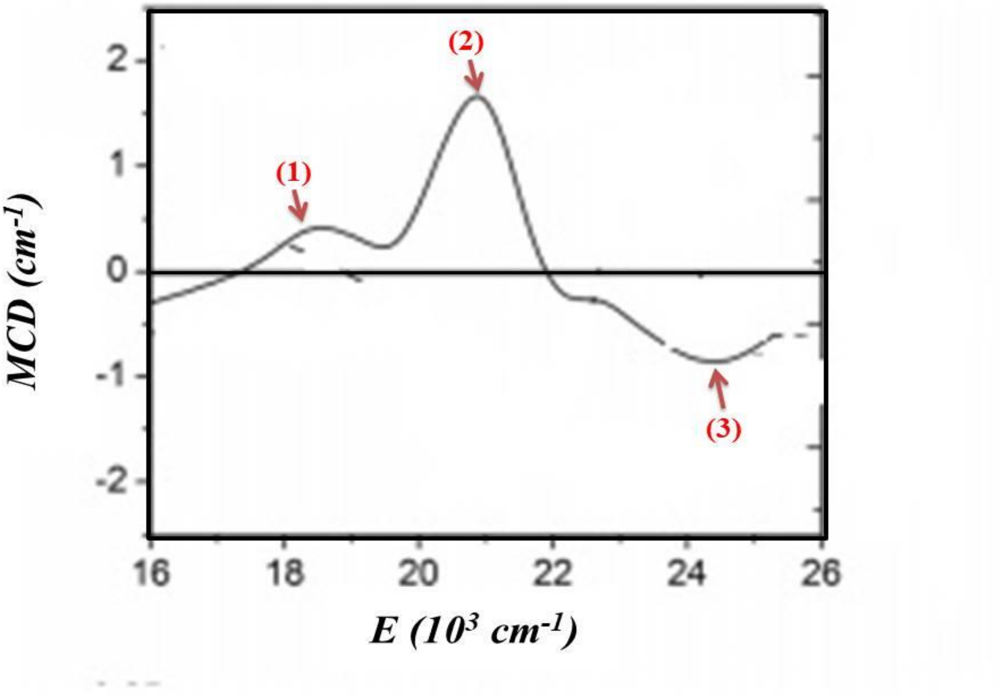

Figure 4.12: The MCD spectrum of maghemite thin film at room temperature and energy range 16000- 26000 $cm^{-1}$~ 2- 3.22 eV (1 $cm^{-1}$ = $12x10^{-5}$ eV). The figure illustrates the transitions at energy of (1) 18520 $cm^{-1}$~ 2.3 eV, (2) 20830 $cm^{-1}$ ~ 2.6 eV and (3) 24390 $cm^{-1}$ ~ 3.02 eV [40]. Reprinted with permission of Journal of Applied Physics.

In this study, iron oxides thin films are prepared by PLD technique using a target of α-Fe2O3 powder. The insights of this study can be used to fabricate thin films with lower cost and higher properties compared to previous work. In addition, this work represents an attempt to control the amount of Fe3+ iron valences using different oxygen pressures. This will help with the efforts of preparing YIG thin films by PLD (next Chapter) as YIG has Fe3+ iron ions.

## 4.3 Experimental work:

### *4.3.1 Preparation of iron oxides thin films:*

Two targets (**A** and **B**) were used to prepare thin films. Both targets were made from 10 g α-$Fe_2O_3$ with purity of 99.99%, which was purchased from Alfa Aesar. The powder was mixed twice for 15 minutes by pestle and mortar (as mentioned in Chapter 3). Then, the targets were sintered in air furnace at different temperatures:

A- **High temperature sinter:** The powder was sintered at 500 ˚C for 15 hours. Then, it was mixed again before it was pressed by vacuum pump at 16,000 KPa to prepare a disk of diameter 25 mm and thickness of 5 mm. The disk was annealed at 1200 ˚C for 19 hours in air. The colour of the target changed after annealing from red to black. The films grown by this target will be referred as samples $\mathbf{A_1}$ and $\mathbf{A_2}$.

B- **Low temperature sinter:** The powder was mixed and sintered at 500 ˚C for 15 hours. Afterwards, the powder was mixed again following the same method was used with target A. Then, the target was annealed in air at 500 ˚C for 19 hours. This target kept its red colour after annealing. The films grown by this target will be called $\mathbf{B_1}$, $\mathbf{B_2}$, $\mathbf{B_3}$ and $\mathbf{B_4}$.

The targets were used to grow iron oxides thin films on sapphire ($Al_2O_3$) substrates by PLD at 500 ˚C and different oxygen pressures (0.03 “base”, 0.1, 10 and 100) mTorr.

### *4.3.2 Crystal structure:*

The crystal structure of the films was characterised using XRD (Bruker D2 phaser device) equipment with Cu kα radiation (λ=1.54 Å) at the X-ray facility (XRF) of the University of Sheffield. EXAFS measurements were performed at the Advanced Photon Source in Argonne National Laboratory by Dr. Steve M. Heald [41]. The thickness measurements were performed using the Dektak equipment at the Kroto centre of the University of Sheffield.

Figure 4.13 shows the XRD spectra of **$A_1$** and **$A_2$** thin films, which were grown by PLD at oxygen pressure of 0.03 “base” and 100 mTorr, respectively. For the film grown at base pressure **($A_1$)**, its spectrum indicates that the majority of the film is cubic FeO. This is indicated by the matching of the peaks at 2θ= 36.22˚ and 2θ=41.97˚ with FeO (111) and FeO (200) peaks [42], respectively. The peaks at 2θ= 37.37˚ and 2θ= 57.08 suggest that this film contains an amount of magnetite since they matched the $Fe_3O_4$ (222) and $Fe_3O_4$ (511) peaks [42]. By calculating concentration $Fe_3O_4$ from XRD data, **$A_1$** thin film has $Fe_3O_4$ about 5.3%.

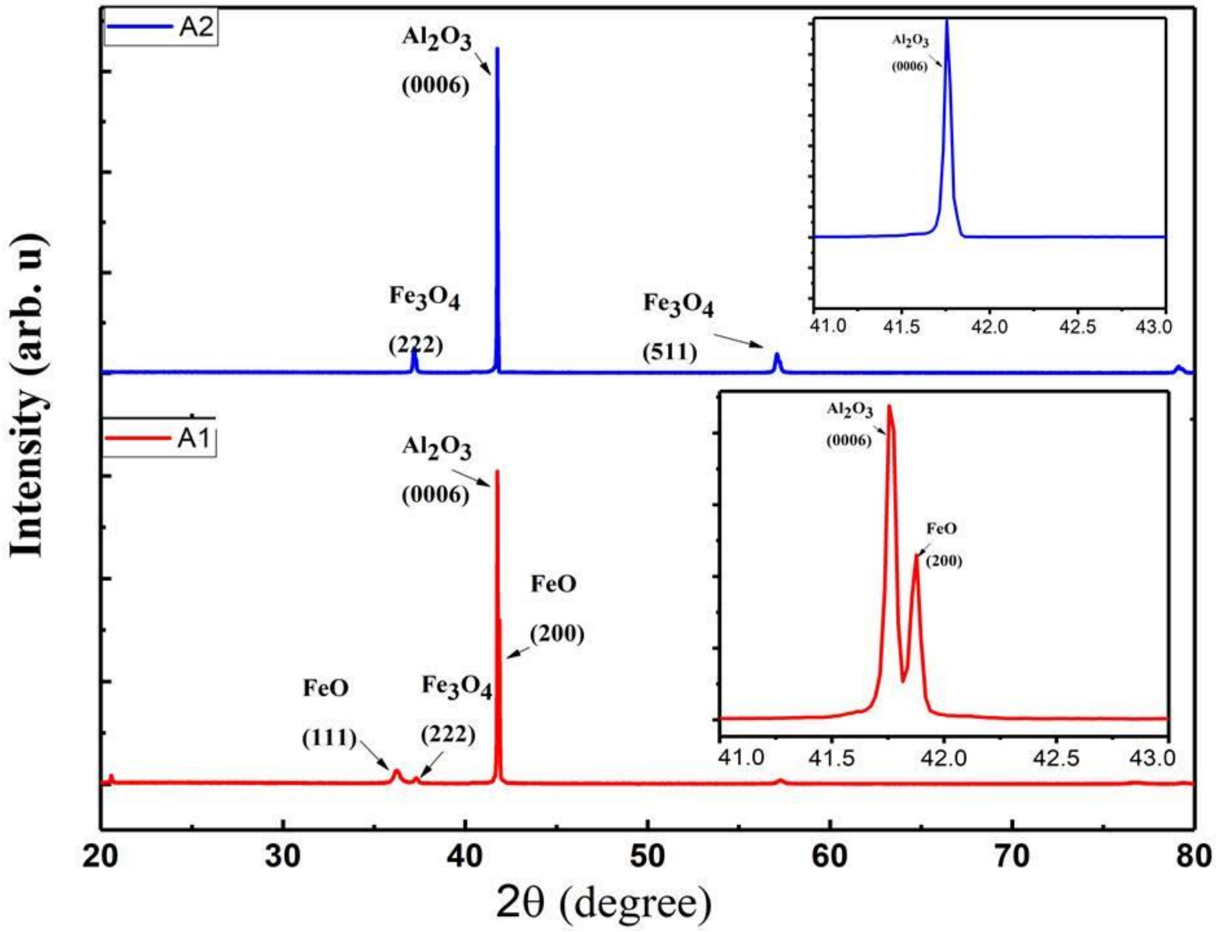

Figure 4.13: XRD spectra of **$A_1$** and **$A_2$** thin films grown on sapphire substrates with oxygen pressures 0.03 and 100 mTorr, respectively. The substrate temperature during the ablation was 500 ˚C. The insets show a magnification of the peak at 2θ=41.7°.

Another possible peak is related to magnetite (444) in **$A_2$** film, which was at 2θ=79.1˚. On the other hand, a matching of peaks with FeO was not observed in the film grown at high oxygen pressure. The sapphire substrate peak of $Al_2O_3$ (0006) was observed in both films at 2θ=41.7˚. These peaks observed in these films are similar to the ones reported previously by Pernicone *et al* [42].

The lattice constants of these films were calculated using Bragg's law (equation 3.1) and are shown in table (4.1) along with the grain size (*D*), which was calculated from Sherrer's equation (equation 3.3). The lattice constant of FeO in film **$A_1$** was calculated using the peak FeO (200) and it was found to be *a*= 4.287 Å, which is close to the lattice constant of bulk wustite *a*= 4.296Å. However, the peak of $Fe_3O_4$ (222) that was observed in both films suggests *a*= 8.390 Å, which is close to the bulk magnetite lattice constant *a*= 8.394 Å [42].

Table 4.1: The results of thickness measurement, XRD and the concentration of $Fe_3O_4$ and FeO, which were determined from XRD measurements, for **$A_1$** and **$A_2$** thin films grown by PLD at different oxygen pressures:

| **Sample No.** | **$P_{O2}$ (mTorr)** | ***t* (nm)** | ***2θ* (°)** | ***(hkl)*** | ***D* (nm)** | ***a* (Å)** | **$Fe_3O_4$ (%)** | **FeO (%)** |
|---|---|---|---|---|---|---|---|---|
| **$A_1$** | Base | 150 ±5 | 41.9 ±0.2 | (200) | 88 ±0.2 | 4.287 ±0.0003 | 5.3 | 94.7 |
| **$A_2$** | 100 | 150 ±5 | 37.2 ±0.01 | (222) | 48 ±0.3 | 8.391 ±0.0002 | 100 | 0 |

XRD spectra of the films grown from target **B** showed only the peak of the sapphire in all target **B** films. This indicates an amorphous nature in these films. Another possibility is a strong crystal texture in these films. Both possibilities needs further investigation to be confirmed. The use of XRD equipment with sample-rotation capability can help to clarify the nature of these films. Furthermore, Raman spectroscopy is another tool that can be used in order to obtain further information for the structural analysis of these films.

**$A_1$** film's XANES (fig. 4.14) was compared to the secondary iron oxide phases of FeO, $Fe_2O_3$ and $Fe_3O_4$ standard powders. The type of the iron oxide can be determined by XANES by observing the shift in the edge of the spectra. This shift represents the iron valency and a high shift means an increase in the iron valencies [43]. In addition, the height of the peak indicates a likely oxidization in the film [43]. For film **$A_1$**, it lays between FeO and $Fe_3O_4$ standard powders near edge spectra. This is a strong indication that this film is likely to contain both $Fe^{2+}$ and $Fe^{2+}Fe^{3+}$ valencies with majority of $Fe^{2+}$, which indicates FeO structure as was suggested by XRD results.

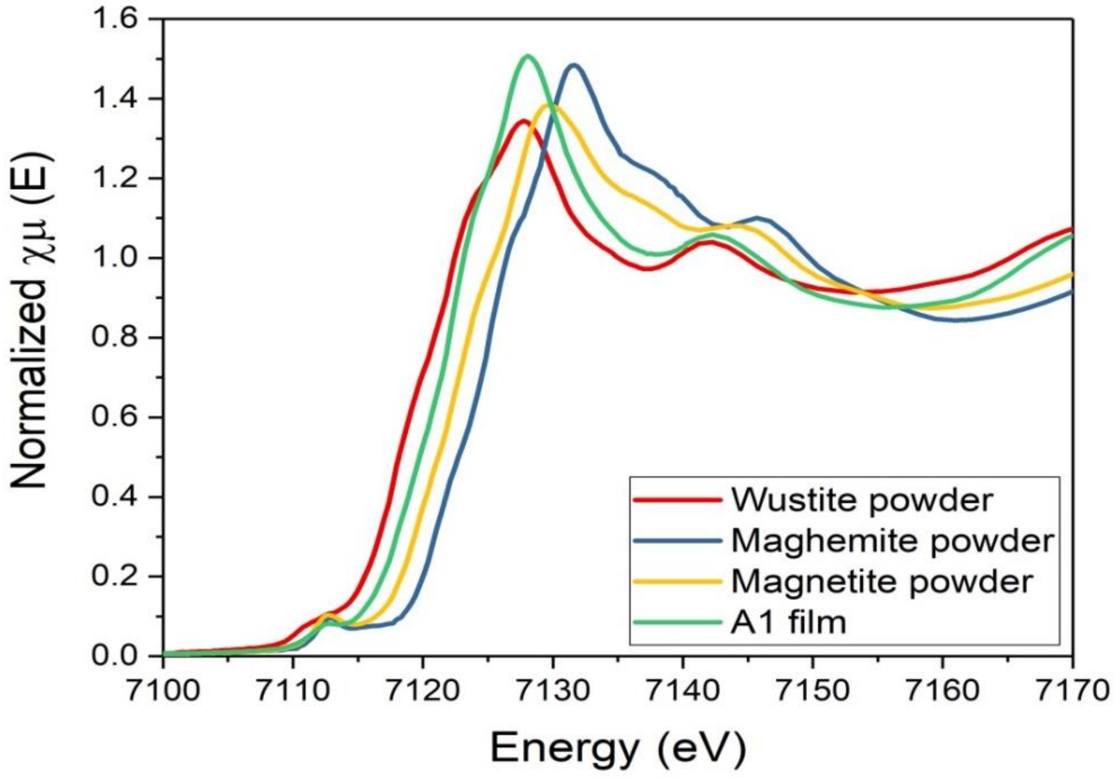

Figure 4.14: Normalised Fe Valencies near edge XANES spectra for **$A_1$** thin films, which was grown in base oxygen pressure, compared with FeO, $Fe_2O_3$ and $Fe_3O_4$ standard powders.

XANES spectra for **$A_2$** thin film (fig. 4.15) were compared to magnetite standard powder spectra. The matching of both spectra indicates that this film has a magnetite structure.

However, the intensity peak of the film was slightly higher than the standard powder, which suggests that the film was oxidized slightly more than magnetite powder [43].

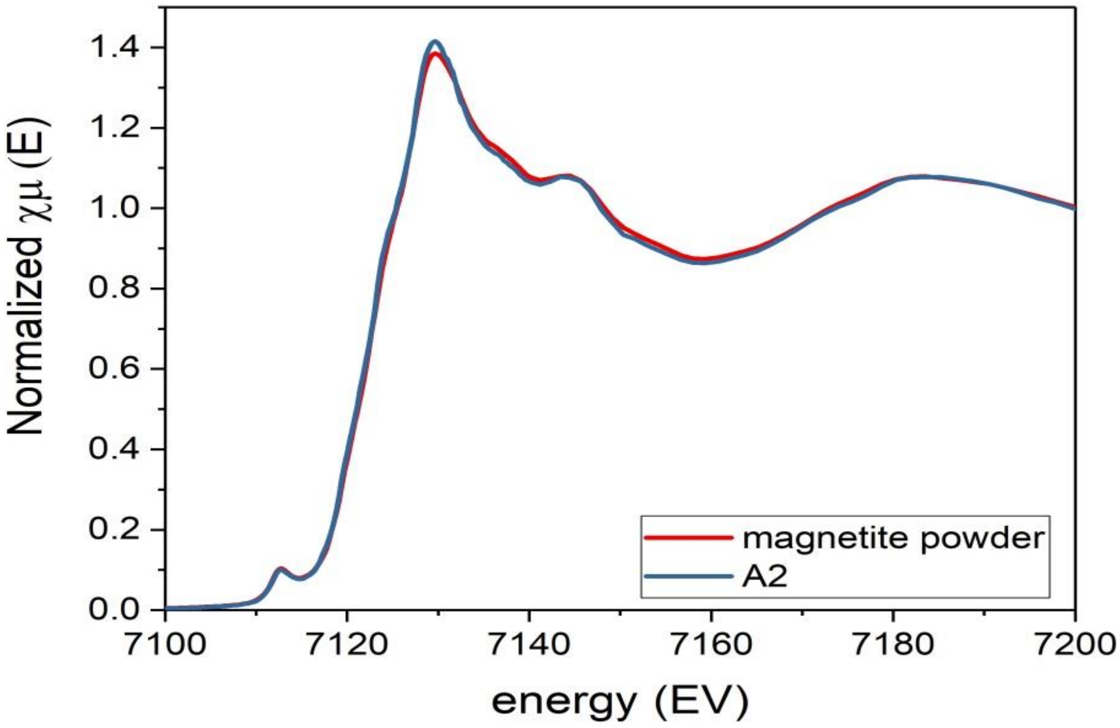

Figure 4.15: Normalised iron valencies near edge XANES spectra for **$A_2$** thin films, which is grown with 100 mTorr oxygen pressure, compared with $Fe_3O_4$ standared powder.

Table 4.2: the concentrations of $Fe_3O_4$ and $Fe_2O_3$, which are obtained from XANES measurements for the films prepared from target B by PLD technique.

| **Film No.** | **$P_{O2}$ (mTorr)** | **$Fe_3O_4$ concentration (%)** | **$Fe_2O_3$ concentration (%)** |
|---|---|---|---|
| **$B_1$** | Base | 87 | 13 |
| **$B_2$** | 0.1 | 60 | 40 |
| **$B_3$** | 10 | 42 | 67 |
| **$B_4$** | 100 | 10 | 90 |

XANES spectra for **$B_1$, $B_2$, $B_3$ and $B_4$** are shown in fig. 4.16. The near edge compared to $Fe_2O_3$ and $Fe_3O_4$ standard powders spectra. The percentage of each oxide can be determined from XANES spectra that show films contain $Fe_3O_4$ about 87, 60, 42 and 10%, respectively, as shown in table 4.2. The comparison between these spectra indicates that the amount of pure $Fe^{3+}$ increases with increasing the oxygen pressure during the ablation, which indicates that a high oxygen pressure is required in order to have pure $Fe^{3+}$ ions in the films, as shown in table 4.2.

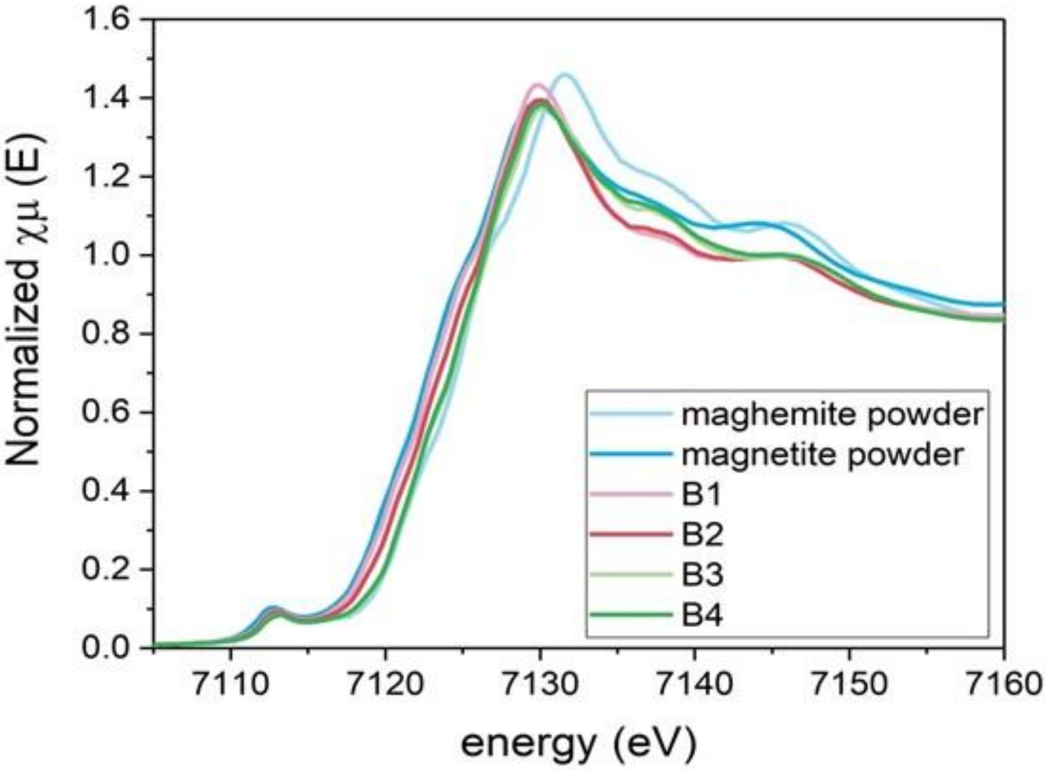

Figure 4.16: Normalised Fe valences for **$B_1$, $B_2$, $B_3$** and **$B_4$** thin films compared to $Fe_2O_3$ and $Fe_3O_4$ standard powders.

The XRD analysis of the **$A_1$** and **$A_2$** films (where the target was annealed at 1200 ˚C) revealed that the majority of the film prepared at base pressure (**$A_1$**) has an FeO structure, while increasing the oxygen pressure in the chamber resulted in a majority of $Fe_3O_4$ structure in the **$A_2$** film an XANES analysis agreed with the XRD analysis of **$A_1$** and **$A_2$** films. For **$B_{1\text{-}4}$**

films that prepared from target, which was annealed at 500 ˚C; the XANES spectra suggested that a higher oxygen pressure resulted in a higher amount of $Fe_2O_3$ phase. This was indicated ionisation energy by the higher occurrence $Fe^{3+}$ ion in these films. Further investigation to this information can be achieved by comparing the magnetic properties of these films. A summary of all the films concentrations and their results will be provided at the end of this chapter.

### *4.3.3 Magnetic properties:*

The magnetic properties of iron oxide thin films were characterised by SQUID in the presence of an applied magnetic field of $\pm 10^4$ Oe at temperatures of 300 and 5 K. For **A** films, the *M-H* hysteresis loops for $\mathbf{A_1}$ thin film were measured at 300 and 5K (fig. 4.17). The linear diamagnetic behaviour of sapphire substrate was subtracted. $M_s$ for this film was ~71 emu/cm$^3$, which is higher than $M_s$ of FeO ~ 49 emu/cm$^3$. This suggests that this film contains a small amount of $Fe_3O_4$, which agrees with XRD and EXANS results. The amount of each oxide in the films can be calculated from:

$$M_{s(Total)} = f\, M_{s(Fe3O4)} + (1-f)\, M_{s(FeO)} \sim 71 \text{ emu/cm}^3 \qquad (4.1)$$

where $M_{s(Total)}$ is the total saturation magnetisation of the film, $f$ is the fraction of $Fe_3O_4$, $M_{s(Fe3O4)}$ is the saturation magnetisation of bulk $Fe_3O_4$, which is 480 emu/cm$^3$ and $M_{S(FeO)}$ is the saturation magnetisation of bulk FeO. From equation 4.1, $\mathbf{A_1}$ film contains about 5.1 % $Fe_3O_4$ and 94% FeO. FeO has no effect at low temperature, whereas at 300 K, increased the magnetisation, which suggests that this film contains a small amount of hematite. This behaviour can be observed in hematite due to Morin transition [30].

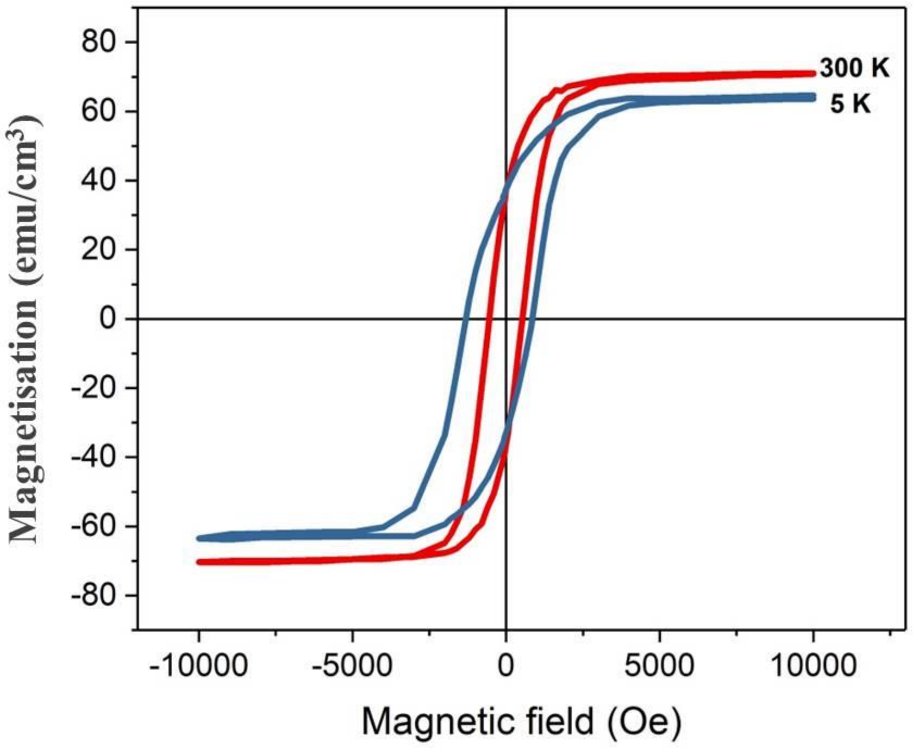

Figure 4.17: The hysteresis loops of $A_1$ thin film at temperatures of 300 and 5 K.

For $\mathbf{A_2}$ thin film, $M_s$ is 470 emu/cm$^3$ (fig. 4.18). This $M_s$ is close to $M_s$ of bulk $Fe_3O_4$, which is in agreement to XANES and XRD results. $H_c$ of this film was at the range of $Fe_3O_4$. On the other hand, the hysteresis loop of $\mathbf{A_2}$ thin film at 5K has a shift in both +ve and -ve directions, as shown in fig. 4.18. These shifts indicated that an interesting behaviour occurred. This shift of the hysteresis loop could have occurred due to existence of a ferrimagnetic (ferromagnetic) and antiferromagnetic phases in the film; similar to $\mathbf{A_1}$ films. This shift was observed in $\mathbf{A_2}$ film only at T=5 K due to $T_N$ of FeO ~ 198 K (fig. 4.18). The coupling of $Fe_3O_4$ and FeO above $T_N$ is likely to be weak due to the disturbance of atomic distances due to thermal vibration.

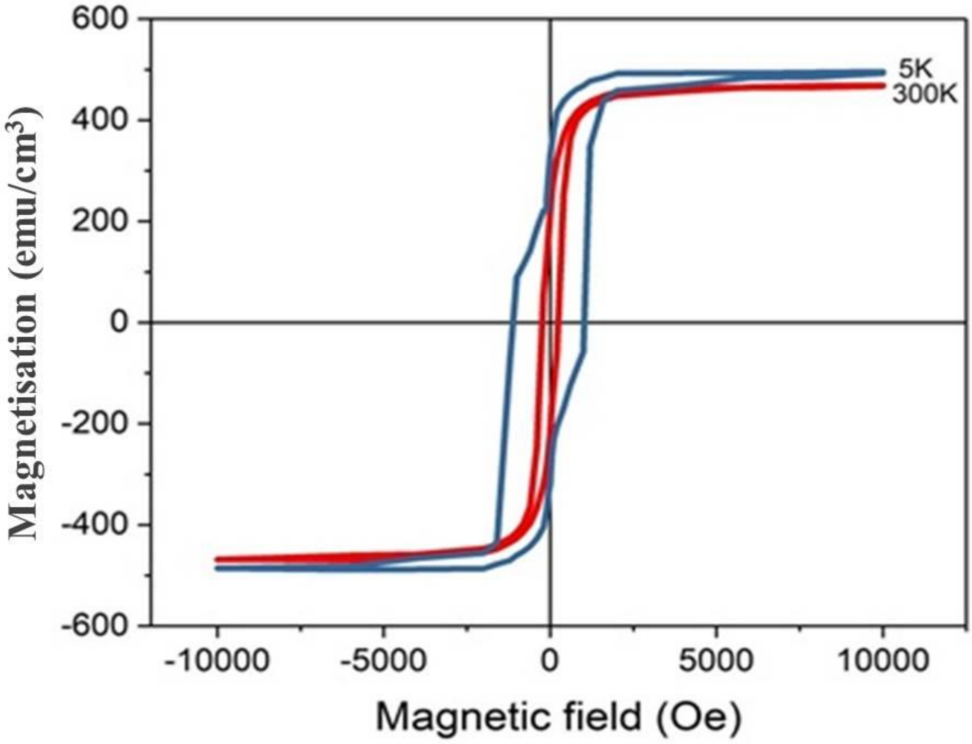

Figure 4.18: The hysteresis loops of $A_2$ thin film at (300 and 5) K.

For **B** thin films, *M-H* hysteresis loops of $\mathbf{B_1}$, $\mathbf{B_2}$ and $\mathbf{B_3}$ thin films (fig. 4.19) show that $M_s$ of these films were 78, 110 and 264 emu/cm$^3$, respectively. These $M_s$ values are less than $M_s$ of magnetite (480 emu/cm$^3$) or maghemite (400 emu/cm$^3$), which were expected based on the understanding of XANES results (fig. 4.16). This lower magnetisation is common in magnetite films when they are grown epitaxial on sapphire substrate, which is due to a structural mismatch between the film and the substrate, which results from the different crystal structure between the cubic structure of magnetite and the hexagonal structure of the sapphire [46]. This mismatch is caused by lattice defects, which lead to changes in the magnetisation and transport properties. The amount of the mismatch in these films was difficult to be specified from the XRD spectra as was mentioned earlier in §4.3.2 [46]. This behaviour is known as the "anti-phase boundary" [46]. The paramagnetic contributions in $\mathbf{B_2}$

and **$B_3$** films, which are shown in fig. 4.19, are probably resulted from the canted antiferromagnet hematite.

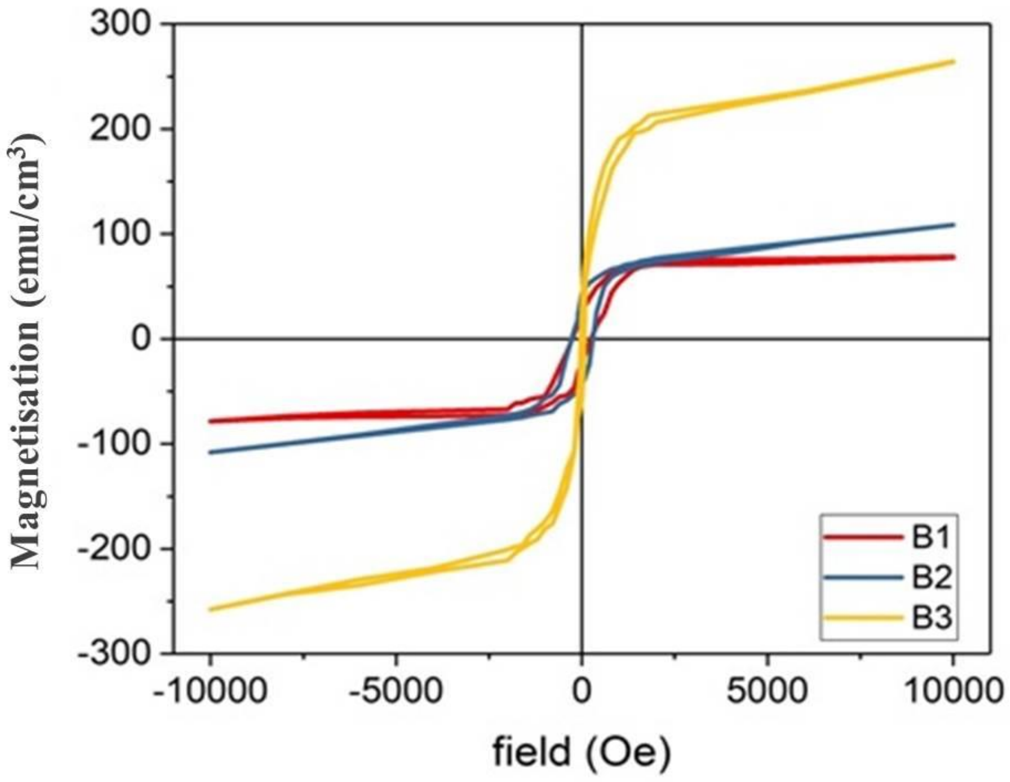

Figure 4.19: The hysteresis loops of $B_1$, $B_2$ and $B_3$ thin films at 300 K.

Fig. 4.20 shows the hysteresis loops of **$B_4$** thin film, which is grown at 100 mTorr oxygen pressure. $M_s$ of this film was 398 emu/cm$^3$, which is close to $M_s$ of maghemite. This result agrees with results obtained by XANES (fig. 4.16).

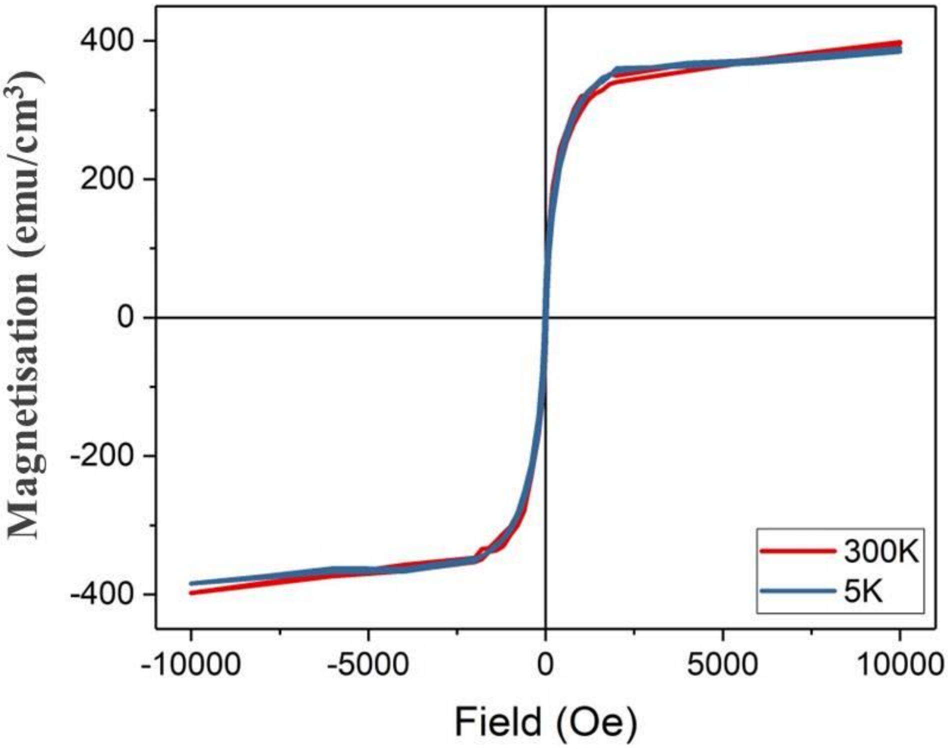

Figure 4.20: The hysteresis loops of $B_4$ thin films at 5 and 300 K.

Table (4.3) shows the magnetic properties for all iron oxides films. **$A_1$, $B_3$** and **$B_4$** films showed a reduction in magnetisation with decreasing the temperature. This suggests that these films contain an amount of canted antiferromagnetic hematite. Hematite has a Morin transition at 260 K, which affects the magnetisation as described in section 4.2.3[30].

The magnetisation as a function of temperature was measured for **$A_1$, $A_2$** and **$B_1$** films with applied magnetic field of 100 Oe and temperature range 5-350 K by using ZFC/FC method as shown in fig. 4.21, 4.22 and 4.23, respectively. The derivatives of magnetisation as a function temperature (dM/dT) of ZFC curves were taken since the slope of ZFC curve gives the maximum value at certain temperature, which indicates the Verwey transition ($T_V$) [18]. The $T_V$ for **$A_1$** and **$A_2$** thin films (fig. 4.21 and 4.22) is close to bulk magnetite $T_V$ ~ 126 K. This indicates that these films have a pure stoichiometric magnetite [47]. However, $T_V$ is lowest for the **$B_1$** film. This reduction in $T_V$ (lower than bulk magnetite) is due to non-stoichiometric magnetite, which usually results from oxidizing the magnetite into maghemite. Hence, $T_V$ is reduced when the film contains non-stoichiometric maghemite [47]. ZFC/FC curves show that the magnetisation increased with increasing the temperature until it reached $T_V$ then the magnetisation started dropping with increasing the temperature. $T_V$ marks the peak point in the magnetisation due to the overcoming of the thermal energy over the anisotropy energy. Below $T_V$, the anisotropy energy is usually higher than the thermal energy [48].

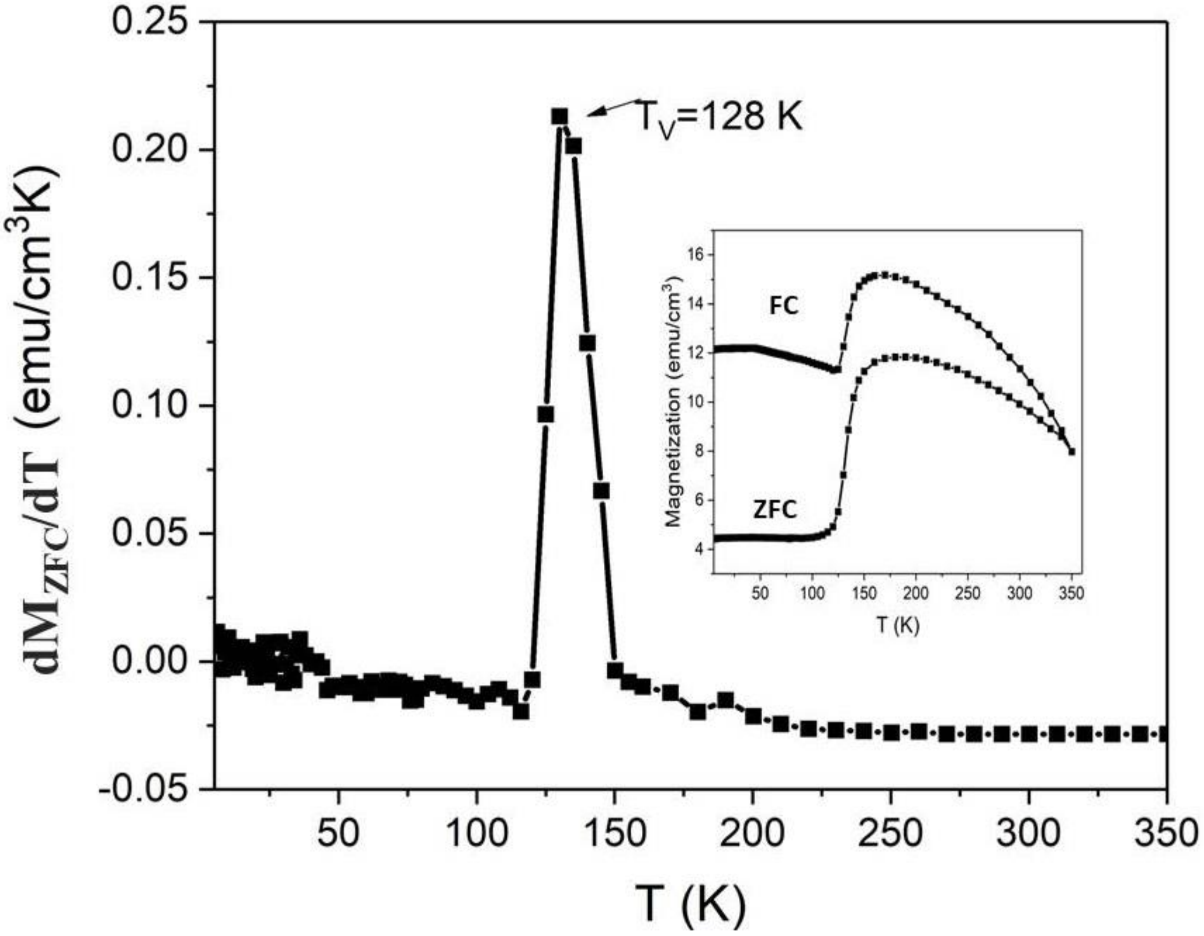

Figure 4.21: The derivative of $M$ as a function of $T$ to determine $T_V$ of $\mathbf{A_1}$ thin film and its ZFC/FC curves.

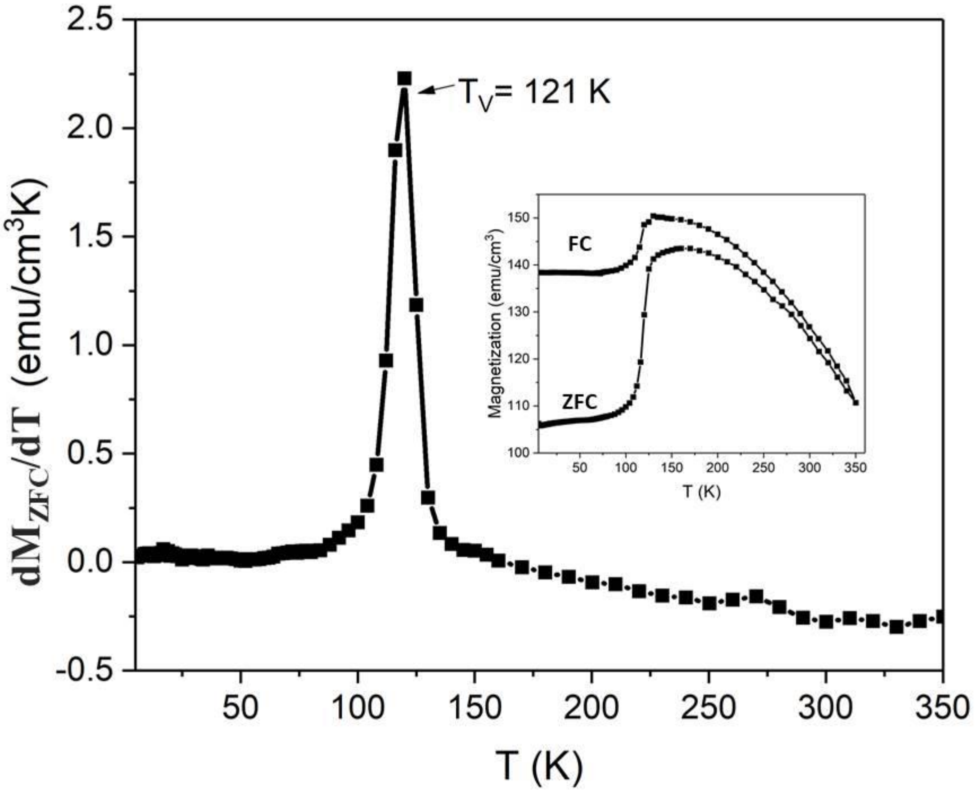

Figure 4.22: The derivative of M as a function of T to determine $T_V$ of $\mathbf{A_2}$ thin film and its ZFC/FC curves.

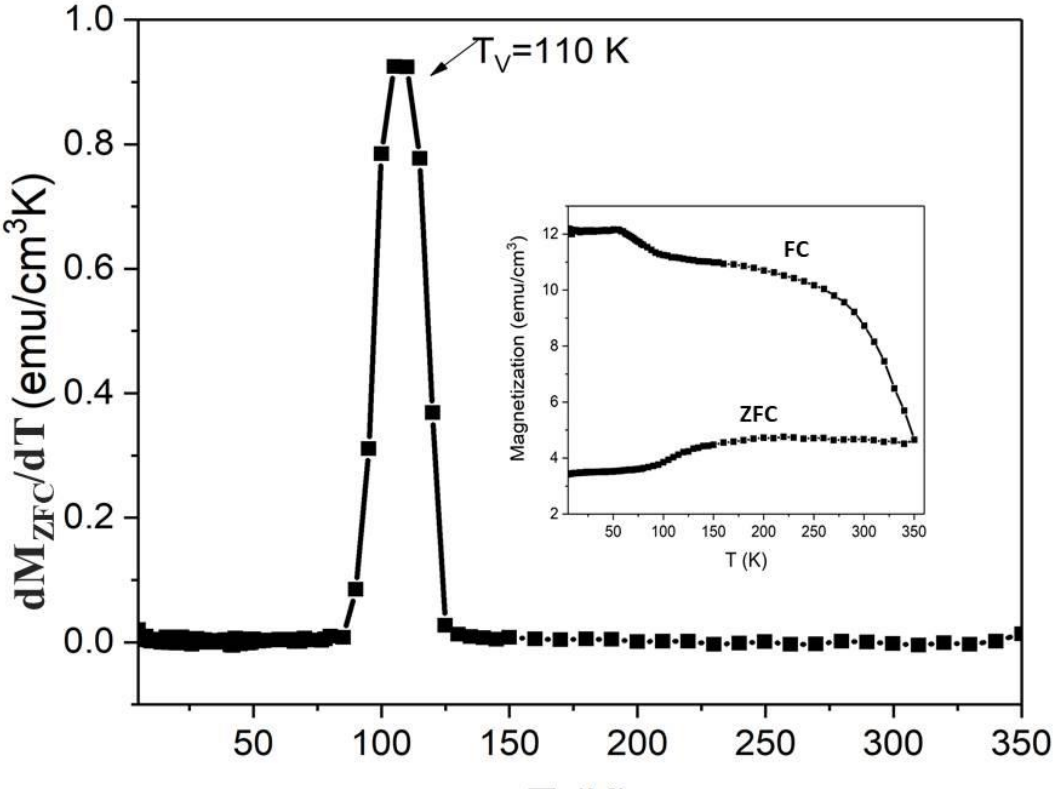

Figure 4.23: The derivative of $M$ as a function of $T$ to determine $T_V$ of $\mathbf{B_1}$ thin film and its ZFC/FC curves.

The magnetic characterisation of the **A$_{1\text{-}2}$** and **B$_{1\text{-}4}$** films confirmed the insights obtained in the crystal structure analysis. This was represented by the observed increase in $M_s$ with increasing the oxygen pressure in both types of films. On the other hand, $T_V$ was observed in **A$_1$**, **A$_2$** and **B$_1$** films, which have a high content of $Fe_3O_4$.

### *4.3.4 Magneto optics properties:*

The MCD spectra were measured using a magnetic field of ±18,000 Oe in the +ve and –ve directions. The measurements were taken at energy range of 1.5-4 eV. The MCD of **A$_1$** and **A$_2$** thin films are shown in fig. 4.24 and it indicates that there are two special paramagnetic features at 2.2 eV and 3.2 eV. Based on the structure and magnetic properties of these films, these features are likely to be related to $Fe_3O_4$ phase (fig. 4.6a). The positive paramagnetic feature at 2.2 eV is due to crystal field *d-d* transition of $Fe^{2+}$ at the octahedral site [15, 49]. However, the negative paramagnetic feature is due to crystal field *d-d* transition of $Fe^{3+}$ at the octahedral site [15, 49]. These transitions are illustrated in fig. 4.6 (§4.2.2).

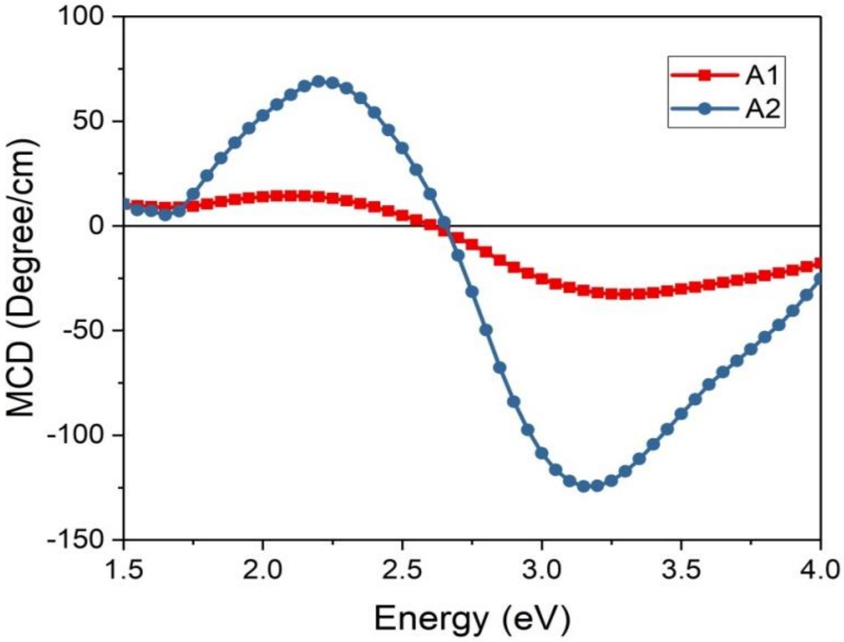

Figure 4.24: MCD spectra of **A$_1$** and **A$_2$** thin films, which were grown at oxygen pressure of base and 100 mTorr, respectively. The measurements were taken in applied magnetic field of ±18000 Oe and at room temperature.

FeO may also have *d-d* transitions below 2 eV but they are usually covered by a band, which is shown in fig. 4.25 in the region below 1.8 eV. This band is due to the defects in FeO as a result of the non-stoichiometry of FeO crystal [50]. Figure 4.25 illustrates the MCD spectra of $\mathbf{B_1}$, $\mathbf{B_2}$, $B_3$ and $\mathbf{B_4}$ thin films, which were indicated from the structural and magnetic characterisation. These films contain a different amount of $Fe_2O_3$ and $Fe_3O_4$. It is likely that $\mathbf{B_1}$ has two paramagnetic features at 2.2 eV and 3.25 eV. These features are related to two different transitions in $Fe_3O_4$ as mentioned above. The peak of 2.25 eV was shifted slightly and decreased with increasing $Fe_2O_3$ amount until it became flat in $\mathbf{B_4}$ thin film, as shown in fig 2.26 (a). Moreover, the intensity of the peak at 3.25 also decreased and shifted, as shown in fig. 2.26 (b). This behaviour was explained by Betivegna *et al* where they showed the weak MCD spectrum of $Fe_2O_3$ below 2.2 eV and shown in fig. 4.12. Then, it increased near the absorption band of $Fe_2O_3$ [40, 51]. The feature around 2.75 eV is likely to be related to $Fe_2O_3$, which has two absorption components located near 2.6 eV and 3eV. This behaviour of $Fe_2O_3$ is similar to the YIG but with more complex structure in YIG [52]. This transition was discussed in §4.2.4 and shown in fig. 4.12. The height of this peak indicates a higher amount of $Fe_3O_4$ (higher peak suggests higher $Fe_3O_4$) [51].

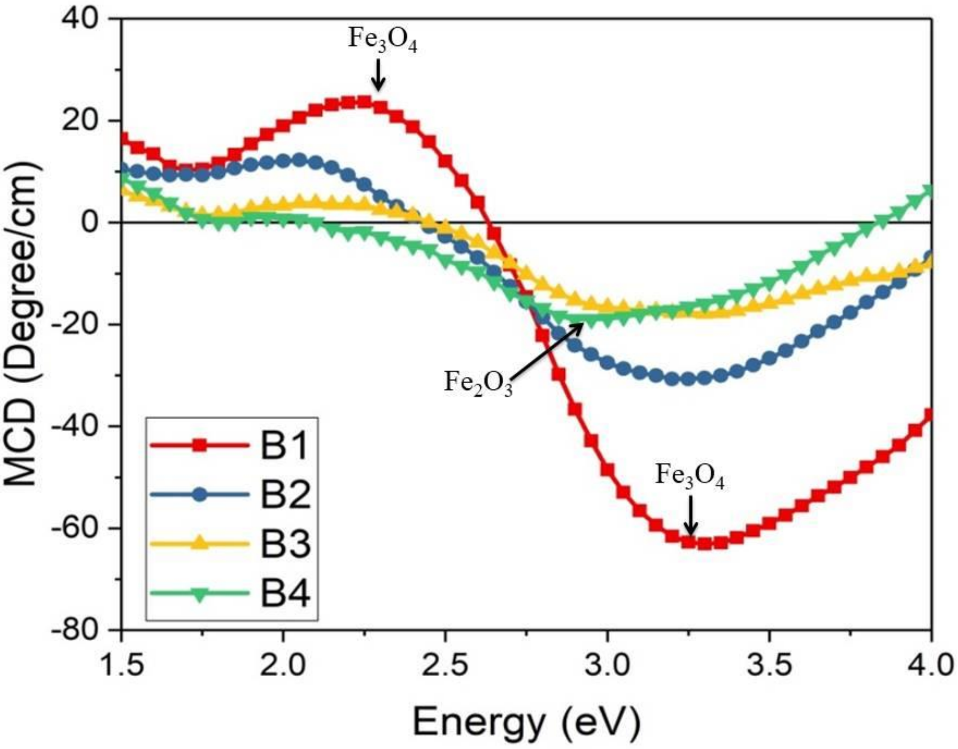

Figure 4.25: MCD data for **$B_1$**, **$B_2$**, **$B_3$** and **$B_4$** thin films. They showed the peaks of transition related to $Fe_3O_4$ or $Fe_2O_3$ phases. The measurements were taken in present of ±18,000 Oe applied magnetic field and at room temperature.

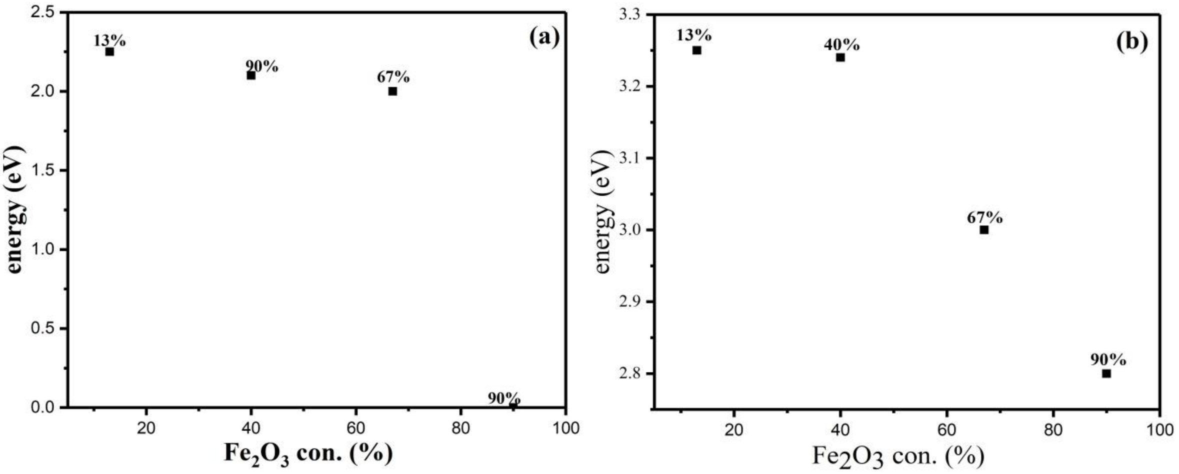

Figure 4.26: the shifting amount of energy peaks of transition as a function of $Fe_2O_3$ concentration of energies (a) 2.25 eV and (b) 3.25 eV.

The MCD spectra confirmed the insights obtained from the crystal structure and magnetic properties of these films, which were mentioned in §4.3.

## 4.4 Conclusions:

The analysis of the structural, magnetic and magneto-optics properties of iron-oxides prepared using PLD technique revealed a dependence on 1) the oxygen pressure and 2) the annealing temperature of the target preparation. The variation in these parameters resulted in significant differences in the crystal structure of the constituent oxides in these films. The characterisation of the films prepared from the hematite target at high temperatures up to 1200 ˚C. The films grown in base pressure showed a structure of wustite with small amount of magnetite. The amount of magnetite increased with increasing the oxygen pressure up to 100 mTorr. This was further indicated by the magnetic properties of these films, which showed a saturation magnetisation of 71 emu/cm$^3$ and 470 emu/cm$^3$ for $\mathbf{A_1}$ and $\mathbf{A_2}$ films, respectively. This suggests an increase in the $Fe_3O_4$ content with increasing the oxygen pressure. The magnetic properties values are shown in table 4.3.

The second hematite target was prepared at 500 ˚C and it showed that the magnetite decreased with increasing the oxygen pressure during the ablation with an increased amount of maghemite. This was confirmed by XANES analysis, which suggested an increase in the $Fe^{3+}$ ions with increasing the oxygen pressure and hence a higher $Fe_2O_3$ content. This was supported by the increase in the saturation magnetisation of these films with increasing the oxygen pressure, as shown in table 4.3.

Further analysis through ZFC/FC to the films studied in the work showed that the films that contain hematite have a lower magnetisation with decreasing their temperature, as a result of Morin transition. The Verwey transition in the ZFC data was found in the films that contain magnetite to decrease with increasing the maghemite content. The MCD spectral features were observed at 2.2 and 3.2 eV for $\mathbf{A_2}$ and $\mathbf{B_1}$ films. These features are related to magnetite phase. These spectra also indicated a high magnetisation of magnetite compared to the antiferromagnetic wustite and hematite. However, the effect of maghemite was observed in the feature shift at 3.2 eV, while the feature disappeared at 2.2 eV in $B_4$ film, which has a 90% maghemite.

According to these results, the FeO thin film could be prepared by PLD from hematite target annealed at high temperature up to 1200 °C with oxygen pressure 0.03 mTorr. Magnetite thin film could be prepared by either use of the previous target, which was used to prepare FeO, with high oxygen pressure (100 mTorr) or from target of hematite annealed at 500 °C with low oxygen pressure (0.03 mTorr). However, maghemite thin films could be prepared from hematite target, which are annealed at 500 °C, with high oxygen pressure more than 100 mTorr.

These insights are important to preparation of pure YIG thin films that are necessary to contain only $Fe^{3+}$ iron ions (as will be discussed in Chapter 5). This is likely to be achieved by using high oxygen pressure during the ablation, which was demonstrated in this chapter to have a positive effect on the saturation magnetisation and magneto-optics properties of the films obtained. The structural, magnetic and magneto optical properties for all films are listed in table 4.3.

Table 4.3: structural, magnetic and magneto- optics properties for iron oxides thin films grown by PLD.

| **Film NO.** | $P_{O2}$ **(mTorr)** | ***t*** **(nm)** | **FeO con. (%)** | **$Fe_3O_4$ con. (%)** | **$Fe_2O_3$ con. (%)** | **$M_s$ 300K ($emu/cm^3$)** | **$M_s$ 5K ($emu/cm^3$)** | **$H_c$ 300K (Oe)** | **$H_c$ 5K (Oe)** | **MCD energy peak of $Fe_3O_4$** | **MCD energy peak of $Fe_2O_3$** |
|---|---|---|---|---|---|---|---|---|---|---|---|
| **$A_1$** | Base | 150 ±5 | ~ 94 (XRD) | 5.3 (XRD) | - | 71 ±0.2 | 64 ±0.3 | 650 ±0.2 | 1100 | 2.2<br>3.2 | - |
| **$A_2$** | 100 | 150 ±4 | - | ~100 (XRD) | - | 470 ±0.5 | 495 ±0.2 | 240 ±0.1 | 1120 | 2.3<br>3.2 | - |
| **$B_1$** | base | 100 ±3 | - | 87 (XANES) | 13 (XANES) | 78 ±0.3 | 80 ±0.5 | 267 ±0.3 | 775 | 2.25<br>3.25 | - |
| **$B_2$** | 0.1 | 100 ±5 | - | 60 (XANES) | 40 (XANES) | 110 ±0.2 | 123 ±0.3 | 354 ±0.3 | 777 | 2.2<br>3.25 | - |
| **$B_3$** | 10 | 100 ±2 | - | 42 (XANES) | 67 (XANES) | 264 ±0.2 | 232 ±0.4 | 29 ±0.5 | 60 ±0.2 | 2.2 | 3 |
| **$B_4$** | 100 | 90 ±5 | - | 10 (XANES) | 90 (XANES) | 398 ±0.4 | 389 ±0.1 | 36 ±0.2 | 42 ±0.1 | - | 2.8 |

## 4.5 References:

1- Khatavkar, S. N., and S. D. Sartale. *Journal of Solid State Electrochemistry* **21.9** (2017): 2555-2566.

2- Santos, Benito, *et al*. *Journal of Physics: Condensed Matter* **21.31** (2009): 314011.

3- Gheisari, M., *et al*. *Journal of Magnetism and Magnetic Materials* **320.21** (2008): 2618-2621.

4- Liu, P., Cai, W. and H. Zeng. *The Journal of Physical Chemistry C* **112.9** (2008): 3261-3266.

5- Seki, M., *et al*. *Applied Physics Letters* **105.11** (2014): 112105.

6- Abreu, G. J. P., Paniago, R. and H-D. Pfannes. *Journal of Magnetism and Magnetic Materials* **349** (2014): 235-239.

7- Welberry, T. R., Goossens, D. J. and A. P. Heerdegen. *Mineralogical Magazine*; **78** (2005): 373–385.

8- Radpour, M., Masoudpanah, S. M. and S. Alamolhoda. *Ceramics International* **43.17** (2017): 14756-14762.

9- Swiatkowska-Warkocka, Z., *et al*. *The Journal of Physical Chemistry C* **121.14** (2017): 8177-8187.

10- Zhang, J., *et al*. *Journal of Magnetism and Magnetic Materials* **432** (2017): 472-476.

11- McNab, T. K., Fox, R. A. and A. J. F. Boyle. *Journal of Applied Physics* **39.12** (1968): 5703-5711.

12- Mirabello, G., Lenders, J. and N. Sommerdijk. *Chemical Society Reviews* **45.18** (2016): 5085-5106.

13- Paramês, M. L., *et al*. *Applied surface science* **252.13** (2006): 4610-4614.

14- Řezníček, R., *et al*. *Physical Review* B **96.19** (2017): 195124.

15- Neal, J. R., *et al*. *Journal of Magnetism and Magnetic Materials* **310.2** (2007): e246-e248.

16- Tarnawski, Z., *et al*. *Acta Physica Polonica-Series A General Physics* **106.5** (2004): 771-776.

17- Jackson M., *et al*. *The IRM quarterly winter*, Vol. **20** (2011): No. 4.

18- Sena, S. P., *et al*. *Journal of Magnetism and Magnetic Materials* **176.2-3** (1997): 111-126.

19- Özdemir, Ö., Dunlop, D. J., and B. M. *Moskowitz. Geophysical Research Letters* **20.16** (1993): 1671-1674.

20- Mokhtari, A., *et al*. *Iranian Journal of Physics Research* 15.3 (2015).

21- Fontijn, W. F. J., *et al*. *Physical Review B* **56.9** (1997): 5432.

22- Liu, H., and C. Di Valentin. *The Journal of Physical Chemistry C* **121.46** (2017): 25736-25742.

23- Zhang, X., Schoenes, J. and P. Wachter. *Solid State Communications* **39.1** (1981): 189-192.

24- Dedkov, Y. S., Rüdiger, U. and G. Güntherodt. *Physical Review B* **65.6** (2002): 064417.

25- Al-Kuhaili, M. F., M. Saleem, and S. M. A. Durrani. *Journal of alloys and compounds* 521 (2012): 178-182.

26- Chirita, M., *et al*. *Chem. Bull* **54.68** (2009): 1-8.

27- De Castro, A. R. B., *et al*. *Journal of magnetism and magnetic materials* **231.2** (2001): 287-290.

28- Wu, Wei, *et al*. *Science and technology of advanced materials* **16.2** (2015): 023501.

29- Lassoued, A., *et al*. *Journal of Molecular Structure* **1141** (2017): 99-106.

30- Bowles, J., M. Jackson, and S. K. Banerjee. *IRM Quart* **20** (2010): 1-10.

31- Ellis, D. S., *et al*. *Physical Review B* **96.9** (2017): 094426.

32- Bødker, F., *et al*. *Physical Review B* **61.10** (2000): 6826.

33- Kant, R, Kumar, D. and V. Dutta. *RSC Advances* **5.65** (2015): 52945-52951.

34- Tepper, T., C. A. Ross, and G. F. Dionne. *IEEE transactions on magnetics* **40.3** (2004): 1685-1690.

35- Huang, X. L., Y. Yang, and J. Ding. *Acta materialia* **61.2** (2013): 548-557.

36- Shokrollahi, H. *Journal of Magnetism and Magnetic Materials* **426** (2017): 74-81.

37- Tepper, T., *et al*. *Journal of applied physics* **93.10** (2003): 6948-6950.

38- Kelm, K., and W. Mader. *Zeitschrift für Naturforschung B* **61.6** (2006): 665-671.

39- Tepper, T., and C. A. Ross. *Journal of applied physics* **91.7** (2002): 4453-4456.

40- Edelman, I., *et al*. *Journal of Applied Physics* **112.8** (2012): 084331.

41- Heald, S., *et al*. *Journal of Synchrotron Radiation* **8.2** (2001): 342-344.

42- Pernicone, N., *et al*. *Applied Catalysis A: General* **251.1** (2003): 121-129.

43- Schmuki, P., *et al*. *Journal of the Electrochemical Society* **143.2** (1996): 574-582.

44- Medvedeva, I., *et al*. *Journal of Nanoparticle Research* **14.3** (2012): 740.

45- Swiatkowska-Warkocka, Z., *et al*. *Nanoscale research letters* **6.1** (2011): 226.

46- Huang, X., and J. Ding. *Journal of the Korean Physical Society* **62.12** (2013): 2228-2232

47- Carlut, J., *et al*. *Frontiers in Earth Science* **3** (2015): 18.

48- Lei, W., *et al*. *Physics Letters A* **381.4** (2017): 314-318.

49- Zhang, X., Schoenes, J. and P. Wachter. *Solid State Communications* **39.1** (1981): 189-192.

50- Gehring, G. A., *et al*. *Journal of Magnetism and Magnetic Materials* **324.21** (2012): 3422-3426.

51- Hiraoka, N., *et al*. *The European Physical Journal B-Condensed Matter and Complex Systems* **70.2** (2009): 157-162.

52- Bentivegna, F., *et al*. *Journal of applied physics* **85.4** (1999): 2270-2278.

# 5. YIG thin films

## 5.1 Introduction:

Yttrium iron garnet (YIG) thin films were grown on gadolinium gallium garnet (GGG) and yttrium aluminium garnet (YAG) substrates at different oxygen pressure using PLD technique. The effect of the oxygen pressure on the structural properties of these films was studied using XRD and XANES. SQUID magnetometer was used to study the properties of these films at different temperatures. Furthermore, the crystal field transitions of the YIG films were studied using an MCD technique. This was accompanied by an investigation of the effect of decreasing temperature on these transitions. The aims of this study is to prepare YIG thin films by PLD with lower cost and higher properties compared to the previous work. The structural and magnetic properties are required to be close to the bulk YIG properties with saturation magnetisation $M_s$ ~143 emu/cm$^3$ and coercivity $H_c$ less than 1 Oe in order to be useful for spintronics and magnonics applications.

In this chapter, a brief review of previous studies on YIG thin films will be presented and followed by the main experimental results of the current work.

## 5.2 YIG previous work:

YIG has a chemical composition of $Y_3Fe_5O_{12.}$ It is the most widely used ferrimagnetic insulator and it became promising for spintronic applications since its first discovery in 1956. For example, it is used as a spin transport medium due to its low damping and long spin-waves [1, 2]. In addition, it is widely used in microwave applications as a capacitor and an isolator because of its low dielectric loss in microwave region, having a high Faraday rotation (~ 214 degree cm$^{-1}$ at 1310 nm) and transmittance (~95%) in IR radiation [1,3]. Other unique properties for YIG are the high melting point (~1555 ˚C), saturation magnetisation ($M_s$ of ~143 emu/cm$^3$), resistivity ($\rho$ ~ 1×10$^{12}$ Ωcm), thermal stability and coercive field ($H_c$ ~1 Oe) [3]. YIG nanoparticles are also used in high density magnetic and magneto optical information storage applications [4].

**5.2.1 Structural properties:**

YIG is an insulator material and has a complex cubic structure with 8 formula units per unit cell and a lattice constant of $a$= 12.376Å. The chemical formula of YIG is written as $\{Y^{3+}\}_3[Fe^{3+}]_2(Fe^{3+})_3O^2{}_{12}$; where YIG has three main groups of sites, as shown in fig. 5.1. It has 24 dodecahedral *c*-sites of $\{Y^{3+}\}$. They are referred to as a dodecahedral because the $Y^{3+}$ is surrounded by 8 oxygen ions to form a dodecahedron. Secondly, it has 16 octahedral a-sites of $[Fe^{3+}]$ where each *a*-site coordinates with 6 oxygen ions to form an octagon. Finally, it has 24 tetrahedral *d*-sites of $(Fe^{3+})$ surrounded by 4 oxygen ions and forming a tetrahedron. In addition, each octahedral site has 6 neighbours of tetrahedral sites and each tetrahedral site has 4 neighbours in octahedral site [5, 6]. Each oxygen ion has two $Y^{3+}$ ions neighbours: one tetrahedral iron ion and one octahedral iron ion.

Figure 5.1: An illustration of complex crystal structure of YIG. The red spheres represented the iron ions. The greys are the yttrium ions, the white are oxygen ions [7]. Courtesy of Northeastern University Boston.

### 5.2.2 Magnetic properties:

YIG is a ferrimagnetic material below its Curie temperature $T_c$=560 K, with a high $M_s$= 143 emu/cm$^3$ and relatively low $H_c$ (~1Oe) [1, 8]. This magnetisation comes from the 3$d^5$ ions in the tetrahedral (*a*) sites and octahedral [*d*] sites. The super-exchange interaction occurs due to the intermediation of the O$^{2-}$ ions between the Fe$^{3+}$ ions and this is responsible for the magnetic ordering of iron spins in YIG. There are three super-exchange interactions in YIG: the interaction between *a*-*a* sites and between *d*-*d* sites (more details about the super-exchange were presented in §2.4.1). These interactions are weak inter-sublattice interaction. The last interaction is the one between *a*-*d* sites, which is the dominant interaction. Figure 5.2a illustrates the interaction in the ground state of the system when the two electrons of oxygen are in a singlet state and the interaction between F$^{3+}$ ions is neglected. At first excited state, one electron can be transferred from oxygen to one of the iron ions. In this case, there are two possibilities of states. Firstly: the spin *S*=5 and the second oxygen electron is parallel to the unaffected iron ions, which is shown in fig. 5.2b. Secondly, $S$=0 when the oxygen electron is antiparallel to the unaffected iron ion, as illustrated in fig. 5.2c. In the latter possibility, a singlet state is likely to be created, which has a lower energy [9]. Hence, the superexchange interaction is antiferromagnetic. This is between one octahedral and one tetrahedral iron through the intervening oxygen.

Figure 5.2: An illustration of the super-exchange interaction of YIG [9]. Courtesy of Ohio State University.

The magnetisation of YIG comes from the opposite magnetic sub-lattices and represents the difference between the magnetisation of the ferromagnetic tetrahedral $Fe^{3+}$ sites ($M_d$) and the ferromagnetic magnetisation of the octahedral $Fe^{3+}$ sites ($M_a$), which can be represented by:

$$M_s(T) = 3M_d(T) - 2M_a(T) \quad \text{(per formula unit)} \tag{5.1}$$

As a result, YIG has a magnetic moment of $5\mu_B$ per formula unit at $T$=0 K. This temperature dependence of the magnetisation of YIG is an example for Neel molecular field theory of ferrimagnetism, which states:

"All super-exchange interaction of the inter sub-lattice, $J_{dd}$, $J_{aa}$ and $J_{ad}$ are antiferromagnetic but under the impact controlling of $J_{ad}$, the two sublattices are aligning antiparallel".

This leads to the ferrimagnetic behaviour of YIG. However, the magnetic moments of the same sub-lattice align ferromagnetically [1, 5, 10]. This process is illustrated in fig. 5.3.

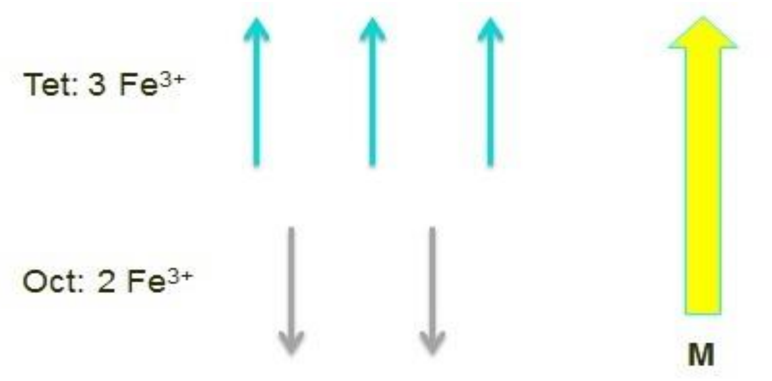

Figure 5.3: A sketch of the octahedral Fe$^{3+}$ site that has two magnetic moments aligning opposite to the three magnetic moments of the tetrahedral Fe$^{3+}$site and the magnetisation of the YIG is determined by the tetrahedral site.

This study focused on growing YIG thin films to be used in applications that benefit from YIG properties, mentioned earlier. Choosing the most suitable substrate to grow epitaxial YIG thin film is of high importance. GGG substrate is commonly used in YIG films due to its crystal structure, which is very close to pure YIG structure [1]. There are many factors that affect the properties of YIG thin films in addition to the substrate type, such as: oxygen pressure, substrate temperature, annealing temperature and laser energy for PLD [8].

Naresh *et al* [11] have grown YIG thin films by PLD using a target made of YIG powder. The films were grown on quartz and GGG substrates at temperatures higher than 800 ˚C. There were no sharp peaks in the XRD pattern for the films grown at different substrate temperature ($T_s$) in range of room temperature to 850°C without annealing (fig. 5.4a). This was suggested to be a consequence of the nanocrystalline structure of the samples. To increase the YIG grain size in the film, they suggested annealing the sample after deposition. Several factors could affect the grain growth of the YIG film such as: the substrate type and the deposition condition. Furthermore, the substrate temperature is not sufficient to control grain growth [11].

The XRD spectra were studied for the films grown at $T_s$ range 500-850 °C and annealed at 700°C, as shown in fig. 5.4b. The magnetisation of the films showed that the film annealed above 850 ˚C is the only film that had a magnetisation (fig. 5.5). $M_s$ of these films increased with increasing annealing temperature. However, the films grown on quartz had magnetisation lower than the magnetisation of the films that were grown on GGG due to the poor lattice mismatching between the quartz and YIG. The film that was grown on GGG had smaller $M_s$ than bulk YIG (~96 emu/cm$^3$) [11].

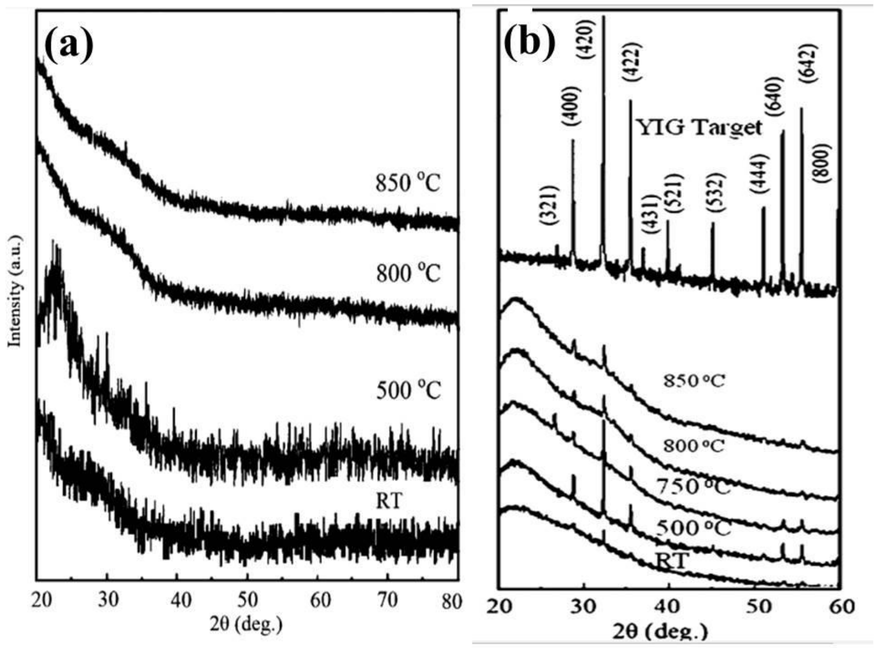

Figure 5.4: XRD pattern of YIG thin films grown at different $T_s$ on quartz substrate (a) without annealing and (b) the films annealed at 700 °C compared with the YIG target [11]. Reprinted with permission of Journal of Magnetism and Magnetic Materials.

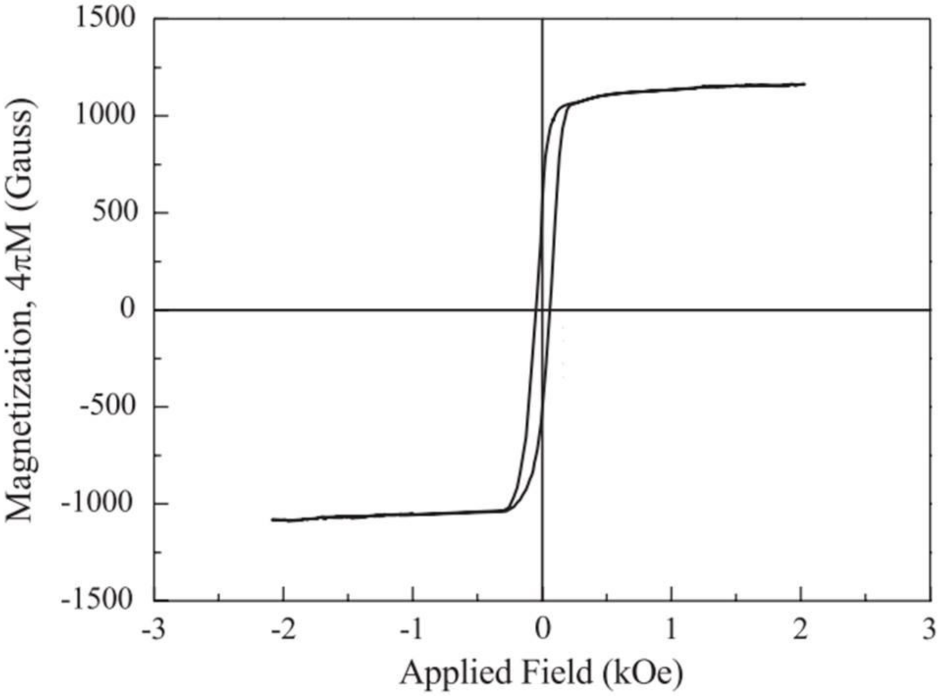

Figure 5.5: *M-H* loop for YIG thin film grown with $T_s$=850°C and $T_{ann}$= 700°C (1 Gauss= 0.08 emu/cm$^3$) [11]. Reprinted with permission of Journal of Magnetism and Magnetic Materials.

Bhoi *et al* had grown YIG thin films on GGG substrates by PLD from a YIG target. For all films, the substrate temperature was 750 ˚C and the films were annealed after ablation at 700 ˚C. The oxygen pressure used in this study was ~370 mTorr and two different laser energies were used for the PLD (240 mJ and 350 mJ). The results showed that the film grown at higher laser energy have $M_s$ close to the bulk sample. However, lower laser energy produced films with $M_s$ less than the bulk YIG (fig. 5.6) [8]. The film grown at high energy had $Ms$= 1520 G ~ 121 emu/cm$^3$. However, the film was grown in low laser energy had lower $M_s$ = 1030 G~ 82 emu/cm$^3$. This indicates that $M_s$ decreases with increasing the laser energy due to the presence of high amount of grain phase boundary with the low laser energy [8].

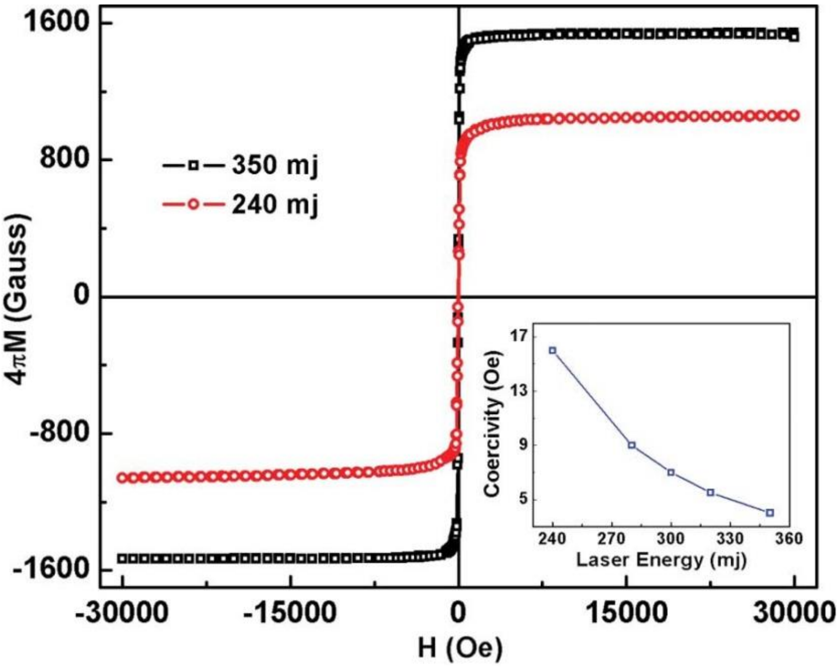

Figure 5.6: The *M-H* loops for two different YIG film on GGG substrates were grown at different laser energy [8]. Reprinted with permission of IEEE Transactions on Magnetics.

Onbasli *et al* studied the magnetic properties of YIG thin films with different thickness grown on GGG (100) substrates made from a target of mixed $Fe_2O_3$ and $Y_2O_3$ powders [12]. The films were ablated using PLD with an excimer laser (400 mJ pulsed). The substrate temperature was 650 °C and the oxygen pressure was 20 mTorr. The film was cooled at the same oxygen pressure until the substrate temperature reached 200 °C. The films were annealed in air after ablation at 800 °C. The results reported that the film of thickness 96 nm had an $M_s$ of 137 emu/cm$^3$ (fig. 5.7), which is slightly less than $M_s$ of bulk YIG. This magnetisation decreased with increasing the film thickness. $H_c$ varied but generally was below 2 Oe, as shown in fig. 5.7b. This low $H_c$ makes YIG an useful soft magnet material. The low $H_c$ of the YIG can be used in microwave applications. The magnetic properties were studied by using a vibrating sample magnetometer technique [12].

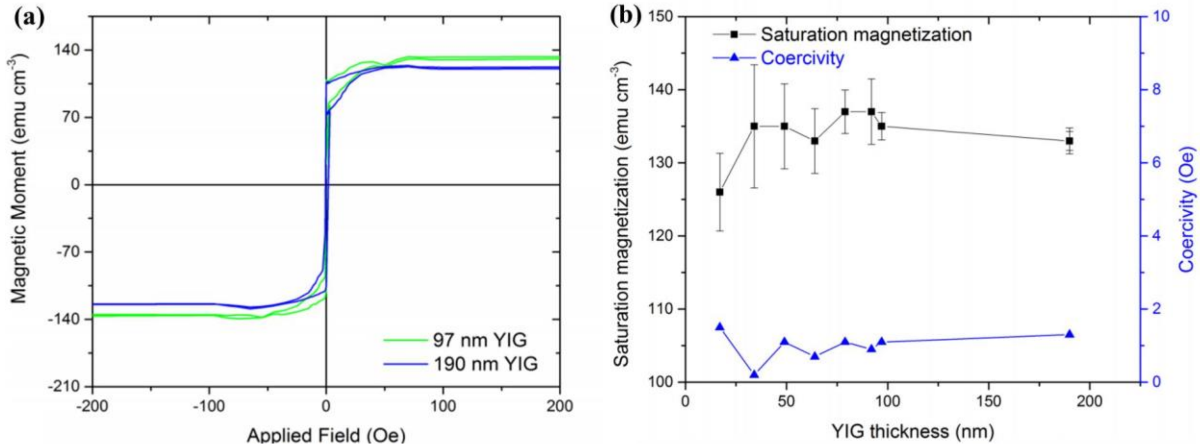

Figure 5.7: (a*) M-H* loops for YIG/GGG thin films with thicknesses of 97 and 190 nm at room temperature and (b) $M_s$ and $H_c$ of YIG thin films as a function of film thickness [12]. Reprinted with permission of APL Materials.

YIG nanoparticles show superparamagnetic behaviour. Rajendran *et al* measured $M_s$ for different YIG nanoparticle sizes. This study reported that $M_s$ dropped with decreasing the grain size down to a grain size of 14 nm. For particle sizes less than 14 nm; the sample showed no saturation magnetisation at room temperature [4].

### 5.2.3 Optical and magneto-optical properties:

Pure YIG has a band gap structure, which is determined by using the optical measurements [13]. The conduction band of YIG made from overlapping four delocalized $Fe^{3+}$ 3d-subbands (fig. 5.8). However, the valence band made from a broad oxygen band and two narrow $Fe^{3+}$ bands. The energy gap between the conductive and valence band found to be ~2.8 eV. YIG is used in microwave applications due to its low absorption to the microwave signal [11, 14].

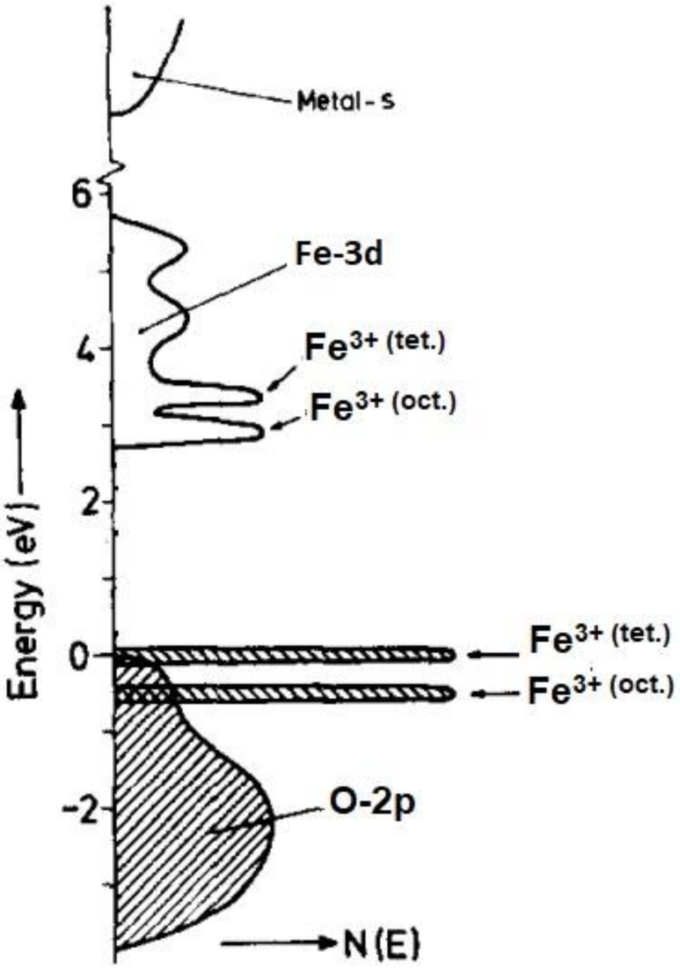

Figure 5.8: The band gap structure of YIG. The valence band is the hatched area, which is indicated the state is filled at $T$=0 [14]. Reprinted with permission of Journal of Solid State Chemistry.

The MCD measurements of YIG thin films are important to determine the electronic transition in YIG. In addition, it is relatively easier method than Faraday rotation (FR) to explain the localized nature of the absorption [15]. The absorption and magneto-optical properties of bulk YIG were reported by Scott *et al* [15]. They measured the MCD and FR and absorption spectra for bulk crystal YIG with thickness of 2 μm. Table 5.1 shows the magneto-optics features of the YIG crystal and the transition, which is indicated for each feature. They reported that the magneto-optics measurement is more complex and give more details about the transition than the absorption spectra, which are straight spectra as shown in fig. 5.9a. They also performed the MCD spectra of YIG thin film prepared on GGG substrate by *rf*-sputtering (fig. 5.9b). The YIG thin films had same magneto-optical properties as the bulk YIG. The magneto-optics properties of YIG have absorption bands all paramagnetic except one below 3.5 eV [15].

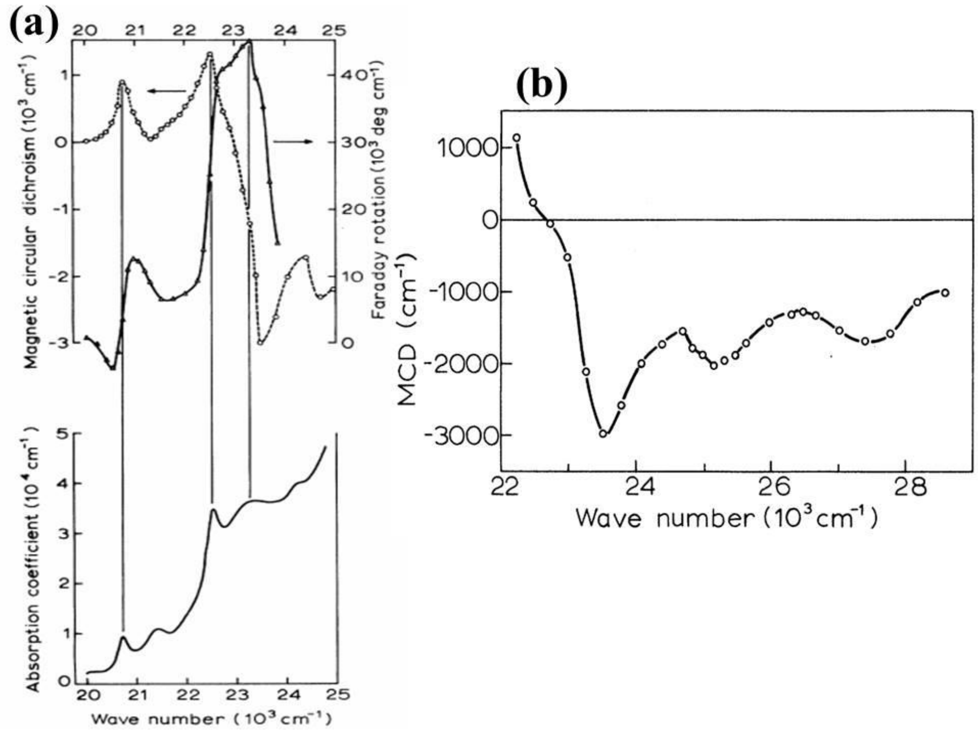

Figure 5.9: (a) FR, MCD and absorption spectra for bulk YIG in energy range (20- 25) $10^3$ cm$^{-1}$ ~ (2.48- 3.2) eV at 77 K, and (b) MCD spectrum of YIG thin film at 77 K (1000 cm$^{-1}$~ 0.124 eV) [15]. Reprinted with permission of American Physical Society.

Table 5.1: Magneto optical transition of bulk YIG. The feature is positive (+) and the feature is negative (-) [15]:

| Energy | Energy | Line shape | | Band assignment |
|---|---|---|---|---|
| ($cm^{-1}$) | ~ (eV) | Paramagnetic | Diamagnetic | |
| 10400 | 1.3 | + | | |
| 10920 | 1.4 | + | | $^6A_{1g}(^6S)\rightarrow {}^4T_{1g}(^4G)$ |
| 11420 | 1.42 | + | | |
| 13500 | 1.7 | + | | |
| 14090 | 1.75 | - | | $^6A_{1g}(^6S)\rightarrow {}^4T_{2g}(^4G)$ |
| 14870 | 1.84 | - | | |
| 16050 | 1.98 | + | | |
| 16500 | 2.04 | + | | |
| 16840 | 2.1 | - | | $^6A_1\ (^6S)\rightarrow {}^4T_1\ (^4G)$ |
| 17380 | 2.15 | + | | |
| 18200 | 2.26 | + | | |
| 18550 | 2.3 | + | | |
| 19100 | 2.37 | - | | $^6A_1\ (^6S)\rightarrow {}^4T_2\ (^4G)$ |
| 19600 | 2.43 | + | | |
| 20700 | 2.57 | + | | $^6A_1\ (^6S)\rightarrow {}^4E;\ {}^4A_1(^4G)$ |
| 21500 | 2.7 | + | | $^6A_{1g}\ (^6S)\rightarrow {}^4E_g;\ {}^4A_{1g}(^4G)$ |
| 22500 | 2.8 | + | | $^6A_{1g}\ (^6S)\rightarrow {}^4T_{2g}\ (^4D)$ |
| 23250 | 2.9 | | + | Biexciton or $Fe^{3+}$- $Fe^{3+}$ charge transfer |
| 25200 | 3.12 | - | | Biexciton |
| 27500 | 3.41 | - | | Biexciton |

The transitions that occur in YIG crystal were also explained by Wood *et al* [16]. They observed that in visible spectra range; the crystal field transitions occur due to a weak spin forbidden of $Fe^{3+}$ ions. In the lower energy region, the following transitions of the octahedral $3d^5$ occurred at $^6A_{1g}$-$^4T_{1g}$ and $^6A_{1g}$-$^4T_{2g}$, as shown in fig. 5.10. However, the transitions on tetrahedral $Fe^{3+}$ ions require energy higher than of the octahedral $Fe^{3+}$ ions due to lower crystal field coordination for the tetrahedral coordination. In addition, the tetrahedral $Fe^{3+}$ ions are not parity forbidden and they are higher in oscillator strength [16].

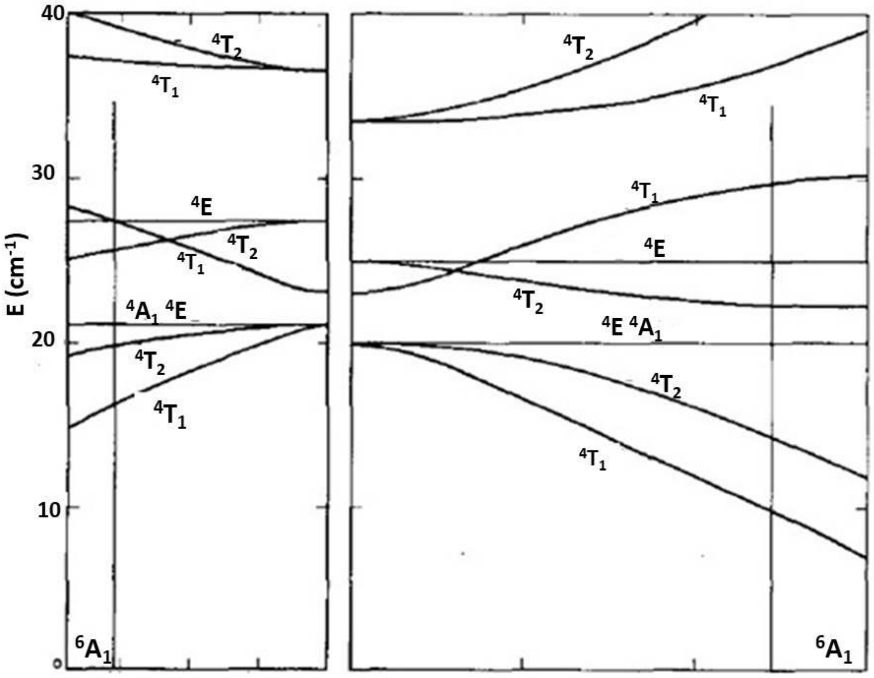

Fig 5.10: The crystal field transition of YIG crystal on (left) the octahedral sites (right) the tetrahedral sites, A, E and T is sub-bands in solid number of d band [16]. Reprinted with permission of Journal of Applied Physics.

## 5.3 Results and discussion:

### *5.3.1 Samples preparation:*

The target used in this study was prepared by mixing yttrium oxide ($Y_2O_3$) powder with iron oxide ($\alpha$-$Fe_2O_3$) powder with the predetermined ratios according to following method:

*YIG thin films*

$$3Y_2O_3 + 5Fe_2O_3 \rightarrow 2Y_3Fe_5O_{12}$$

The atomic weight of $Y_2O_3$ $(At.wt)_{Y2O3}$ = 225.82 g/mol and $(At.wt)_{Fe2O3}$= 159.7 g/mol.

Hence, 3x$(At.wt)_{Y2O3}$ of $Y_2O_3$+ 5x$(At.wt)_{Fe2O3}$ of $Fe_2O_3$= 677.47 g of $Y_2O_3$ needs 798.5 g of $Fe_2O_3$ to have YIG. This means a 1 g of $Y_2O_3$ needs 1.1787 g of $Fe_2O_3$.

The target contained 4 gm of $Y_2O_3$ with 4.7148 g of $Fe_2O_3$. The two types of powders were purchased from Alfa Aesar with purity of 99.99%. The powder mixture was mixed by pestle and mortar for 15 min. Then, the mixture was sintered in an air furnace at 1200 ˚C for 10 hours. This step was repeated twice and the powder colour changed from light red to light grey. The powder was then pressed into a disc of diameter 25 mm that was annealed in an air furnace at 1200 ˚C for 15 hours. Another target was made earlier by same method, powders and ratios but with $T_{ann}$ of 500 °C for both the powder and the target (same annealing temperature was used in Chapter 4). This target was powdery and it broke up in the chamber during the ablation.

Different types of 4×4 mm substrates were used, such as sapphire ($Al_2O_3$) (0001), gadolinium gallium garnet (GGG) (100) and aluminium gallium garnet (YAG) (100), which all are obtained from PI-KEM Ltd, all were two side polished. The films grown on sapphire showed no peaks in their XRD spectra. In addition, they showed non-magnetic characteristics in their SQUID measurements. This indicates an amorphous nature in these films. The results from these films are not included hereafter.

The thin films of this study were grown at oxygen pressures 100, 400 and 500 mTorr and with substrate temperature of 500 ˚C. Then, the films were annealed in air at different temperature up to 1400 ˚C. There was no magnetism for the films annealed below 900 ˚C and the films evaporated when they were annealed at temperatures higher than 1200 ˚C. The highest quality films were the films annealed at 1000 ˚C. Therefore, all the films studied in this work were annealed in air at 1000 ˚C for 4 hours after ablation. The YIG films were grown in high oxygen pressure (100, 400 and 500 mTorr) in order to maintain the iron ion of $Fe^{3+}$.

### *5.3.2 Structure properties:*

Figure 5.11 shows the XRD patterns for the YIG/ GGG thin films, which were grown with $P_{O2}$=100, 400 and 500 mTorr, and YIG/YAG thin film, which was grown at $P_{O2}$= 400 mTorr. These patterns suggest that all the films are likely to be epitaxial. The peaks at 2θ ~ 28.82° and 60.9° matched the (400) and (800) planes of GGG substrates, respectively (fig. 5.11a-c). The peaks of YIG thin film on GGG with $P_{O2}$= 400 mTorr at 2θ = 28.8° and 59.6° matched the peaks of YIG with orientation of (400) and (800), respectively (Fig 5.11b). However, YIG thin film on GGG substrate with $P_{O2}$= 100 mTorr showed one peak that matches with YIG only with orientation of (400) at 2θ= 28.48°. For the film grown with $P_{O2}$= 500 mTorr, the peaks at 2θ= 28.72° and 59.54°, as show in fig. 5.11c. However, the peaks of XRD spectra (fig. 5.11d) at 2θ of 30.0° and 62° appear to match the YIG with orientation (400) and (800), respectively.

None of the peaks in the studied films indicated the presence of iron phases. This suggests that if there were any secondary iron phases in these films, it was a negligible amount that cannot be detected by XRD technique.

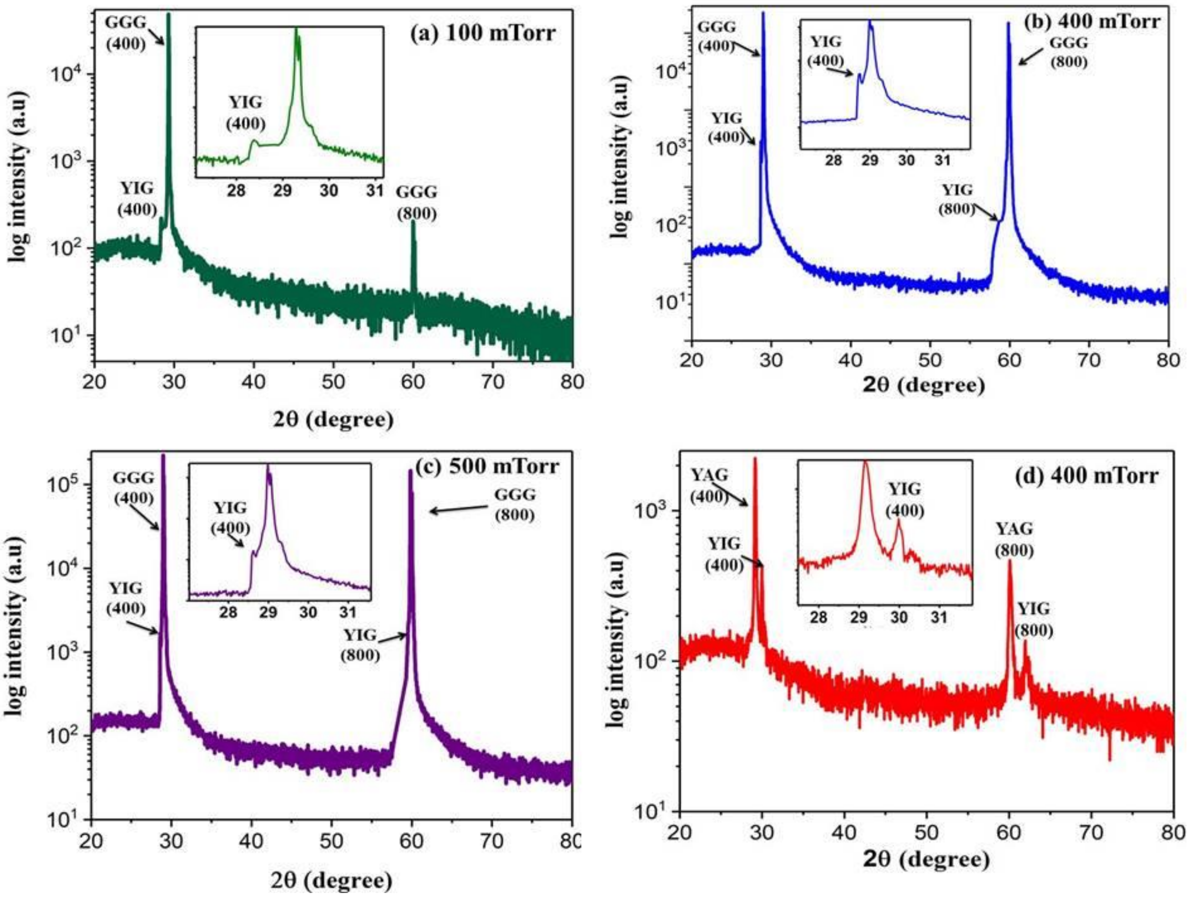

Figure 5.11: The XRD patterns of YIG thin films (a) YIG with P/GGG $P_{O2}$=100 mTorr, (b) YIG/GGG with $P_{O2}$=400 mTorr, (c) YIG/GGG with $P_{O2}$=500 mTorr and (d) YIG/YAG with $P_{O2}$=400 mTorr. The insets show zoom in the peak of YIG (400).

The lattice constant for the films was calculated using Bragg's law (table 5.2). The film was grown in GGG with $P_{O2}$=400 mTorr has a lattice constant $a$=12.385 Å, which is close to the lattice constant of bulk YIG $a$=12.376 Å. The peaks of the film grown on YAG substrate were slightly shifted as shown in fig. 5.11d. The lattice constant of this film is $a$=11.861 Å, which is lower than the bulk YIG. The lattice mismatch between the bulk YIG and the substrates were calculated from equation:

$$lattice\ mismatch = \left|\frac{a_{YIG}-a_{substrate}}{a_{substrate}}\right| \times 100\% \qquad (5.2)$$

$$\varepsilon = \left|\frac{a_{film}-a_{bulk}}{a_{bulk}}\right| \times 100\% \qquad (5.3)$$

and it found to be 0.056% with GGG substrate and 2.28% with YAG substrate. The calculated lattice mismatch between the films and substrates is shown in table 5.2. The least mismatch was for the YIG on GGG film grown with $P_{O2}$= 400 mTorr, which is 0.016%. The strain ($\varepsilon$) is also calculated from equation (5.3) for all films. It shows that the film grown with $P_{O2=}$ 400 Torr on GGG has lowest strain of 0.07%, as shown on table (5.2). However, the film was grown on YAG substrate has the highest value of 3.846 %. The XRD patterns were compared to the YIG powder pattern, which was measured by Rajendran *et al* and it showed a similar XRD spectra of the thin films studied here [4]. The grain size for YIG/YAG can be calculated from Sherrer's equation and it was found to be $D$=29 ±4 nm.

Table 5.2: The structural properties of YIG thin films obtained from Dektak and XRD results, for the peak of orientation (400).

| ***Film NO.*** | $P_{O2}$ ***(mTorr)*** | ***t (nm)*** | ***a (Å)*** | ***Lattice mismatch (%)*** | ***ε (%)*** |
|---|---|---|---|---|---|
| (a) YIG/GGG | 100 | 110±3 | 12.487 ±0.0003 | 1.001 ±0.0001 | 0.90±0.002 |
| (b) YIG/GGG | 400 | 120±3 | 12.385 ±0.0001 | 0.016 ±0.0001 | 0.07±0.003 |
| (c) YIG/GGG | 500 | 120±2 | 12.418± 0.0004 | 0.28 ±0.0001 | 0.34±0.002 |
| (d) YIG/YAG | 400 | 120±2 | 11.861 ±0.0001 | 1.24 ± 0.0004 | 4.16 ±0.001 |

The film grown on GGG with $P_{O2}$=100 mTorr was studied by XAFS in order to detect any secondary iron phases. The XAFS data taken on this film was compared to XAFS data for pure YIG powder, as shown in fig. 5.12. The near edge (XANES) spectrum of this film shows an overlap with the near edge spectrum of YIG powder with small edge shift to lower energy, which indicates the presence of low valence states Fe ions. This shift suggested having an amount of iron metal ion $Fe^0$ in this film. This amount was estimated to have about 6±2% of the film as iron atoms $Fe^0$ [17].

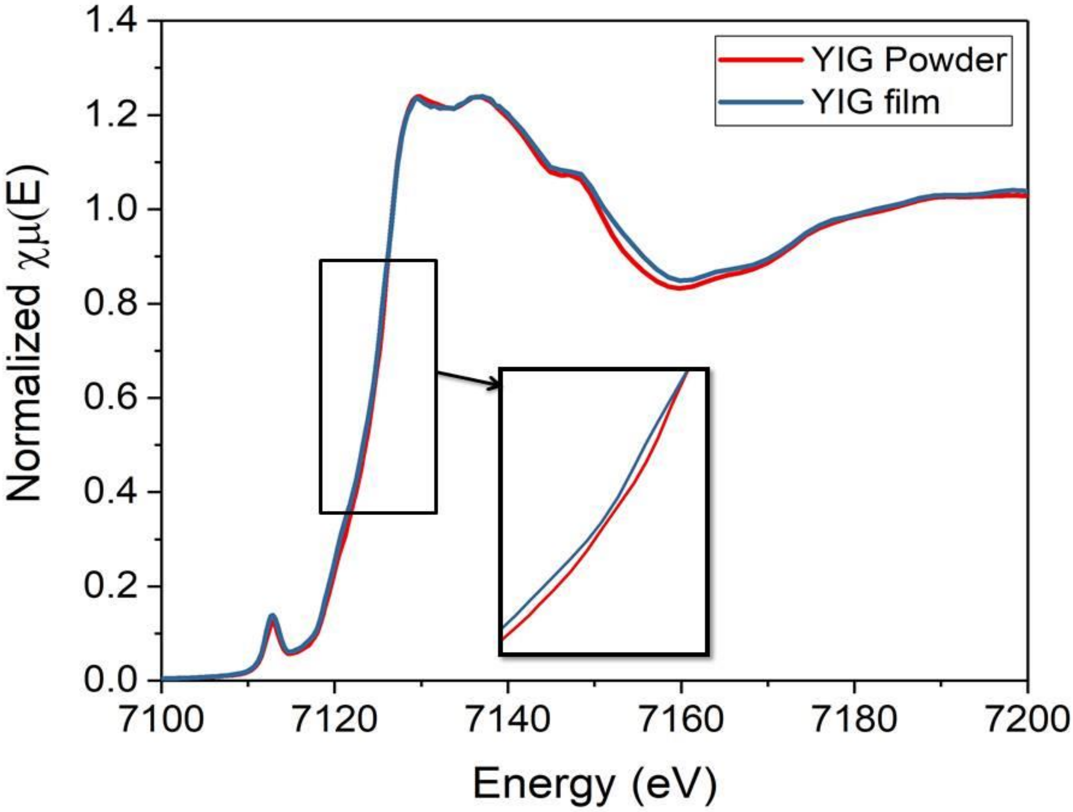

Figure 5.12: XANES measurements for YIG/GGG grown with $P_{O2}$=100mTorr compared with YIG powder.

The XRD analysis of YIG films on GGG or YAG substrates suggested that all the films have YIG structure. XANES spectra suggested having ~6% iron metal ions in YIG/GGG grown with $P_{O2}$=100 mTorr. On the other hand, YIG/GGG thin films grown with $P_{O2}$=400 mTorr have the closest structure to pure YIG with the smallest strain. This is important because low strain means there is high probability that film has properties close to the bulk, which is the aim of this chapter.

### *5.3.3 Magnetic properties:*

The magnetic properties of YIG thin films were studied using SQUID magnetometer at temperature range 5-300K. The magnetisation (*M*) of the films was measured as a function of applied magnetic field ($H$) up to 1000 Oe, which was applied in-plane with the film. This value of applied field is less than the applied field used in iron oxides films (Chapter 4) since YIG saturates below 1000 and $H_c$ less than 1 Oe [18].

The $M$-$H$ loop for YIG/GGG thin film, which was grown with $P_{O2}$=100 mTorr, is shown in fig. 5.13. The linear term from the paramagnetic contribution of the GGG substrate was subtracted. This film shows a clear loop at 300 K and it saturated at $M_s$ = 588 emu/cm$^3$. This $M_s$ is higher than $M_s$ for YIG and all iron oxides. $H_c$ of this film is shown in the inset fig 5.12 and it is about 1.7 Oe, which is slightly higher than what is expected from YIG. Based on XANES measurements, this film may contain YIG with an amount of metallic iron Fe$^o$, which has high $M_s$=1700 emu/cm$^3$ [19].The fraction of metallic Fe was estimated from the magnetisation by using:

$$M_{s\,(total)} = fM_{s\,(Fe)} + (1-f)M_{YIG} \sim 588\ emu/cm^3 \tag{5.4}$$

where $M_{YIG,}$ is the saturation magnetisation of YIG ~ 143 emu/cm$^3$ and $M_{Fe}$ is the saturation magnetisation of metallic Fe, while $f$ is the fraction of metallic Fe in the film. The calculation showed that this film contains about 30% metallic Fe. However, the XANES measurement indicated that the film contains about 6% metallic Fe. That means the magnetisation measurement could be more accurate than XANES in detect the fraction of defects in the film [17].

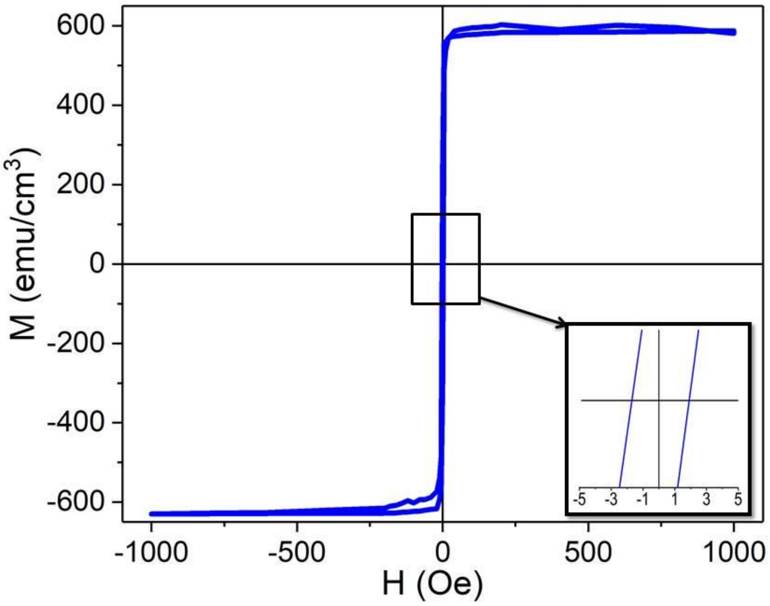

Figure 5.13: The *M-H* loop of YIG thin film grown on GGG substrate with $P_{O2}$= 100 mTorr by PLD. The paramagnetic data from GGG has been subtracted. The inset shows $H_c$ value of the films.

The *M-H* loops of YIG/GGG grown at $P_{O2}$= 400 and 500 mTorr at 300 K are shown in fig. 5.14. The linear term of the paramagnetic contribution of GGG substrates was subtracted. The loops saturated at 143 and 140 emu/cm$^3$, respectively. $M_s$ of these films matches the $M_s$ of bulk YIG, ($M_S$=143 emu/cm$^3$). The film grown at $P_{O2}$=400 mTorr has $H_c$ of 0.7 Oe, which is also in the range of bulk YIG ($H_c$<1 Oe). However, this $H_c$ increased at the film grown at $P_{O2}$ = 500 mTorr to 30.6 Oe, as shown in the inset of fig 5.14. This $H_c$ is higher than the expected values of YIG. This indicates that there is an optimum value of the oxygen pressure to produce YIG films. These results agree with the XRD results, which indicated a high lattice strain in the YIG film grown on GGG substrate with $P_{O2}$ = 500 during the ablation.

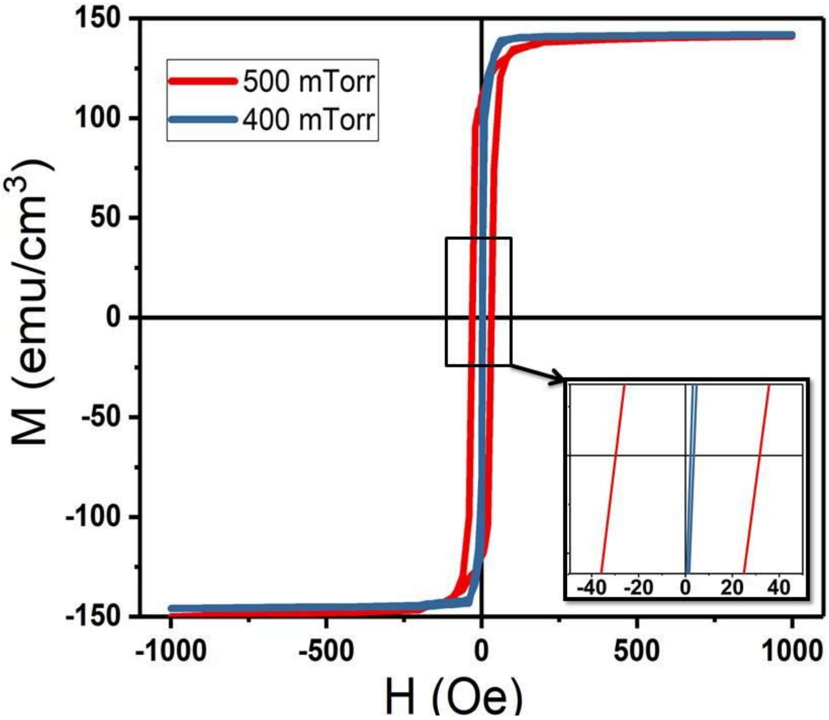

Figure 5.14: The *M-H* loop of YIG thin film grown on GGG substrate with $P_{O2}$= 400 and 500 mTorr by PLD. The paramagnetic data from GGG has been subtracted. The inset shows $H_c$ value of the films.

*M-H* loops were measured at temperatures of 300, 140 and 70 K for YIG/GGG thin film grown at $P_{O2}$ = 400 mTorr. Figure 5.15 shows the temperature dependence of the magnetisation of this film. The substrates signal was subtracted from all measurements. The measurements were taken as a function of applied magnetic field varied between -1000 and 1000 Oe. $M_s$ at 300, 140 and 70 K increased with decreasing the temperature from 143 to 180 and 200 emu/cm$^3$, respectively. This increase is a likely result of the ferrimagnetic material and indicates that all hematite (which was used to make the targets) interacted with $Y_2O_3$. This results also agree with the bulk YIG results obtained by ref [20]. There were no loops at temperatures less than 70 K due to the high paramagnetic effect of GGG substrate, which can be neglected with the currently used SQUID device. $H_c$ of these loops also increased with decreasing the temperature from 0.7 to 32 and 39 Oe due to the increase in the magnetocrystalline anisotropy of the films. Magnetocrystalline anisotropy is strongly dependent on temperature where it decreases with increasing the temperature in ferrimagnetic material and the material becomes isotropic at $T_c$ [21].

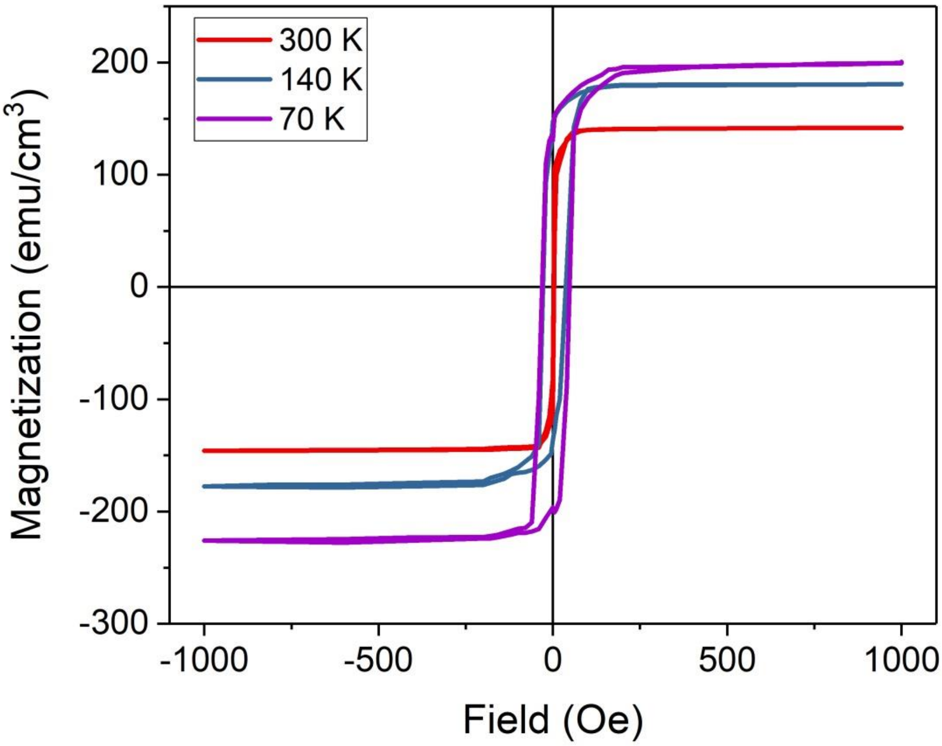

Figure 5.15: M-H loops for YIG/GGG thin film grown with $P_{O2}$ (400 mTorr). The measurements were performed at T of 300, 140 and 70 K with applied magnetic field of 1000 Oe.

YIG thin film were grown on diamagnetic YAG substrate in order to eliminate the effect from paramagnetic GGG at low temperature. The growth of YIG on YAG substrate is an alternative to GGG substrate that has a close structure to YIG. The *M-H* loops for this film are shown in fig. 5.16. The magnetisation of the film saturated at 140 emu/cm$^3$ at 300 K, which is also close to the bulk YIG and close to the film grown in same parameter on GGG. However, $H_c$ is 34.2 Oe, which is higher than expected (table 5.3). This increase in the coercive field is due the lattice strain, which is a result of the lattice mismatch between the YIG film and YAG substrate. The *M-H* loop for the film grown on YAG at 5K has a $M_s$ =

205 emu/cm$^3$, as shown in fig. 5.16. This result indicated that $M_s$ of YIG/YAG thin film increased with decreasing the temperature. This $M_s$ value of YIG/YAG film is slightly higher than $M_s$ of bulk YIG at 5K (~193 emu/cm$^3$) [21-22]. In addition, $H_c$ increased up to 63 Oe with decreasing the temperature to 5K, as shown in the inset in fig 5.16.

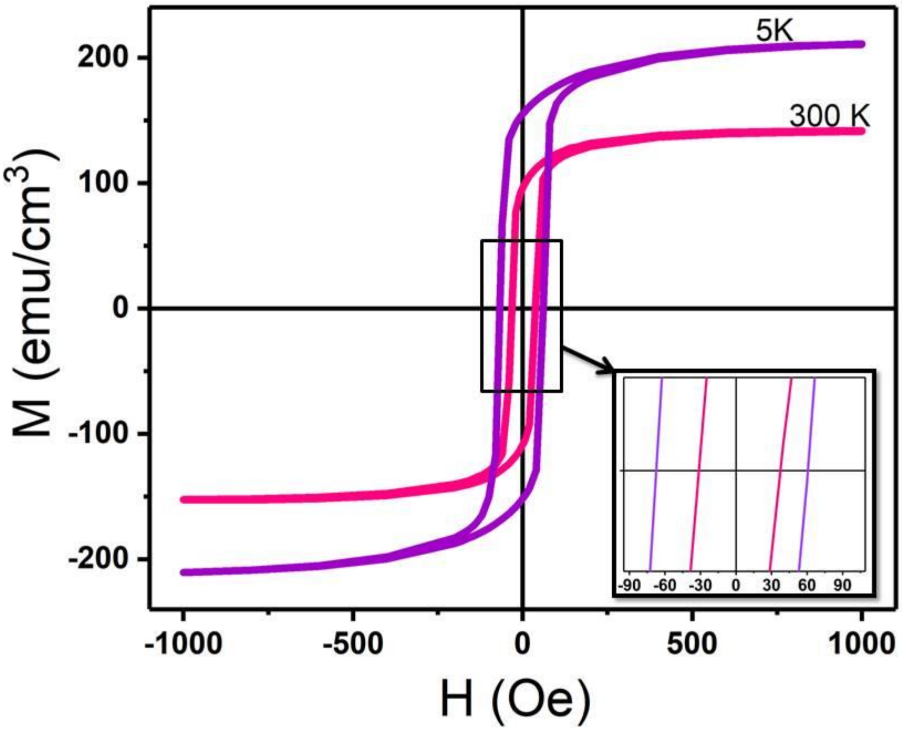

Figure 5.16: The *M-H* loops of YIG thin film grown on YAG substrate at 300 and 5K. The diamgnetic data from YAG substrate has been subtracted. The inset shows $H_c$ value of the films.

The ZFC and FC magnetisation measurements of YIG/YAG thin films were performed using SQUID in a temperature range between 5-350 K (fig. 5.17). The ZFC measurement was performed in the absence of magnetic field whereas FC was performed in the presence of an applied magnetic field of 100 Oe. These measurements were performed to study the effect of thermal flactuations on the magnetisation. ZFC and FC curves showed an increase with decreasing the temperature and they separated at $T$= 175 K. The ZFC reached the maximum at $T$= 60K, while the FC increased countinuously at the same point [23,24]. The maximum value of the ZFC is known as the ‘blocking temperature’ ($T_B$), which refers to the broad size distribution. For this film, $T_B$ ~ 60 K. The presence of $T_B$ proves that YIG/YAG thin film is likely to contain nano-size grains, which agrees with the grain size calculation where *D*=29 nm for YIG/YAG thin film. The grain size calculated from XRD measurement using Sherrer equation (see §5.3.2).

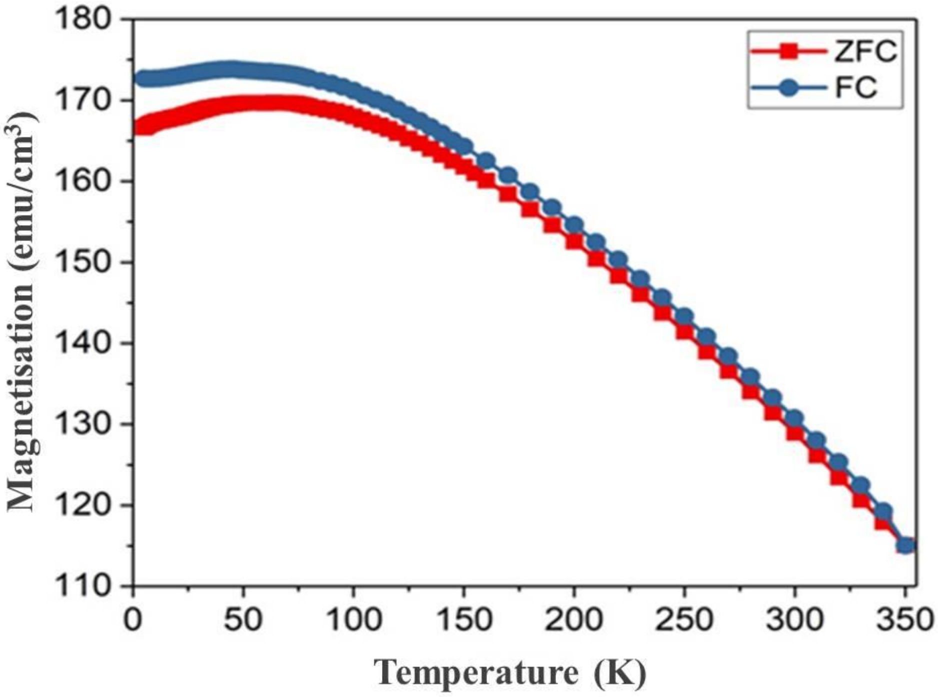

Figure 5.17: ZFC and FC magnetisation for YIG/YAG thin film taken with applied magnetic field of 100 Oe.

Table 5.3: the magnetic properties of the YIG films at 300 K:

| ***Substrate*** | $P_{O2}$ ***mTorr*** | ***Ms at 300K (emu/cm$^3$)*** | ***Hc at 300K (Oe)*** |
|---|---|---|---|
| GGG | 100 | 588 ±0.2 | 1.7 ±0.01 |
| GGG | 400 | 143 ±0.1 | 0.7 ±0.01 |
| GGG | 500 | 140 ±0.3 | 30.6 ±0.2 |
| YAG | 400 | 140 ±0.4 | 34.2 ±0.1 |

*YIG thin films*

The magnetic characterisation of YIG thin films agreed with the results obtained in crystal structure analysis. The results revealed that $M_s$ and $H_c$ of YIG/GGG thin film, which was grown with $P_{O2}$= 400 mTorr, were close to $M_s$ and $H_c$ of bulk YIG. In addition, $H_c$ of YIG/YAG film was higher than $H_c$ of bulk YIG with no negligible difference between their $M_s$ due to the high strain between YIG and YAG structure. However, the film of YIG/GGG, which was grown with $P_{O2}$ = 100 mTorr, showed higher $M_s$. This is because this film contains an amount of mettalic Fe. The film of YIG/GGG, which was grown with $P_{O2}$ = 500 mTorr, showed $M_s$ close to the bulk with high $H_c$. This could be due to presence of defects in this film as a result of the high oxygen pressure during ablation.

### *5.3.4 Magneto-optical properties:*

The MCD spectra presented in this section were taken in Faraday geometry as a function of energy change in range 1.5-4 eV. The technique measures the elipticity of the MCD in applied magnetic field of ±18,000 Oe out-of-plane. The signal from the substrate has been subtracted from all presented data. Figure 5.18 shows the change in MCD spectra as a function of energy for YIG thin film on GGG substrates, which were grown at different oxygen pressure 100, 400 and 500 mTorr. These MCD spectra were measured at room temperature and the results of the films showed three main features. Firstly; the peak at energy of 2.75 eV is a positive paramagnetic contrbution, which refers to the transition of $^6A_{1g}$ ($^6S$) – $^4T_{2g}$ ($^4D$) in the octahedral $Fe^{3+}$ ions [25, 26]. Secondly; at energy higher than 2.75 eV, the MCD spectra of YIG changed. The negative paramagnetic features at energies of 3.1 and 3.5 eV indicated a biexcitonic transition, which occured in an exchange-coupled $Fe^{3+}_{(octahedral)}$ –$(O^{2-})_n$ - $Fe^{3+}_{(tetrahedral)}$. Finally; the positive despersive line in energy of 1.5 eV suggests the transition of $^6A_{1g}$ ($^6S$) – $^4T_{1g}$ ($^4G$) [15, 27]. Figure 5.18 shows that the height of the peak increased with reducing the oxygen growth pressure. The highest peak observed was for the film grown at 100 mTorr. This effect could be related to the present of the Fe metalic ions in the film, which increases the magnetisation of the film. The peak at 3.1 eV showed a shif, which is attributed to the change in the lattice constant. Figure 5.19 shows that the energy, which is required to the transition, increased with increasing the lattice constant. The features of the film grown with $P_{O2}$= 400 mTorr are clearer and agreed with Scott *et al* (figure 5.9), which was attributed to the occurrence of small lattice-strain. However, the films grown with $P_{O2}$= 100 and 500 mTorr showed different behaviour in the energy above 3.4 eV due to their lattice strain. The results reported by Scott *et al* showed higher number of peaks compared to this study's results, which can be attributed to the difference in accuracy of the measurements. Scott *et al* reported an accuracy of about 0.0125 eV, whereas our measurement's accuracy was about 0.05 eV. Another difference is that the MCD intensity in the previously reported measurements was higher than current study by a factor of ~10. This could be due to the difference in lamp intensity or slit width, which is placed between the spectrometer and the thin film. The results of MCD spectra of this study agree with XRD (§5.3.2) and magnetic (§5.3.3) measurements presented earlier.

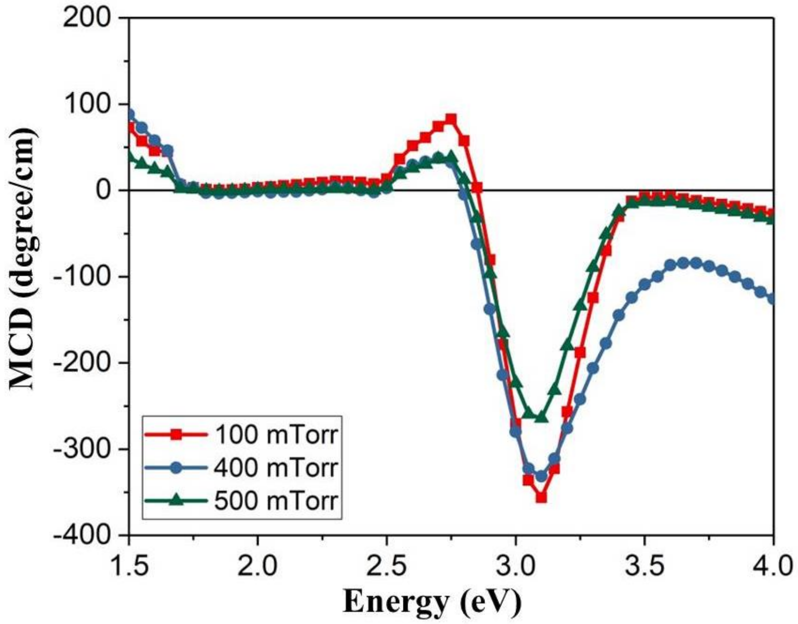

Figure 5.18: The MCD spectra at room temperature for YIG/GGG thin films grown at different oxygen pressure.

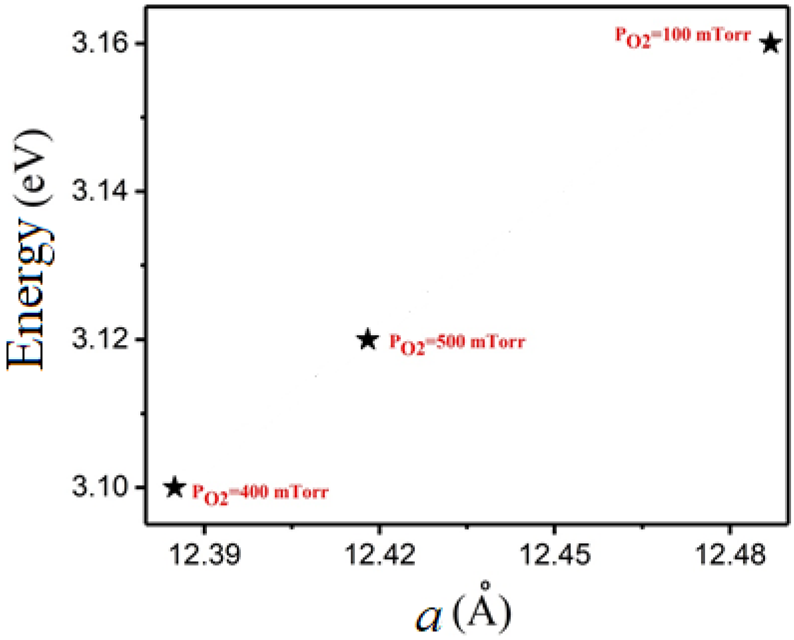

Figure 5.19: the shifting amount of energy 3.1 eV for MCD peaks of transition as a function of lattice constant for YIG/GGG thin films, which were grown with different oxygen pressure.

Figure 5.20 shows the MCD spectra of YIG thin films grown on GGG and YAG substrates at oxygen pressure 400 mTorr. These measurements were performed at room temperature with applied magnetic field of ±18000 Oe and energy range 1.5 - 4 eV. The YIG/YAG film has the same features of YIG/GGG film, which indicates the transition mentioned above. However, the features of YIG/YAG have a weaker signal than in YIG/GGG. In addition, the peak at 3.5 eV became a shoulder in the film grown on YAG. By comparing fig. 5.18 & 5.20, YIG/YAG thin film has same behaviour above 3.4 eV as YIG/GGG thin films, which were grown with $P_{O2}$= 100 and 500 mTorr. This behaviour is more likely to be due to the lattice-strain between YIG and YAG in the films resulted from their lattice mismatch. The strain of YIG/YAG appears to be the highest compared to other films (table 5.2), which means it will have a higher effect on this film.

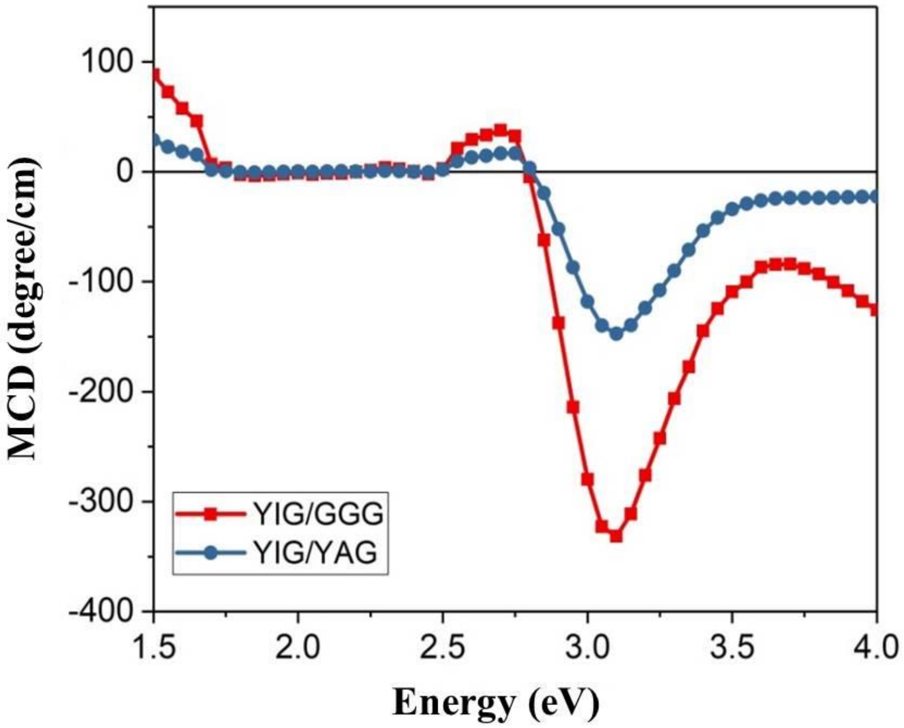

Figure 5.20: The MCD spectra at room temperature for YIG/GGG and YIG/YAG thin films grown at $P_{O2}$= 400 mTorr.

The MCD of YIG thin films was also compared to the MCD of a pure YIG crystal. The YIG crystal of a thickness 0.5 mm with area of 5×5mm is usually used as a calibration sample in magneto-optics measurements. The MCD measurement was performed at room temperature with applied magnetic field of ±18000 Oe. The MCD spectrum (fig. 5.21) demonstrated that the pure YIG have same features at energies 2.7 eV and 3.1 eV, which agrees with MCD spectra of YIG thin films. The rest of pure YIG features in table 5.1 were not observed in the current measurements. However, the MCD spectrum above the energy of 3.4 eV seems to be reduced by the absorption. The YIG crystal starts absorbing above 3.4 eV as shown by Scott *et al* [15].

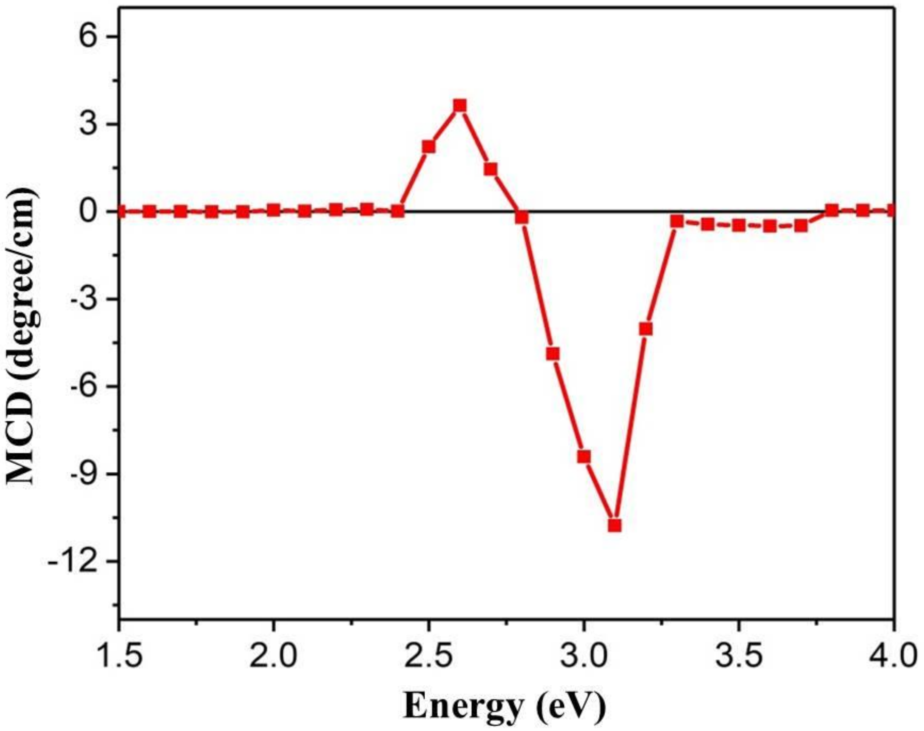

Figure 5.21: The MCD spectrum of pure YIG crystal at room temperature and with applied magnetic field of ±18000 Oe.

The MCD spectra as a function of temperature were measured for YIG/GGG and YIG/YAG thin films, which were grown at $P_{O2}$= 400 mTorr, in order to provide more details about the origin of the MCD signal and indicate if there is any defect phases. Each film was maintained inside cryostat and vacuumed before reducing the temperature to prevent any thermal contact between the film and the cryostat (see Chapter 3). The temperature was reduced by pumping helium gas inside the cryostat. The temperature dependence of MCD of the blank substrate and the glass window were measured and subtracted in order to obtain the spectra of thin films only. A magnetic field of ±5000 Oe was applied instead of 18000 Oe due to the increase of the distance between the magnetic poles to fit with the cryostat. The MCD spectra of YIG/GGG thin film, which were grown with $P_{O2}$ = 400 mTorr, was measured at room temperature (RT) and 10 K, as shown in fig. 5.22. The magnitude of the MCD features at 2.75 and 3.1 eV increased with decreasing the temperature from 42 to 88 degree/cm and -

202 to – 354 degree/cm, respectively. This strongly agrees with the increase in the magnetisation with decreasing the temperature (see §5.3.3). Having the same feature at same energy at different temperature indicates that the ferrimagnetism is original and have the same donor state. In addition, the film showed some oscillation in the energy range 1.7-2.5 eV at 10 K. The transition peak at 3.6 eV disappeared due to the high absorption in this region at low temperature and it became a shoulder.

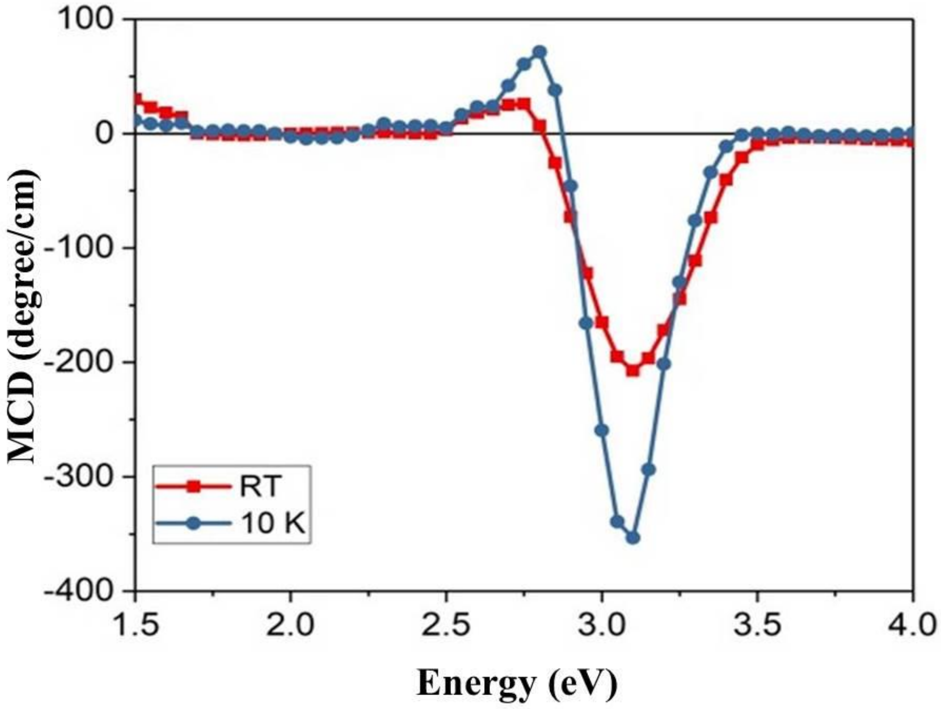

Figure 5.22: Temperature dependence of the MCD spectra measured with applied magnetic field of ±5000 Oe for YIG/GGG thin films. All substrates data are subtracted.

The MCD spectra for YIG/YAG thin film were also measured at room temperature and 10 K as shown in fig. 5.23. The feature of energy 2.75 and 3.1 eV in this film has the same behaviour of YIG/GGG films with a red-shift for transition peaks to 2.8 and 3.02 eV, respectively. These shifts results are due to the change in crystallographic structure of the film with temperature. The lattice parameter decreases with decreasing the temperature [15]. In addition, the transition peak of 3.1 eV at 10 K was thinner than at room temperature for both films due to the thermal depopulation for the vibrionic states in the pure electronic ground state [27, 28]. The magnitude of the peaks at 2.8 and 3.02 eV also increased from 18 to 60 degree/cm and from -50 to 152 degree/cm, respectively. That behaviour is expected due to increase the magnetisation of the film with decreasing the temperature.

The MCD measurements showed likely features of YIG and this confirmed the insights obtained from the crystal structure and magnetic properties in which YIG/GGG thin film was grown with $P_{O2}$ had magneto optical properties closest to bulk YIG. It was noticed that the measurement at room temperature using cryostat is lower and different from the normal MCD at room temperature. This is due to use of a lower magnetic field with the cryostat.

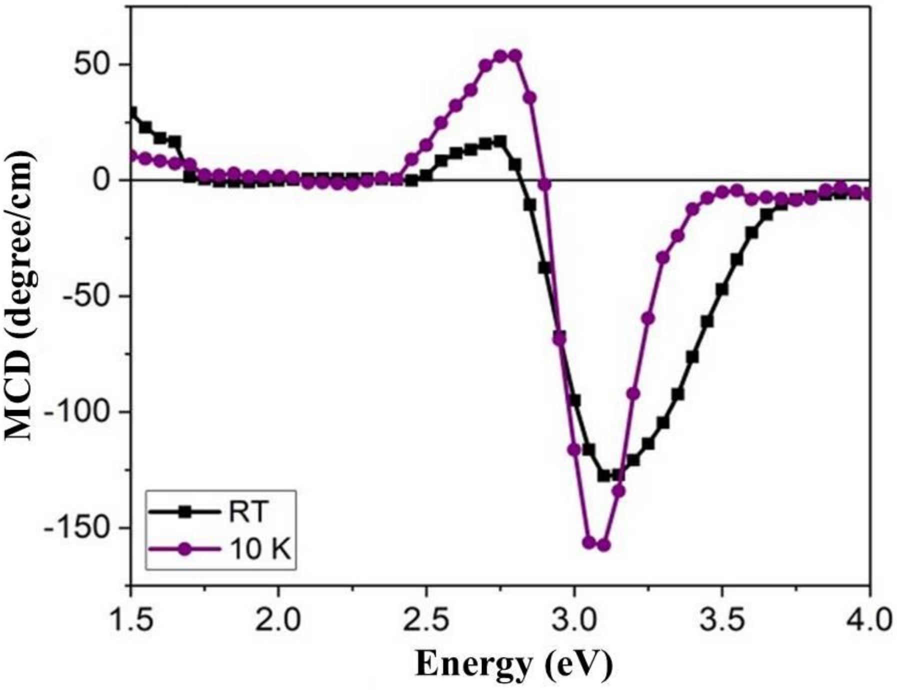

Figure 5.23: Temperature dependence of the MCD spectra measured with applied magnetic field of ±5000 Oe for YIG/YAG thin films. All substrates data are subtracted.

## 5.4 Summary:

YIG thin films were prepared on GGG and YAG substrates by PLD technique. The most suitable conditions to grow YIG thin film with properties close to the bulk YIG was by growing it with substrate temperature of 500 ˚C, $P_{O2}$= 400 mTorr and annealing the film after ablation at 1000 ˚C in air. The film grown on GGG substrate with these conditions has structure and magnetic properties close to bulk YIG with small strain of ε= 0.016%. $M_s$ of this film has the same $M_s$ of bulk YIG =143 emu/cm$^3$ with $H_c$ less than 1 Oe, which represents a successful achievement of the aims of this chapter (see §5.1).

The film grown on GGG substrate with less oxygen pressure ($P_{O2}$=100 mTorr) has very high $M_s$. When the XANES spectrum of this film was measured, it suggested the presence of about 6% iron metal ions $Fe^0$, which has a ferromagnetic properties with $M_s$ ~ 1700 emu/cm$^3$. The deposition of YIG film on YAG substrate with $P_{O2}$=400 mTorr showed magnetic properties close to the bulk YIG with higher $H_c$ that suggested to be due the high strain of the film. The strain in the crystal structure of this film ε=1.2 % is likely to be due to the crystallographic mismatch between the film and the substrate.

The magnetisation as a function of the change in temperature was studied and it showed an increase in the magnetisation with decreasing the temperature. This behaviour is characteristic of ferrimagnetic materials. This measurement was essential to ensure all antiferromagnetic α-$F_2O_3$ powder interacted with $Y_2O_3$ powder and formed the ferrimagnetic YIG target.

The MCD measurements showed two main transitions for all films in $^6A_{1g}$ ($^6S$) – $^4T_{2g}$ ($^4D$) in octahedral sites in about 2.75 eV and biexciton transition at 3.1 eV. The MCD spectrum of YIG/GGG thin film, which was grown with $P_{O2}$=400 mTorr, shown the same behaviour of bulk YIG with less feature that could be due to the smaller accuracy. However, the films of

YIG/GGG, which were grown with $P_{O2}$= 100 and 500 mTorr, and YIG/YAG thin films showed increase in the absorption at energy above 3.4 eV. This behaviour was attributed to the higher strain for these films. On the other hand, the MCD signals were found to increase with decreasing the temperature. The films were compared with the MCD spectrum of YIG crystal, which was measured using the same setup. The results of YIG crystal showed same features YIG films with high absorption above 3.4 eV. This comparison indicated the lower number of features appeared in YIG films of this work compared to the reported films in the literature. A possible explanation is the difference in the MCD setup used such as the lamp intensity and the slit width.

## 5.5 References:

1. Kumar, R., Hossain, Z. and R. C. Budhani. *Journal of Applied Physics* **121.11** (2017): 113901.
2. Wesenberg, D., *et al*. *Nature Physics* **13.10** (2017): 987.
3. Xue, F., *et al*. *Journal of Magnetism and Magnetic Materials* **446** (2018): 118-124.
4. Rajendran, M., *et al*. *Journal of Magnetism and Magnetic Materials* **301.1** (2006): 212-219.
5. Pardavi-Horvath, M., *et al*. *Journal of magnetism and magnetic materials* **119.1-2** (1993): 193-204.
6. Shone, M. *Circuits, systems, and signal processing* **4.1** (1985): 89-103.
7. Hu, Bolin. "*Crystal growth of hexaferrite architecture for magnetoelectrically tunable microwave semiconductor integrated devices.*" PhD thesis. Northeastern University Boston (2015).
8. Bhoi, B., *et al*. *IEEE Transactions on Magnetics* **49.3** (2013): 990-994.
9. Thavendrarajah, A. Dissertation. The Ohio State University, (1992).
10. Sanchez, R. D., *et al*. *Journal of magnetism and magnetic materials* **247.1** (2002): 92-98.

11. Kumar, N., *et al*. *Journal of Magnetism and Magnetic Materials* **320.18** (2008): 2233-2236.
12. Onbasli, M. C., *et al*. *APL Materials* **2.10** (2014): 106102.
13. Hansen, P., and J-P. Krumme. *Thin solid films* **114.1-2** (1984): 69-107.
14. Larsen, P. K., and R. Metselaar. *Journal of Solid State Chemistry* **12.3-4** (1975): 253-258.
15. Scott, G. B., *et al*. *Physical Review B* **12.7** (1975): 2562.
16. Wood, D. L., and J. P. Remeika. *Journal of Applied Physics* **38.3** (1967): 1038-1045.
17. Zaki, A. M., *et al*. *Journal of Magnetism and Magnetic Materials* **453** (2017).
18. Zhang, Y., et al. *IEEE Transactions on Magnetics* **51.11** (2015): 1-4.
19. Yin, H., and G. M. Chow. *Journal of materials research* **8.1** (2003): 180-187.
20. Maier-Flaig, H., *et al*. *Physical Review B* **95.21** (2017): 214423.
21. Graham Jr, C. D. *Physical Review* 112.4 (1958): 1117.
22. Lage, Enno, et al. *APL Materials* **5.3** (2017): 036104..
23. Suchomski, C., *et al*. *Chemistry of Materials* **25.12** (2013): 2527-2537.
24. Sanchez, R. D., *et al*. *Physica B: Condensed Matter* **354.1-4** (2004): 104-107.
25. Nguyet, *et al*. *Journal of Alloys and Compounds* **541** (2012): 18-22.
26. Wettling, W. *Journal of Magnetism and Magnetic Materials* **3.1-2** (1976): 147-160.
27. Lage, E., *et al*. *APL Materials* **5.3** (2017): 036104.
28. Kumar, N., *et al*. *Journal of Magnetism and Magnetic Materials* **272** (2004): E899-E900.
29. Dorsey, P. C., *et al*. *Journal of Applied Physics* **74.2** (1993): 1242-1246.

# 6. Ca doped YIG thin films

## 6.1 Introduction:

YIG thin films were fabricated on GGG and YAG substrates. It was found that the films grown in an oxygen pressure of 400 mTorr have properties close to bulk YIG. YIG is a promising material for spintronic applications if it is successfully doped to exhibit the properties of magnetic diluted semiconductors. In this chapter, the possibility of growing Ca:YIG thin films by PLD is investigated. This includes studying the effect of Ca-doping on the structural, magnetic and magneto-optical properties of Ca:YIG thin films. A brief review on previous work concerning dope YIG thin films with Ca and other ions will be presented and followed by the main experimental results of the current study.

## 6.2. Previous work:

### *6.2.1 Dopant ions and charge compensation of yttrium iron garnet:*

YIG is a ferrimagnetic insulating material (see §5.2) that has several different sites that enables its doping by a wide range of ions. These ions may have different valence and radius from the ion they replace. YIG films have been doped by diamagnetic ions that substitute on one or more of the three sites in YIG: $\{Y^{3+}\}$, $[Fe^{3+}]$ and $(Fe^{3+})$ [1]. The diamagnetic ions discussed here are Ca, Bi, In, V or Ga [1].

Pure YIG has two magnetic sublattices due to the magnetisation of the tetrahedral $Fe^{3+}$ sites ($M_d$) and the magnetisation in the octahedral $Fe^{3+}$ sites ($M_a$) (see §5.2). The difference between these two magnetisations determines the ferrimagnetism of YIG. When YIG is doped with diamagnetic trivalent ions ($M^{3+}$) in the tetrahedral sites sublattices (such as $Ga^{3+}$ doped YIG ($Y_3Fe_{5-x}Ga_xO_{12}$)); the charge balance will not change. However, the saturation magnetisation ($M_s$) of YIG drops from 143 emu/cm$^3$ to zero emu/cm$^3$ at low temperature for x=1.14 [2].

YIG can be doped with diamagnetic ions of divalent cations ($M^{2+}$) or tetravalent cations ($M^{4+}$) such as: $Ca^{2+}$, $Mg^{2+}$, $Pb^{2+}$, $Si^{4+}$ and $Ge^{4+}$ [2, 3]. These ions substitute on different sites in a YIG crystal. For example, $Si^{4+}$ or $Ge^{4+}$ ions substitute on the $Fe^{3+}$ tetrahedral sites and generate $Fe^{2+}$ ions on a neighbouring octahedral site. $Bi^{4+}$ ions substitute the $Y^{3+}$ dodecahedral sites and generate $Fe^{2+}$ on the tetrahedral sites. $Ca^{2+}$ ions also substitute the dodecahedral sites but form $Fe^{4+}$ ions on the tetrahedral sites [4]. When the divalent or tetravalent ions are substituted in YIG, the resulting composite YIG will be changed due to the valance change of +1 or -1. However, doping with a trivalent ion will not generate extra charges [5].

The inclusion of divalent and tetravalent ions in YIG thin films leads to charge-compensating substitution, which reduces $M_s$ of YIG. This reduction results from the formation of $Fe^{4+}$ and $Fe^{2+}$ ions, which ensure that the overall charge is neutral [1]. If these ions are present in YIG; the magnetic, electrical and optical properties of YIG will change [1]. The presentation of divalent and tetravalent cations also affects the electric properties and produces either p-type or n-type defect states, respectively [6]. The electrical conductivity in this case is assumed to occur by hopping due to the presentation of two different iron valences, which leads to a drop in the resistivity to lower than $10^4$ Ωcm [7].

In pure YIG, $Fe^{3+}$ ions have $S$=5/2 and $L$=0 [1, 3]. However, the $Fe^{4+}$ and $Fe^{2+}$ ions are non $S$-state ions with $S$=2 and $L$=2 in $t_g$ degenerate states. The single ion anisotropy of these ions is high and they also have a large spin-orbit interaction. The $Fe^{4+}$ ($3d^4$) ion has a plot of energy in tetrahedral sites similar to $Fe^{2+}$ ($3d^6$) in the octahedral sites, as shown in fig. 6.1.

This similarity is in a cubic crystalline field split, exchange field, split-orbit coupling and coulomb field of ions [4].

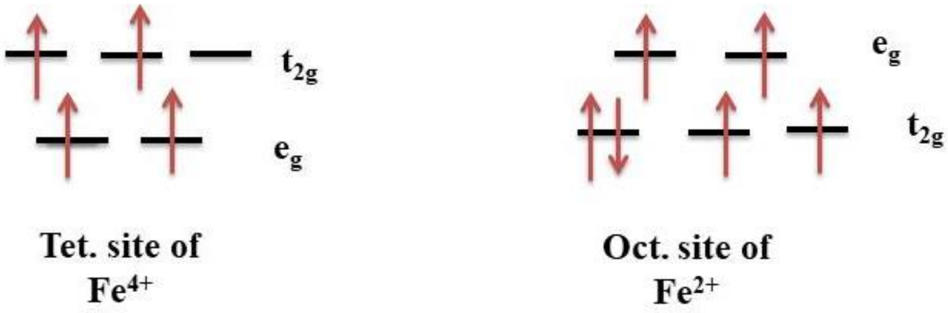

Figure 6.1: The energy state diagram illustrates the electrons contribution of $Fe^{4+}$ ion in the tetrahedral sites with $Fe^{2+}$ ion in the octahedral sites.

### *6.2.2 $Ca^{2+}$ doped YIG:*

YIG doped with Ca provides a hole-compensating doping, which is likely to produce a semiconductor with magnetic properties similar to permanent magnetic materials and with a possibility of controlling the number of carriers [8]. If the result of substituting $Ca^{2+}$ on dodecahedral sites is to produce holes on oxygen ions; there should be no change in magnetisation. However, the magnetisation was observed to drop to about 20% for Ca:YIG thin film with concentration of x=0.14, which was attributed to the generation of $Fe^{4+}$ ions [4, 8]. Each $Ca^{2+}$ ion either produces $Fe^{4+}$ ion on the tetrahedral sites or reduces the average value of the oxygen content [9]. Theoretical models assumed that about 1/3 of magnetic ions on the tetrahedral sites of YIG formed into $Fe^{4+}$ ions for $x$=0.14, which coupled ferromagnetically with the $Fe^{3+}$ ions of the octahedral sites [1,3]. Accordingly, the holes that are introduced by substituting $Ca^{2+}$ become delocalized at high temperature. However, they are localized at tetrahedral sites and form $Fe^{4+}$ ions at low temperature [1]. Ca doped YIG thin films became a promising material for their use as an alternative dilute magnetic semiconductor [10]. These films have activation energy in the range 0.2-0.4 eV and their resistivity could be as low as 300 Ωcm at room temperature [9].

To understand the structure of $Ca^{2+}$ doped YIG compared to pure YIG, the target (which is made from $Y_2O_3$ and $Fe_2O_3$ only) has more oxygen than the target that includes CaO. This can be described by the formula [11]:

$$\{Y^{3+}\}_{3-x}\,\{Ca^{2+}\}_x\,[Fe^{3+}]_2\,(Fe^{3+})_3\,O_{12-\frac{x}{2}}\,V_{O\frac{x}{2}}^{\cdot\cdot} \tag{6.1}$$

$V_O^{\cdot\cdot}$ is the oxygen vacancy and $x$ is the concentration. Hence, keeping $Fe^{3+}$ ions and $O^{2-}$ could be provided if there are more oxygen vacancies, which are about $x/2$. If not, this will produce a charge compensation, which is achieved by including $Fe^{4+}$ ions in the tetrahedral sites or $O^{1-}$ in the oxygen sites [11]. This all depends on the oxygen content during the growth.

As for the magnetic properties, Pardavi-Horvath *et al* found that the magnetisation is reduced by 20% when Ca doped in YIG with $x= 0.14$ at low temperature, while the easy direction of YIG does not change when it is doped by $Ca^{2+}$ even at low temperature (~ 4.2K) [4]. The low magnetisation of Ca:YIG thin films showed an exceptional behaviour at low temperature. When the magnetisation reaches a maximum value below 100 K; it starts dropping with decreasing the temperature down to 0 K (fig. 6.2). However, the magnetisation of pure YIG showed an increase with decreasing the temperature to 0 K (as discussed in §5.3.3). This reduction in the magnetisation is due to the presence of localized ferromagnetic superexchange instead of the usual antiferromagnetic exchange between the tetrahedral *d*-sites and the octahedral *a*-sites.

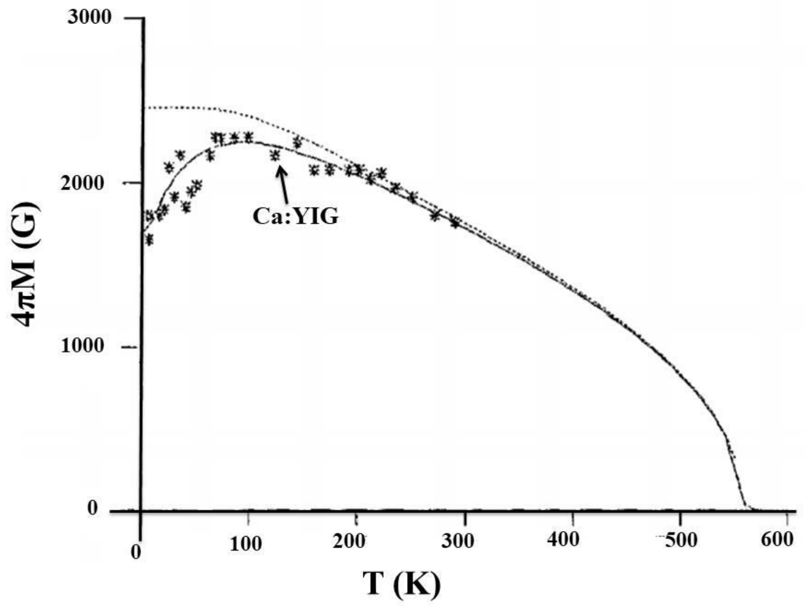

Figure 6.2: Temperature dependence of the magnetisation for Ca:YIG thin film with $x$=0.34 [2]. Reprinted with permission of Journal of Applied Physics.

This abnormal behaviour is explained by molecular field theory model [5]. In magnetic materials, the energy of spin $S_i$ could be found with the Heisenberg Hamiltonian;

$$< H_i >= -2\sum_j J_{ij} S_i . S_j - g\mu_B < S_i > . H \tag{6.2}$$

where $S_i$, $S_j$ are the spins, $i$ and $j$ are the sites, $J_{ij}$ is exchange integrals, $H$ is the external field and $H_i$ is the molecular field and it can be calculated through:

$$< H_i >= \frac{2}{g\mu_B}\sum_{j,i} J_{ij} < S_i > \tag{6.3}$$

For a YIG system, which has two magnetic sites ($d$ and $a$), and in the absence of external magnetic field ($H$=0), the molecular field is:

$$\langle H_{dz} \rangle = \frac{2}{g\mu_B}(J_{dd} n_{aa} \langle S_{dz} \rangle + J_{ad} n_{da} \langle S_{az} \rangle) \tag{6.4}$$

$$\langle H_{az} \rangle = \frac{2}{g\mu_B}(J_{ad} n_{ad} \langle S_{dz} \rangle + J_{aa} n_{aa} \langle S_{az} \rangle) \tag{6.5}$$

where $n_{ad}$ is the number of nearest neighbours of a-site spin to the d-site spin. For YIG; $n_{dd}$ =4, $n_{aa}$=8, $n_{da}$=4, $n_{ad}$=6 and the spin is $S$=5/2 [2]. The exchange integrals of YIG are $J_{ad}$=-36.4 K, $J_{dd}$=-17.1 K and $J_{aa}$=-12.2 K. When $Ca^{2+}$ ions substitute $Y^{3+}$ ions in YIG, the exchange integral and the lattice constant will change. If the spin will give a different value of $n_{ij}$, which is the number of nearest neighbours of *i*-site to *j*-site spin. The lattice in this case may have some defects, such as: oxygen vacancies or other ions. The oxygen vacancies can break or remove the interaction between one *a-d* sites and affect $J_{ad}$. A ferromagnetic superexchange could occur between the tetrahedral *d*-site and octahedral *a*-site at a point of local disorder [5]. Then, the molecular field at *d*-site or *a*-site in this case will be:

$$\langle H_i \rangle = \frac{2}{g\mu_B} \sum_K n_{iK} J_{iK} \langle S_K \rangle \tag{6.6}$$

where $S_K$ is average spin. The magnetic moment per mole can be determined using Brillion function:

$$M_{tot} = N_A g \mu_B \sum_i f_i \langle S_i\ (T) \rangle \tag{6.7}$$

where, $f_i$ is the fraction of $Fe^{3+}$ ions at d-sites or a-sites and $N_A$ is Avogadro's number. By assuming that Fe ions at *d*-sites have one ferromagnetic super exchange (*a-d* link), so:

$$\langle H_{dI} \rangle = \frac{2}{g\mu_B} \{(4J_{dd} + \Delta J_{dd}) S_{d\,Av} + (3J_{ad} + J_I) S_{a\,Av}\} \tag{6.8}$$

where $J_I$ is the exchange integral of the ferromagnetic exchange via the oxygen vacancies (*Vo), $\Delta J_{dd}$* is the possible change in *d-d* interaction as a result of the increase in the number of oxygen ions. $S_{dAv}$ and $S_{aAv}$ are the average of *d*-site spin and *a*-site spin, respectively. The $Fe^{3+}$ ion at a given site may reverse at low temperature. This depends on the strength of $J_I$. The orientation of the spin *($S_{dI}$)* will reverse at 0 K, if $J_I$> 40.8K with ignoring $\Delta J_{dd}$. The *a*-site has six antiferromagnetic superexchange *a-d* sites, therefore; it will be hard to reverse them by replacing one of *a*-*d* linked with ferromagnetic one. Hence, the abnormal magnetic behaviour of Ca:YIG at low temperature is expected to result from the reversal of *d*-sites spins [5].

Paradavi *et al* also studied behaviour of the magnetisation of Ca:YIG thin films at low temperature. They assumed that when the $Ca^{2+}$ ions substitute YIG, the holes will be present [2]. These holes are delocalized at high temperature. Therefore, the magnetisation behaves similar to pure YIG. However, when the temperature decreases down to 0 K, the holes in the tetrahedral sites will gradually localize and $Fe^{4+}$ ions will be produced. This localization is temperature dependent according to [2]:

$$[Fe^{4+}]_T = [Fe^{4+}]_o[1 - exp(-T_o/T)] \tag{6.9}$$

where $[Fe^{4+}]_T$ is the concentration of $Fe^{4+}$ ions at $T$ temperature and $[Fe^{4+}]_o$ is the concentration of $Fe^{4+}$ ions at $T_o$ temperature. The anomalies temperature, which is the temperature that marks the magnetisation decrease, is dependent on the amount of $Ca^{2+}$ ions. For example, the magnetisation of Ca:YIG/GGG thin films with $x$=0.34 increased with increasing the temperature up to $T$=200 K. Then, the magnetisation decreased with decreasing the temperature down to 0 K [2].

Szweykowska *et al* also studied the effect of the temperature drop on the magnetisation of Ca:YIG thin films. The $Ca^{2+}$ concentration in their study was $x$=0.15. The magnetisation started dropping at a temperature less than 100 K, as shown in fig. 6.3. They suggested that this behaviour is due to the temperature dependence of the exchange interaction between Fe ions in *d*-sites and *a*-sites [12].

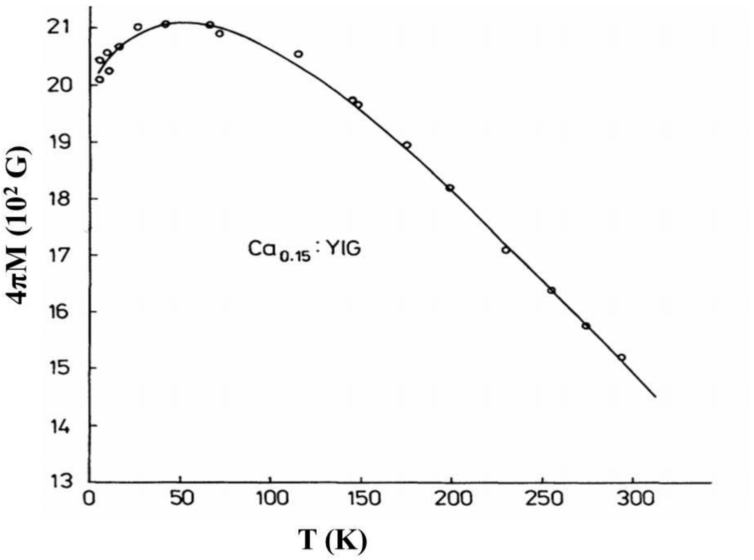

Figure 6.3: Temperature dependence of the magnetisation for Ca:YIG thin film with $x$=0.15 [12]. Reprinted with permission of Physical Review B.

For YIG optical properties, the absorption of YIG will be strongly increased in the near infra-red if $Ca^{2+}$ ions substitute YIG ions even with small amounts of Ca. This is because of the change of $Fe^{3+}$ ions in the tetrahedral sites into $Fe^{4+}$ ions [9]. The increase in absorption of Ca:YIG films is because $Fe^{4+}$ ions are effectively moved in the lattice by holes. This increase in absorption makes it interesting for many applications, such as; p-type electric conductance and photoinduced effects [9]. Bornfreund *et al* studied the optical properties of Ca:YIG thin films grown by liquid phase epitaxial (LPE) technique with concentration of Ca ($x$=0.18). They found that the films had two features in the absorption curve at λ= 607 nm (~2 eV) and λ=910 nm (~1.4 eV), as shown in fig. 6.4. These features were similar to the pure YIG thin film (see §5.2), which were reported by Scott *et al* on table 5.1 and agreed with the magneto optical results of YIG films (§5.3.4). The feature at 2eV indicated that there was a crystal transition in $^6A_1(^6S) \rightarrow {}^4T_1(^4G)$. This transition occurred in the tetrahedral sites. However, the feature at 1.4 eV is related to the crystal transition of $^6A_{1g}(^6S) \rightarrow {}^4T_{1g}(^4G)$, which occurred in the octahedral sites [10].

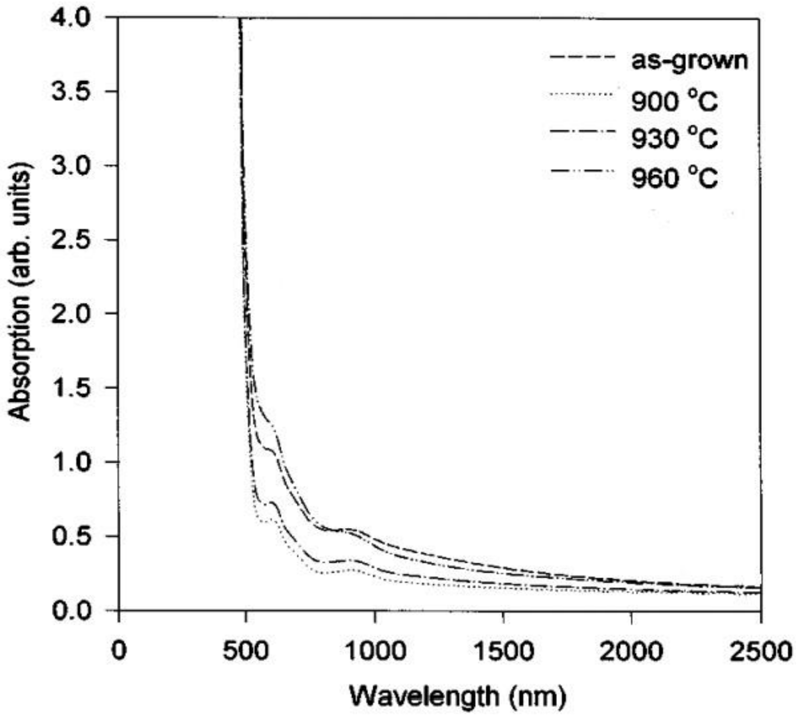

Figure 6.4: The optical absorption of Ca:YIG thin film with different annealing temperature (500nm ~ 2.5 eV) [9]. Reprinted with permission of Journal of Applied Physics.

MCD is a valuable tool to study the properties of the compensating centres of Ca:YIG [13]. It also measures the properties of $Fe^{4+}$ ions and it can be used to determine the two distinct types of $Fe^{4+}$ centres [9]. Kucera *et al* found through MCD that there are two different type of centres in Ca:YIG thin film, which can be obtained from the magneto optical spectra [13]. These types are: type I, which represents the absorption band of the MCD spectrum with peaks near 0.78 and 1.39 eV. The second type is type II, which provides bands of different shapes with peaks near 1.2 and 1.6 eV [13]

Kucera *et al* studied the MCD spectra of Ca:YIG thin films at different Ca concentrations. They found that Ca substituted YIG provided broad spectral bands in the near IR region of the magneto optical spectra (in both Faraday rotation and MCD spectra) [14]. The reduction of temperature from room temperature to 80 K increased the band intensity [14]. The effect of Ca concentrations on the MCD spectra was also studied, as shown in fig. 6.5. For the film with $x$>0.1, the intensity of the band was found to be increased with increasing the concentration in both Faraday rotation and MCD spectra. However, for $x\leq 0.1$; there were no bands in the magneto optical spectra [14].

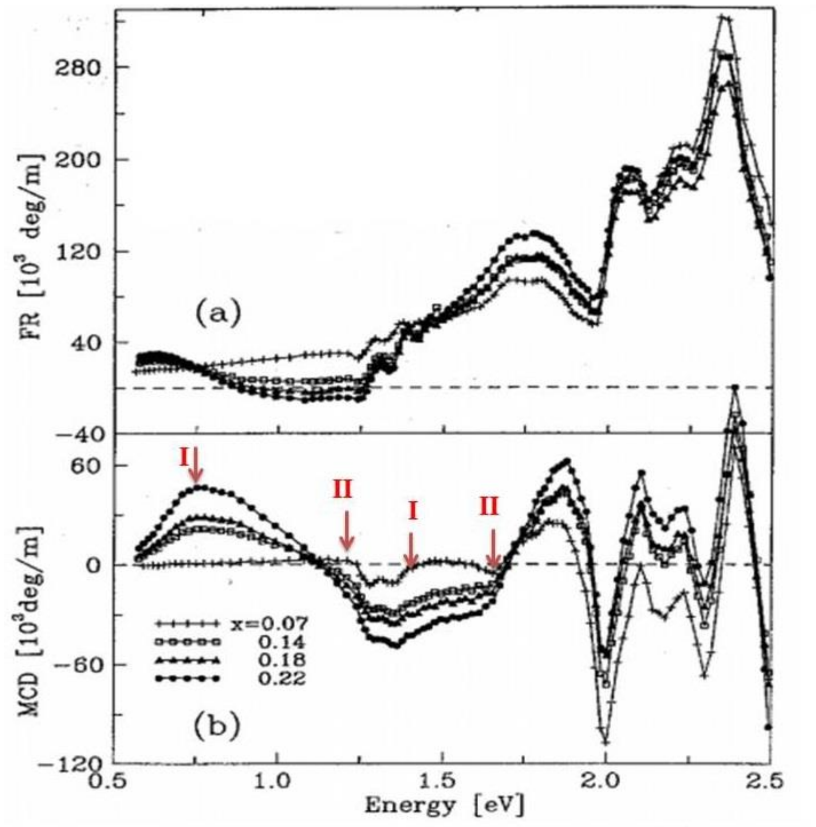

Figure 6.5: (a) The Faraday spectra and (b) the MCD spectra of Ca doped YIG with different concentration of $Ca^{2+}$ at 80 K. The figure illustrates the two types of centres in Ca:YIG (type I and II). The other peaks are related to the transitions in YIG [14]. Reprinted with permission of Journal of Magnetism and Magnetic Materials.

When YIG is doped with ions that have valence different from 3+, they will create a donor or accepter levels in the gap and increase the room temperature conductivity from$10^{-12}$ $\Omega^{-1}$cm$^{-1}$. D'Amico *et al* studied the change in resistivity of YIG when it is doped by Ca. They grew Ca:YIG thin films on GGG substrates with Ca concentration ($x$=0.36) by using LPE technique. The resistivity was found to drop from a value of $\rho$= $10^{12}$ Ωcm to $\rho$=450 Ωcm. They also found that the film had two special features; when the conductivity is measured in the presence of magnetic field-gradient, there was a large increase in conductivity. In addition, the film was used as a bolometer that gave higher response to the radiant energy [6, 15].

## 6.3 Present work:

### 6.3.1 Sample preparation:

The Ca:YIG targets used in this study were prepared from $Y_2O_3$, α-$Fe_2O_3$ and CaO powders. All powders were purchased from Alfa Aesar with a purity of 99.99%. Four different targets were made for different Ca concentrations, $x$=0.05, 0.1, 0.2 and 0.3. The weight of each powder needed to produce Ca:YIG targets was calculated through:

$$(3-x)Y_2O_3 + 5Fe_2O_3 + 2xCaO \rightarrow 2Y_{(3-x)}Ca_xFe_5O_{12}$$

So,

1 gm $Y_2O_3$ requires $\frac{5}{(3-x)}\frac{At.Wt_{Fe2O3}}{At.Wt._{Y2O3}}\, gm\ of\ Fe_2O_3$ and $\frac{2x}{3-x}\frac{At.Wt_{CaO}}{At.Wt_{/y2O3}}\ gm\ of\ CaO.$

The powders were mixed in stoichiometric amounts by pestle and mortar for 20 minutes. The mixture was sintered in an air furnace at 1000 °C for 10 hours. Then, the mixture was mixed again for 20 minutes and sintered at the furnace at 1000 °C for 10 hours. This step was repeated twice to ensure that all the powder particles interacted with each other. The next step was to compress the powder in vacuum (more details were given in §3.2). The targets were sintered in an air furnace at 1000 °C for 15 hours. Prior to the fabrication of these targets, a target was made by same method but was annealed at temperature of 1200 °C, which was used previously with YIG target (see Chapter 5). The target colour turned from light red to black and hence it was excluded from the study. This change of colour could be due to the loss of the Ca leading to a target dominated by FeO or $Fe_3O_4$, which both are black, as mentioned in Chapter 5. The other reasons could be due to loss some O ions from CaO and turning to Ca ions. These ions have a low melting point ~850 °C.

The films were deposited by PLD on 4×4×0.5 mm GGG or YAG substrates. The substrate temperature was fixed at 500 °C for all the films and the oxygen pressure inside the chamber was increased from 0.03 to 400 mTorr. After ablation, the films were annealed in an air furnace at 1000 °C for 4 hours.

### *6.3.2 Structural properties:*

The thickness measurements of the Ca:YIG films were performed using the Dektak technique. Figure 6.6 shows the XRD spectra of Ca:YIG/GGG thin films with different $Ca^{2+}$ concentrations. All the films exhibited an epitaxial structure represented by two peaks of orientation (400) and (800). Epitaxial structure means a single crystal layer of the film grown on the top of single crystal substrate. Comparing with pure YIG/GGG (fig. 5.11b), a shift in the peaks is observed when the YIG is doped with $Ca^{2+}$. Pure YIG/GGG (400) thin film has a peak at 2θ= 28.8˚, whereas the Ca:YIG/GGG (400) thin films with x=0.05, 0.1, 0.2 and 0.3 have peaks at 2θ=28.4°, 28.28°, 28.25° and 28.21°, respectively, as shown in table 6.1. However, pure YIG/GGG (800) thin film has a peak at 2θ= 59.6˚, whereas the Ca:YIG/GGG (800) thin films with $x$=0.05 and 0.1 have peaks at 2θ=58.1° and 58.4°, respectively. These shifts indicate a change in the lattice constants of the YIG phase with increasing the $Ca^{2+}$ concentration. The change in the lattice constant of the YIG phase due to change in the strain, which shows an increase with increasing $Ca^{2+}$ concentration (table 6.1). This behaviour was observed before by Al-Omari *et al* [16]. The increase in the lattice constant is likely to be resulted from the large radius of $Ca^{2+}$ (1.94 Å), which is larger than the substituted $Y^{3+}$ (0.9 Å). These results agree with the observations of Chen *et al* [17].

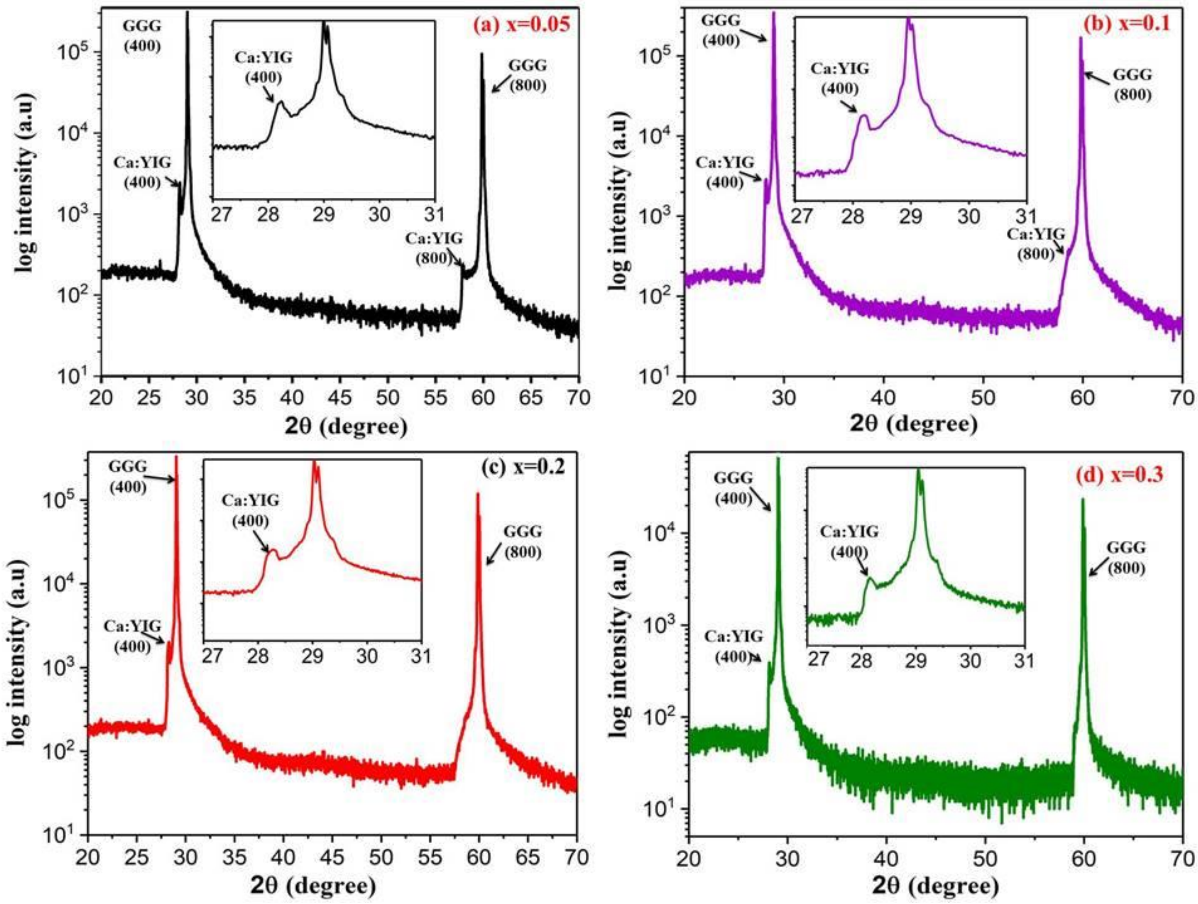

Figure 6.6: The XRD patterns of Ca:YIG/GGG thin films with different $Ca^{2+}$ concentrations (a) *x*=0.05, (b) *x*=0.1, (c) *x*=0.2 and (d) *x*=0.3.

Table 6.1: The structure properties obtained from XRD spectra for Ca:YIG (400) thin films on GGG substrates.

| Film NO. | x | t (nm) | 2θ (°) | a (Å) | Lattice mismatch (%) | ε (%) |
|---|---|---|---|---|---|---|
| YIG/GGG | 0 | 120 ±2 | 28.80 ± 0.02 | 12.385 ±0.001 | 0.016 | 0.070 ±0.0003 |
| Ca:YIG/GGG | 0.05 | 150 ±3 | 28.40 ± 0.04 | 12.550 ±0.005 | 1.351 ±0.002 | 1.406 ±0.0001 |
| Ca:YIG/GGG | 0.1 | 150 ± 3 | 28.28 ±0.003 | 12.613 ±0.0003 | 1.833±0.003 | 1.915 ±0.0001 |
| Ca:YIG/GGG | 0.2 | 150 ± 3 | 28.25 ± 0.002 | 12.621 ±0.0001 | 1.924 ±0.001 | 1.990 ±0.0003 |
| Ca:YIG/GGG | 0.3 | 150 ±3 | 28.21 ± 0.001 | 12.634± 0.0004 | 2.032 ±0.004 | 2.085 ±0.0002 |

*Ca doped YIG thin films*

The XRD spectra of Ca:YIG/YAG thin films, which have different $Ca^{2+}$ concentrations, were compared to the spectrum of pure YIG/YAG film (see §5.3.2). The Ca:YIG/YAG thin films also have an epitaxial structure with two peaks of orientation (400) and (800). The peaks of pure YIG/YAG are at 2θ of 30.0° and 62.0°, respectively. These peaks show a shift in the doped YIG that decreases with increasing the $Ca^{2+}$ concentration. The peak of orientation (400) shift to 30.1˚, 30.16˚ and 30.2˚ for $x$=0.1, 0.2 and 0.3, respectively. However, the peak of orientation (800) shift to 61.6˚, 60.5˚ and 60.3˚ for $x$=0.1, 0.2 and 0.3, respectively. This also indicates a change in the lattice constant (6.2). The increase in the lattice constant of Ca:YIG/YAG thin films is due to the mismatch between the YAG substrate and YIG thin film resulted from the doping of $Ca^{2+}$.

The average thickness of these films was 150±5 nm (table 6.1 and 6.2). The lattice mismatch in these films (shown in table 6.1), which was calculated by using equation 5.2 (§5.3.2), was raised from 0.016% for pure YIG/GGG thin films to 2.033% when $Ca^{2+}$ of $x$=0.3 substituted $Y^{3+}$ in YIG thin film on GGG substrate, which was grown in same conditions of pure YIG film. That increased the lattice strain $\varepsilon$ (table 6.1), which was calculated by using equation 5.3 (§5.3.2), from 0.07% for pure YIG to 2.085% for Ca:YIG thin film with $x$=0.3. This significant increase in lattice strain is due to substitution of small size $Y^{3+}$ by relatively larger ion $Ca^{2+}$, which disturbed the crystal lattice. The Ca:YIG/YAG thin films also showed an increase in the lattice mismatch from 1.65% for pure YIG/YAG thin films to 2.165% for the film of $Ca^{2+}$ concentration $x$=0.1 (table 6.2). Then, it increased up to 2.289% for the film of $Ca^{2+}$ concentration $x$=0.3. In addition, the lattice strain increased from 3.846% for pure YIG/YAG up to 4.468 % for Ca:YIG/YAG with $x$=0.3. These strain amounts are larger than the lattice strain of Ca:YIG/GGG thin films with same concentrations. This indicates a larger mismatch in the films grown on YAG substrates.

The grain size of the Ca:YIG/YAG phase was calculated manually by using Scherrer's equation and origin program for measuring FWHM for the peaks. It showed a slight decrease with increasing the $Ca^{2+}$ concentrations (table 6.2). The grain size for Ca:YIG/YAG thin films, such as 29, 29, 28 and 28 nm for $x$=0, 0.1, 0.2 and 0.3, respectively. The grain size of Ca:YIG/GGG thin films could not be deduced because of the overlapping of the peaks with those of GGG substrate.

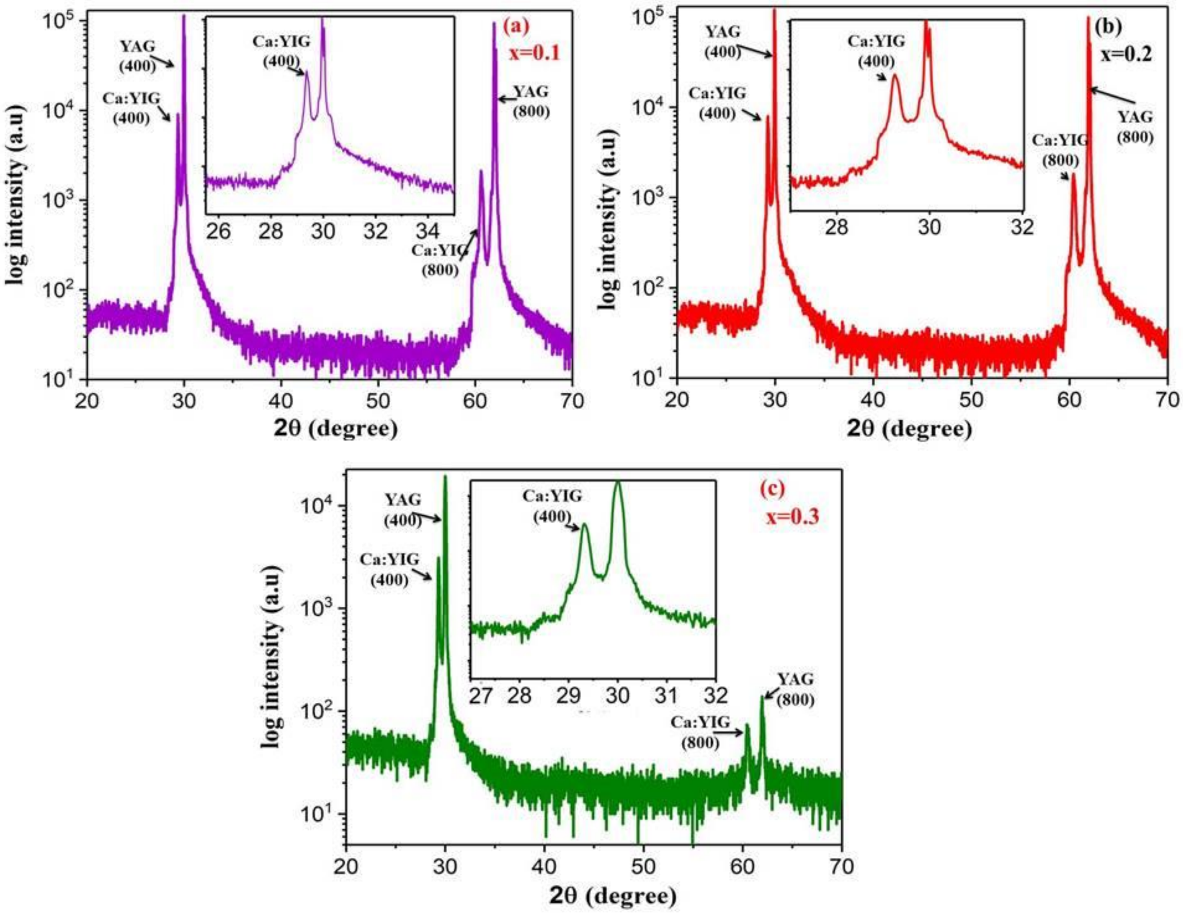

Figure 6.7: The XRD patterns of Ca:YIG/YAG thin films with different $Ca^{2+}$ concentrations (a) $x$=0.1, (b) $x$=0.2 and (c) $x$=0.3.

### *Ca doped YIG thin films*

Table 6.2: The structure properties obtained from XRD spectra for Ca:YIG (400) thin films on YAG substrates.

| **Film NO.** | **x** | **Thickness (nm)** | **2θ (°)** | **a (Å)** | **D (nm)** | **Lattice mismatch (%)** | **ε (%)** |
|---|---|---|---|---|---|---|---|
| YIG/YAG | 0 | 120 ±2 | 30.0 ±0.003 | 11.900 ±0.0004 | 29 ±0.4 | 1.650±0.0004 | 3.846 ±0.0001 |
| Ca:YIG/YAG | 0.1 | 150 ±3 | 30.1 ±0.002 | 11.86 ±0.0002 | 29 ± 0.5 | 1.983 ±0.0006 | 4.161 ±0.0002 |
| Ca:YIG/YAG | 0.2 | 150 ±3 | 30.16 ±0.002 | 11.838 ±0.0002 | 28 ±0.4 | 2.165 ± 0.0002 | 4.347 ±0.0001 |
| Ca:YIG/YAG | 0.3 | 150±2 | 30.2 ±0.003 | 11.823 ±0.0004 | 28 ± 0.2 | 2.289 ± 0.0002 | 4.468 ±0.0003 |

K-edge XANES and EXAFS spectra were recorded for further crystallographic investigation of Ca:YIG thin films. Figure 6.8 shows XANES spectra for Ca:YIG thin film on GGG substrate with $x$= 0.05, 0.1, 0.2, 0.3. These spectra were compared to XANES spectra of YIG powder and it indicated that the majority of the films have YIG phase with small shift to a lower valence at the edge of all doping levels. This shift suggests that the films contain about 5% of $Fe^{2+}$, which is independent of the doping levels. These spectra are important because they can give the ionization of the iron ($Fe^{n+}$), where n is valence number.

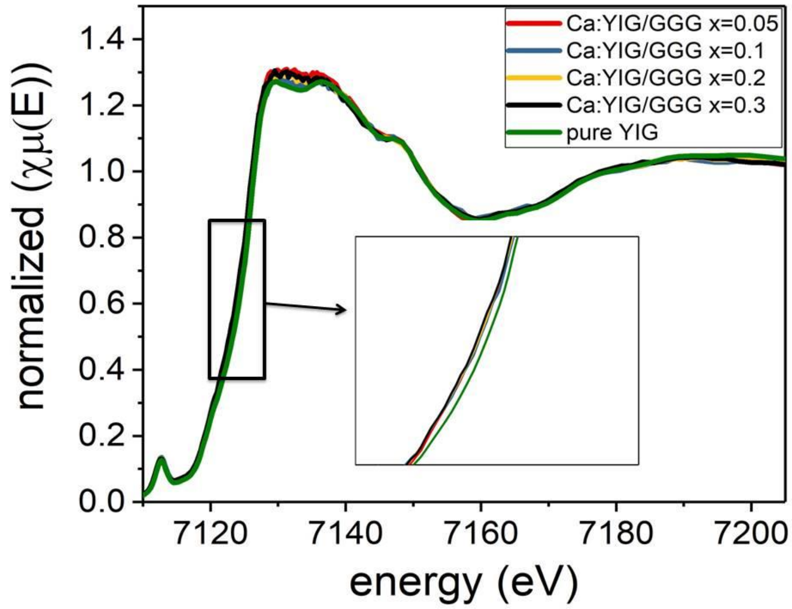

Figure 6.8: XANES spectra for $Fe^{3+}$ ions in Ca: YIG/GGG thin films with different Ca concentration $x$= 0.05, 0.1, 0.2 and 0.3 compared to pure YIG.

Figure 6.9 shows the distribution of ions around Ca in Ca:YIG/GGG thin films with *x*=0.1 and 0.3 compared to that for $Y^{3+}$ site in YIG data. In YIG, the distances of between the nearest $O^{2+}$-$Y^{3+}$, $O^{2+}$-$F^{3+}$ in the tetrahedral site and $O^{2+}$-$Fe^{3+}$ in the octahedral site are ~ 2.4 Å, 1.87 Å and 2 Å, respectively. The Ca-O distance found to be ~2.4 Å indicating that it is on $Y^{3+}$ sites. There was a reduction in the intensity of Ca:YIG films spectra due to the lattice disorder, which is a result of the different sizes of the $Ca^{2+}$ and $Y^{3+}$ ions. This clarifies the reason of the decrease in the amplitude with higher $Ca^{2+}$ concentration, which is due to the different numbers of Ca atoms nearby that are distorting the lattice.

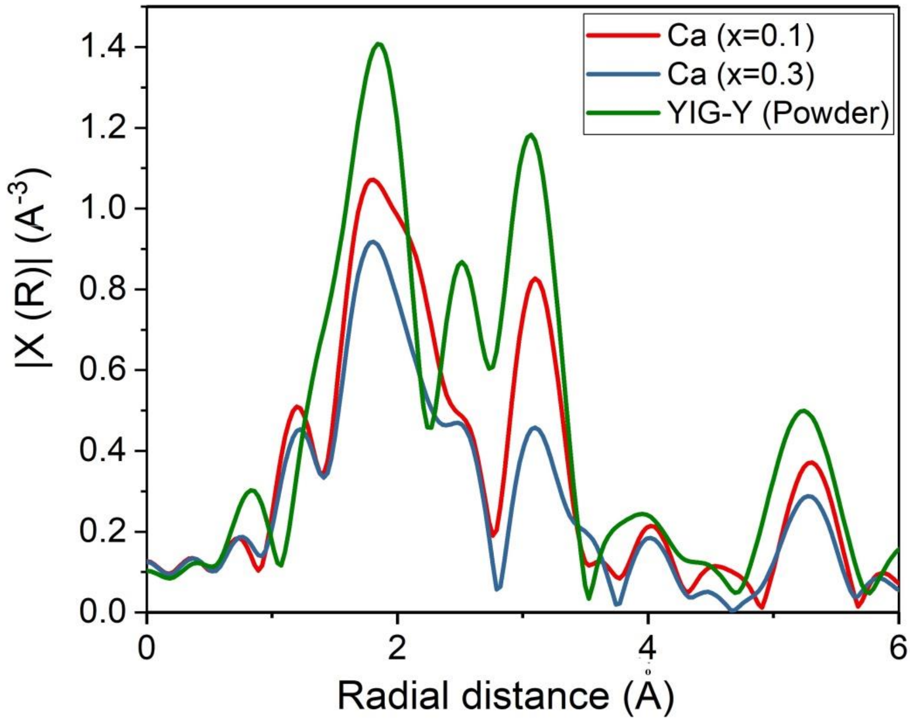

Figure 6.9: The EXAFS spectra of Ca:YIG/GGG of *x*=0.1 and 0.3 compared to $Y^{3+}$ in YIG powder.

The XRD, EXAFS and XANES spectra suggest that the Ca ions occupied Y-sites in YIG phase leads to some lattice mismatch due to the size difference between $Ca^{2+}$ and $Y^{3+}$. In addition, shifting in the near edge absorption spectra to smaller energy suggested the presence of $Fe^{2+}$ ions. There was no evidence of $Fe^{4+}$ in these films.

### *6.3.3 Magnetic properties:*

The *M-H* hysteresis loops for Ca:YIG thin films on GGG substrates were measured using SQUID magnetometer for different Ca concentrations. A magnetic field of up to ±1000 Oe was applied parallel to the surface of the films. The paramagnetic signal of the GGG substrates was subtracted from the results. The loops were compared to the pure YIG/GGG thin film, which was grown in same conditions (see §5.3.3). The results show that $M_s$ decreased with increasing $Ca^{2+}$ concentration (fig. 6.10). This decrease is about 18% for $x$=0.05 ($M_s$=118 emu/cm$^3$), 34% for $x$=0.1 ($M_s$=94 emu/cm$^3$), 45 % for $x$=0.2 ($M_s$=78 emu/cm$^3$) and 52% for $x$=0.3 ($M_s$=69 emu/cm$^3$). Although the non-magnetic $Ca^{2+}$ ions substituted non-magnetic $Y^{3+}$ ions on dodecahedral *c*-sites of YIG, the magnetisation dropped. From the XANES measurement (§6.3.2), all the films contain about 5% $Fe^{2+}$ ions, hence; the chemical formula of the films is:

$$Y^{3+}_{3-x}Ca^{2+}_{x}Fe^{3+}_{5-y}Fe^{2+}_{y}O^{2-}_{12-(\frac{x+y}{2})}$$

This formula clarifies that there are some oxygen ions missing from the films. The oxygen vacancies are dependent on Ca concentration and increase with increasing *x*. These oxygen vacancies, in addition to the $Fe^{2+}$ ions, reduced the magnetisation. If $Fe^{2+}$ ion changes coordinates to $Fe^{3+}$ ion one in the presence of oxygen ion mediating them, then there will be a weak double exchange interaction between these ions. This interaction is called “biquadratic exchange”. There is no mobile electron in this interaction. Therefore, the resistivity measurements showed that all films have resistivity more than 2000 Ωcm, which is the maximum value of the equipment that was used. Another reason for this behaviour could be the difference in the structure of these films due to the difference in the radius of $Ca^{2+}$ and $Y^{3+}$ ions that increase the lattice strain in the film, which was mentioned earlier in §6.3.2. $H_c$

of the films increased slightly with increasing the $Ca^{2+}$ concentrations as shown in table 6.3, which is expected behaviour due to increase the strain.

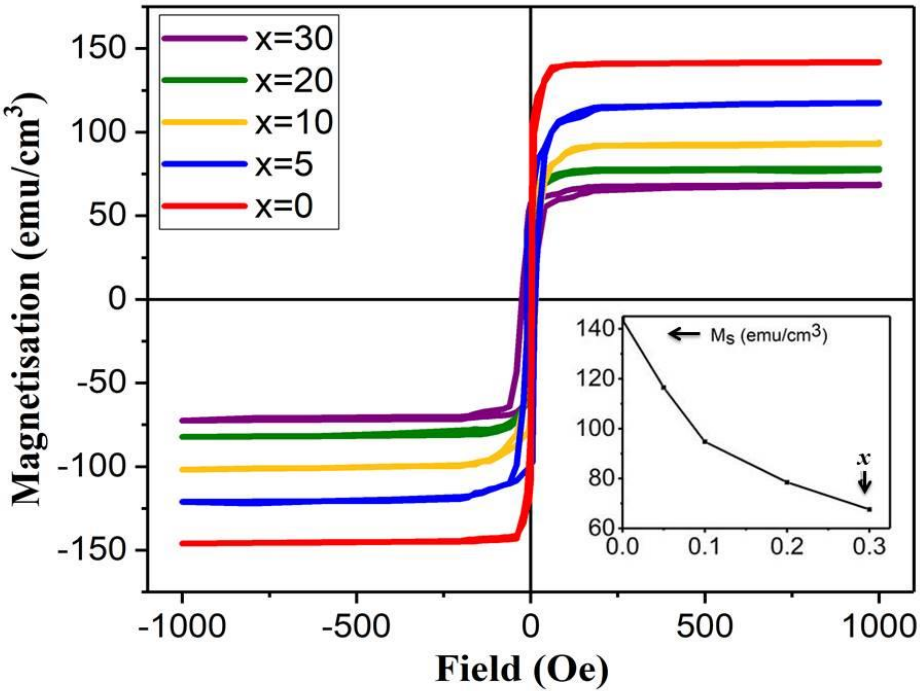

Figure 6.10: *M-H* hysteresis loops for Ca:YIG/GGG at different concentrations of Ca compared with pure YIG, at *T*=300K. The paramagnetic contribution of GGG has been subtracted. The inset shows the decrease of $M_s$ with Ca concentration.

Table 6.3: The magnetic properties of Ca:YIG at temperature of 300 K.

| ***Film No.*** | ***x*** | **$M_s$** (emu/cm$^3$) | **$H_c$** (Oe) |
|---|---|---|---|
| YIG/GGG | 0 | 143 ±0.1 | 0.7 ±0.01 |
| Ca:YIG/GGG | 0.05 | 118 ±0.4 | 9 ± 0.2 |
| Ca:YIG/GGG | 0.1 | 94 ±0.3 | 12 ±0.1 |
| Ca:YIG/GGG | 0.2 | 78 ±0.1 | 14 ±0.3 |
| Ca:YIG/GGG | 0.3 | 69 ±0.2 | 16 ±0.4 |

The *M-H* loops of Ca:YIG thin films on YAG substrate with *x*= 0.05 and 0.1 were measured at 300 K and is shown in fig. 6.11. The results were compared to pure YIG/YAG thin films. The magnetic measurements on Ca:YIG/YAG thin films with different Ca concentrations showed different behaviour when measured at any specific temperature and applied magnetic field. This was suggested by previous studies [18, 19] to be due to the multiphase nature of the film structure. This is mainly related to the high strain between the film and the substrate, which gives poor film crystallinity and leads to magnetic disorder of the grain boundary. Therefore, the interaction between the film and the substrate is an important factor that affects forming the preferred structural and magnetic properties.

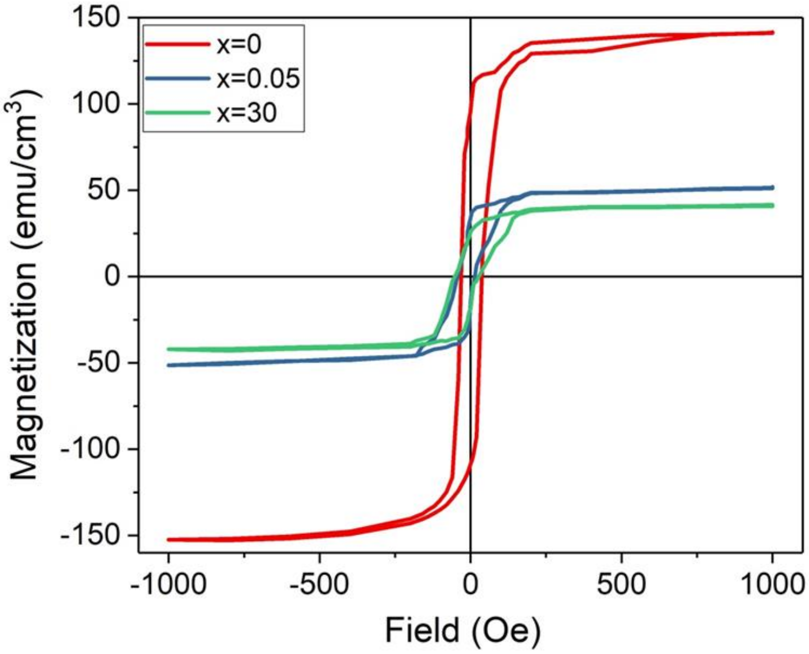

Figure 6.11: M-H loops of Ca:YIG/YAG with x=0.05 and 0.3 at 300 K compared with pure YIG/YAG thin film. The diamagnetic contribution of YAG substrates was subtracted.

The magnetisation as a function of the temperature change was measured for Ca:YIG/GGG thin films with *x*= 0.1 and 0.3. The temperatures used were 300, 140 and 70 K. Measurement at temperatures lower than 70K were not possible with the current SQUID capabilities due to the paramagnetism of the GGG substrate below this temperature and hence no *M-H* loops could be produced even if the GGG effect was subtracted. Figure 6.12 shows the effect of the temperature on the magnetisation for Ca:YIG/GGG $x$=0.1. $M_s$ was about 94 emu/cm$^3$ and when the temperature decreased to 140 K; $M_s$ increased to about 120 emu/cm$^3$. This behaviour is expected for ferrimagnetic YIG. In pure YIG, the magnetisation increases by about 22% between 300K and 140 K and with this film is about 23%. However, when the temperature drops to 70K, the magnetisation decreases slightly to $M_s$ ~ 115 emu/cm$^3$. However, in pure YIG the magnetisation increased to about 40% at 70 K compared to the magnetisation at 300 K, as shown in fig. 5.15. This suggests that there is a specific temperature between 140 and 70 K where the magnetisation starts dropping with decreasing the temperature. $H_c$ show slightly increasing from 12, 14 and 17 Oe, when the temperature decreased from 300, 140 and 70, respectively. This is unexpected behaviour because the magnetocrystalline anisotropy highly increased when temperature drops. This small reduction in $H_c$ could be due to the frustration Fe$^{2+}$.

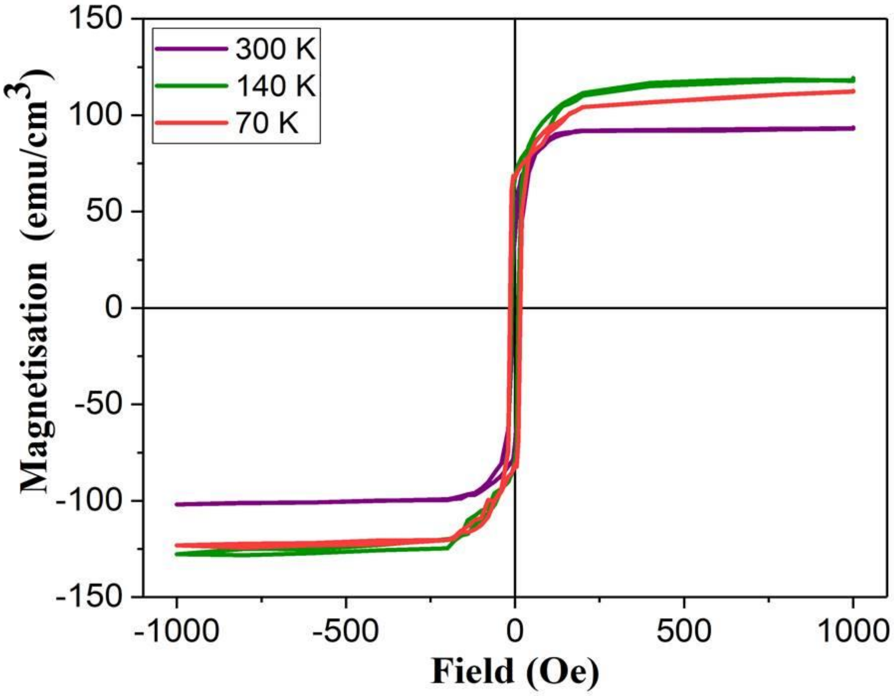

Figure 6.12: The M-H loops for Ca:YIG/GGG with $x$=0.1. The paramagnetic contribution of GGG has been subtracted

Figure 6.13 shows the magnetisation at temperatures of 300, 140 and 70 K of Ca:YIG/GGG *x*=0.3. $M_s$ at 300 K is 69 emu/cm$^3$. When the temperature decreased to 140 K; the magnetisation increased by about 21% to 83 emu/cm$^3$, which is also the same behaviour of pure YIG/GGG (fig. 5.15). However, when the temperature dropped to 70 K, the magnetisation went down to 43 emu/cm$^3$. This $M_s$ is lower than $M_s$ at 300 K, which means the magnetisation of the film drops at a temperature close to 140 K. Figure 6.14 shows the different in the magnetisation between pure YIG/GGG, Ca:YIG/GGG *x*=0.1 and *x*=0.3 thin films as a function of temperature.

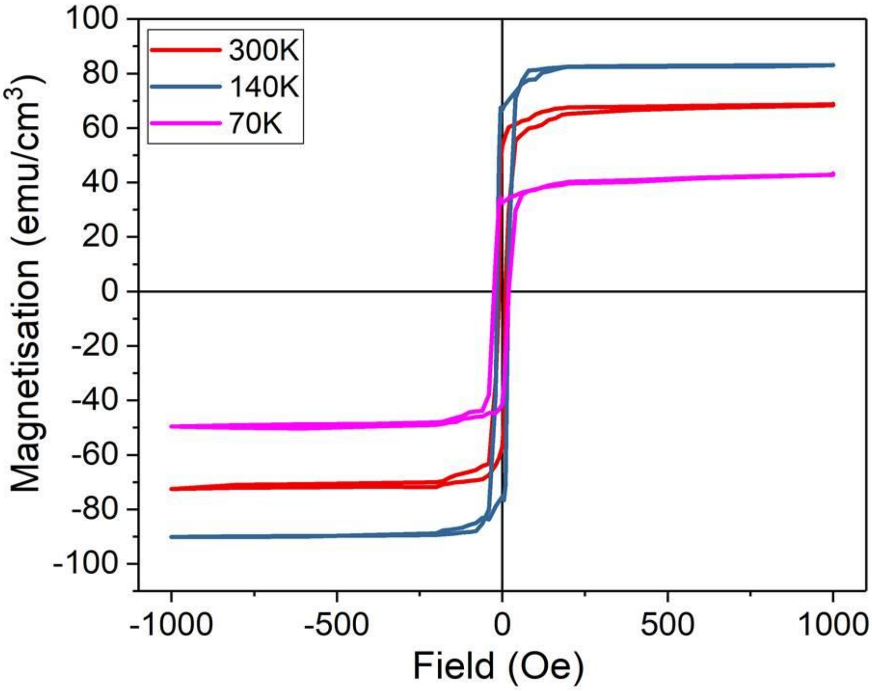

Figure 6.13: The M-H loops of Ca:YIG/GGG with *x*=0.3. The paramagnetic contribution of GGG has been subtracted.

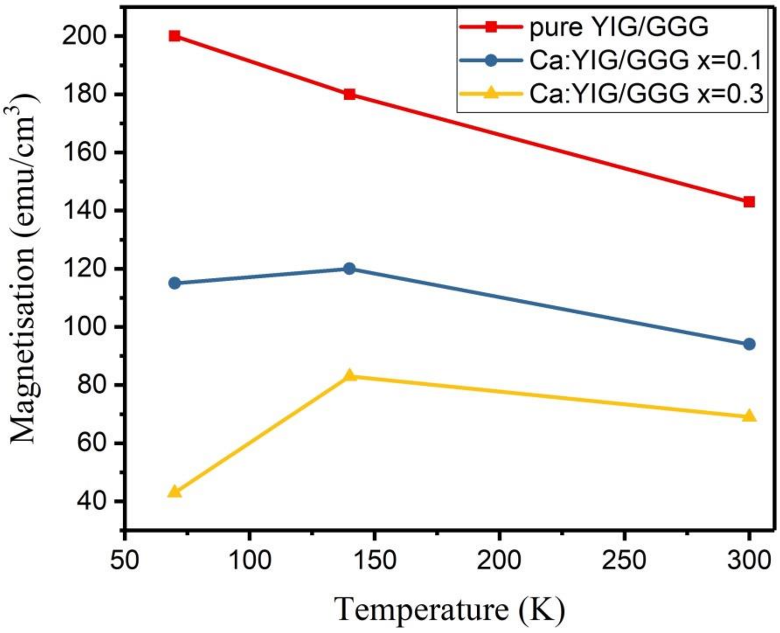

Figure 6.14: the change in the magnetisation as a function of temperature for pure YIG/GGG, Ca:YIG/GGG *x*= 0.1 and Ca:YIG/GGG *x*=0.3 thin films.

This reduction of $M_s$ was also reported by Thavendrarajah *et al* but their effect was smaller [20]. They showed that Ca$^{2+}$ ions substituted Y$^{3+}$ ions, extra holes were introduced and they are likely to have a weak bond with the Ca$^{2+}$ ions at high temperature. If the temperature decreases, the holes will start to be localized and form Fe$^{4+}$ ions on the tetrahedral *d*-sites. These localizations are assumed to set on the tetrahedral sites due to small Fe$^{4+}$ ion compared to Fe$^{3+}$ ions. Therefore, Fe$^{4+}$ ions assumed to form a magnetic sublattice that has same crystal symmetry of tetrahedral *d*-site [19]. However, these Fe$^{4+}$ ions will have a ferromagnetic superexchange coupling with the Fe$^{3+}$ ion in the octahedral *a*-site. This is because the Fe$^{4+}$ ion has less than half-filled $3d^4$ shells, while Fe$^{3+}$ ion has a half-filled $3d^5$ shell. It was demonstrated earlier in §5.2 that the magnetisation of pure YIG is due to strong antiferromagnetic interaction between the Fe$^{3+}$ on *a*-sites and *d*-sites. The defect induced ferromagnetic interaction destroys the long range interactions. However, for Ca:YIG the magnetisation was reduced due to two reasons. Firstly, the formation of Fe$^{4+}$ ions in the tetrahedral *d*-site and secondly, the magnetic moments of Fe$^{4+}$ align antiparallel to the Fe$^{3+}$

ions in the tetrahedral sites. However, the films present in this study have not seen any $Fe^{4+}$ ions and have shown high resistivity with high reduction in the magnetisation. This could be due to the presence $Fe^{2+}$ ions, which were present as paramagnetic ions. This behaviour increases with reducing the temperature down to 0 K when these ions become highly frustration. A higher reduction in the magnetisation of the film with $x$=0.3 compared to the film of $x$=0.1 was observed since the concentration of oxygen vacancies increased with increasing Ca concentration.

The magnetic characterization of Ca:YIG thin films agreed with the structural analysis. The magnetisation of Ca:YIG thin films decreases with increasing $Ca^{2+}$ ion concentration due to formation of frustration $Fe^{2+}$ ions in the tetrahedral sites of YIG. The oxygen vacancies increase with increasing $Ca^{2+}$ ion amount. $Fe^{2+}$ ion starts to be strong paramagnetic under certain temperature near 0 K, which depends also on $Ca^{2+}$ ion concentration.

### *6.3.4 Magneto optical properties:*

MCD spectra of Ca:YIG thin films with different $Ca^{2+}$ concentration were measured using Faraday geometry as a function of the change in energy, which varied between 1.5-4 eV. The MCD spectra were performed with applied magnetic field of ±5000 Oe out of plane. The films were set on vacuumed cryostat. The signal of the cryostat window and the substrates were subtracted from all results. Figure 6.15 shows the MCD spectra as a function of energy for Ca:YIG/GGG thin films with $Ca^{2+}$ concentrations of 0.05, 0.1 and 0.2 and compared to the MCD of pure YIG/GGG thin films. These measurements were performed at room temperature. The MCD spectra of Ca:YIG/GGG thin film are close to the spectrum of pure YIG/ GGG thin films at the energy between 1.5- 3.4 eV. All the films show three features transitions. The positive paramagnetic feature at energy of ~2.75 eV represents the transition of the octahedral $Fe^{3+}$ ions of $^6A_{1g}$ ($^6S$) – $^4T_{2g}$ ($^4D$). This transition has similar MCD intensity for all Ca:YIG/GGG films and is slightly higher in the pure YIG/GGG thin films. The negative signal at energy of 3.1 eV indicates a biexciton transition. The features showed a shift in energy when the Ca concentration increased. This shift is due to the increase in lattice constant, as shown in fig. 6.16. These features showed a decrease in the MCD negative signal with increasing the $Ca^{2+}$ concentrations. This reduction in the bixciton transition could be occurred due to two reasons; the number of oxygen vacancies increased with increasing the $Ca^{2+}$ ion concentation and due to $Ca^{2+}$ ion substituting $Y^{3+}$ ion, which resulted in frustration $Fe^{2+}$ ions. That is because the targets that used in Ca:YIG films did not have enough oxygen for Ca:YIG. The oxygen pressure that was used could be less than this reduction. Therefore, this lack of oxygen was going to form some of $Fe^{3+}$ ions into $Fe^{2+}$ ions with sufficient oxygen vacancies.

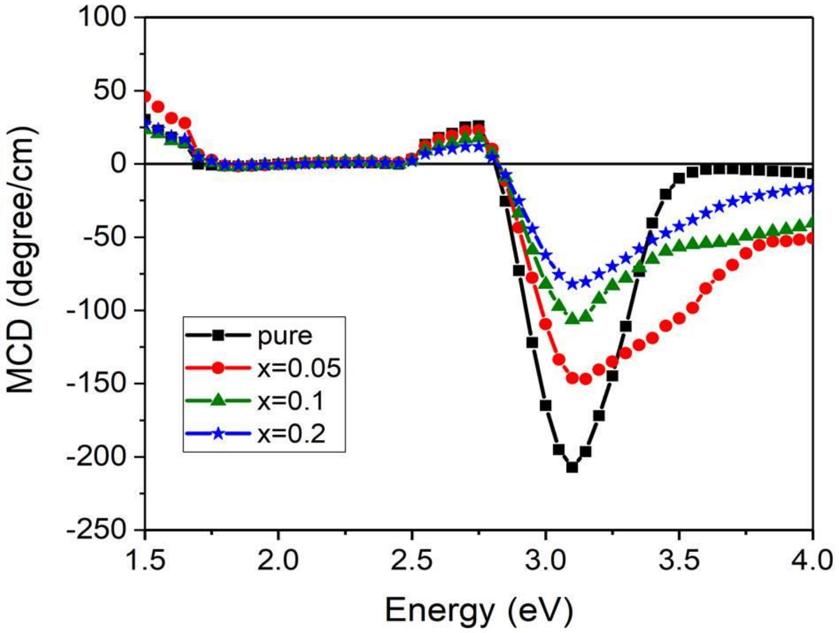

Figure 6.15: The MCD spectra for of Ca:YIG/GGG films with *x*=0, 0.05, 0.1 and 0.2 at room temperature and with applied magnetic field of ±5000 Oe.

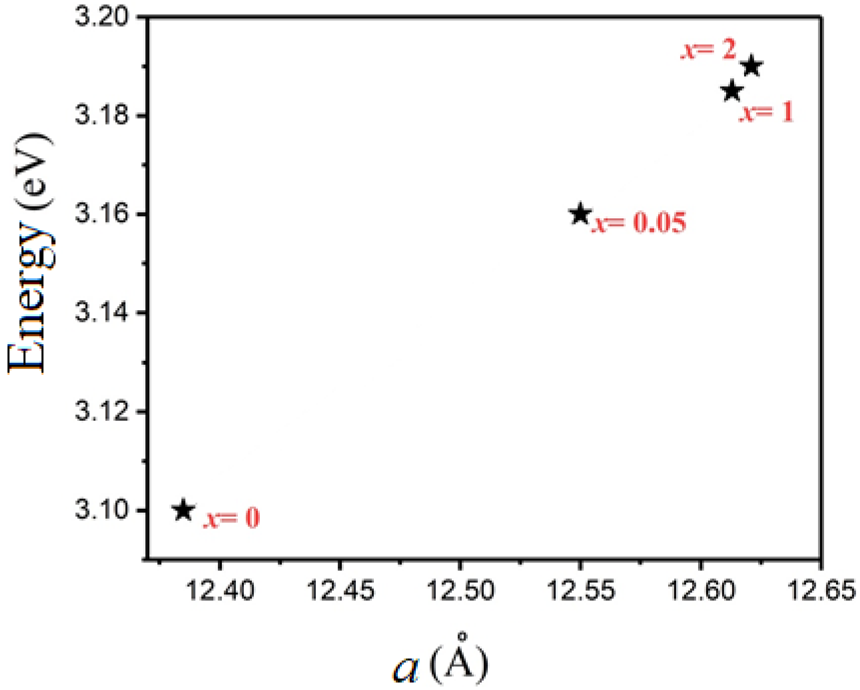

Figure 6.16: the shifting amount of energy 3.1 eV for MCD peaks of transition as a function of lattice constant for Ca:YIG/GGG thin films with different Ca concentration (*x*).

Another reason is the superexchange interaction between $Fe^{2+}$ and $Fe^{3+}$ is ferromagnetic. In addition, there was no change in the band tranistion of $^6A_{1g}$ ($^6S$) – $^4T_{1g}$ ($^4G$) at energy of 1.5 eV. However, the behaviour of MCD for all Ca:YIG films between 3.5-4 eV is unexcepted because they are not monotronic and not understood clearly yet, but could be due to the strong absorption at E >3.5 eV, which makes the MCD unreliable at this energy value.

Figure 6.17 shows the MCD spectra of Ca:YIG/GGG thin films with different $Ca^{2+}$ ion concentrations at temperature of 10 K compared to the MCD of pure YIG/GGG thin film measured at same temperature. The MCD features at 1.5 and above 3.4 eV became a shoulders. However, the feature at 3.1 eV is shifted slightly to 3.2 eV with the $Ca^{2+}$ ion. The intensity of the peaks also showed an decrease with increasing the $Ca^{2+}$ ion concentrations. This decreasing in intensity is due to increase the oxygen vacancies and the frustrated $Fe^{2+}$. The absorption of the films increased with decreasing the temperature.

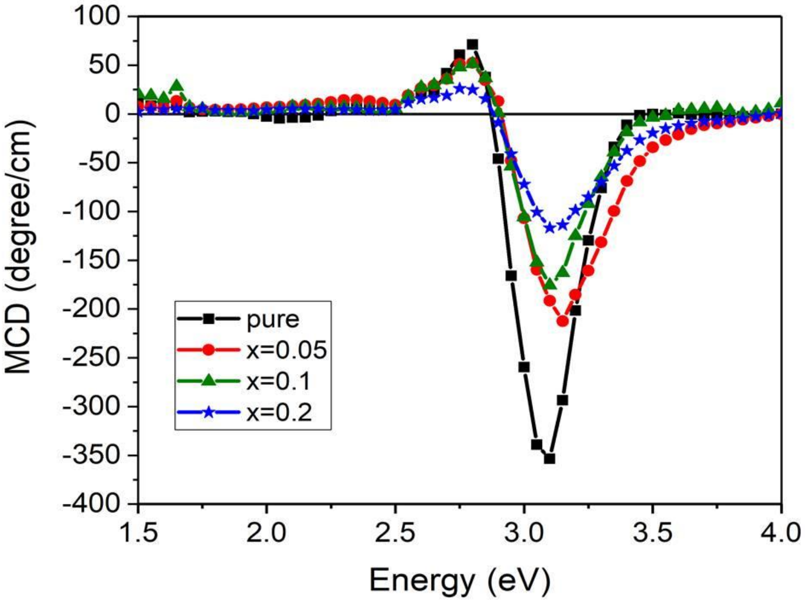

Figure 6.17: The MCD spectra for of Ca:YIG/GGG films with *x*=0, 0.05, 0.1and 0.2 at 10 K and with applied magnetic field of ±5000 Oe.

The MCD spectra of Ca:YIG thin films with different $Ca^{2+}$ concentrations on YAG substrates were measured at room temperature and compared to the MCD spectrum of pure YIG/YAG thin film. Ca:YIG/YAG films have multi-phase *M-H* loops fig.6.11. Therefore, the mixture has different material that affected the MCD results, which makes the data not reliable as much as pure YIG/YAG films, as shown in fig. 6.18.

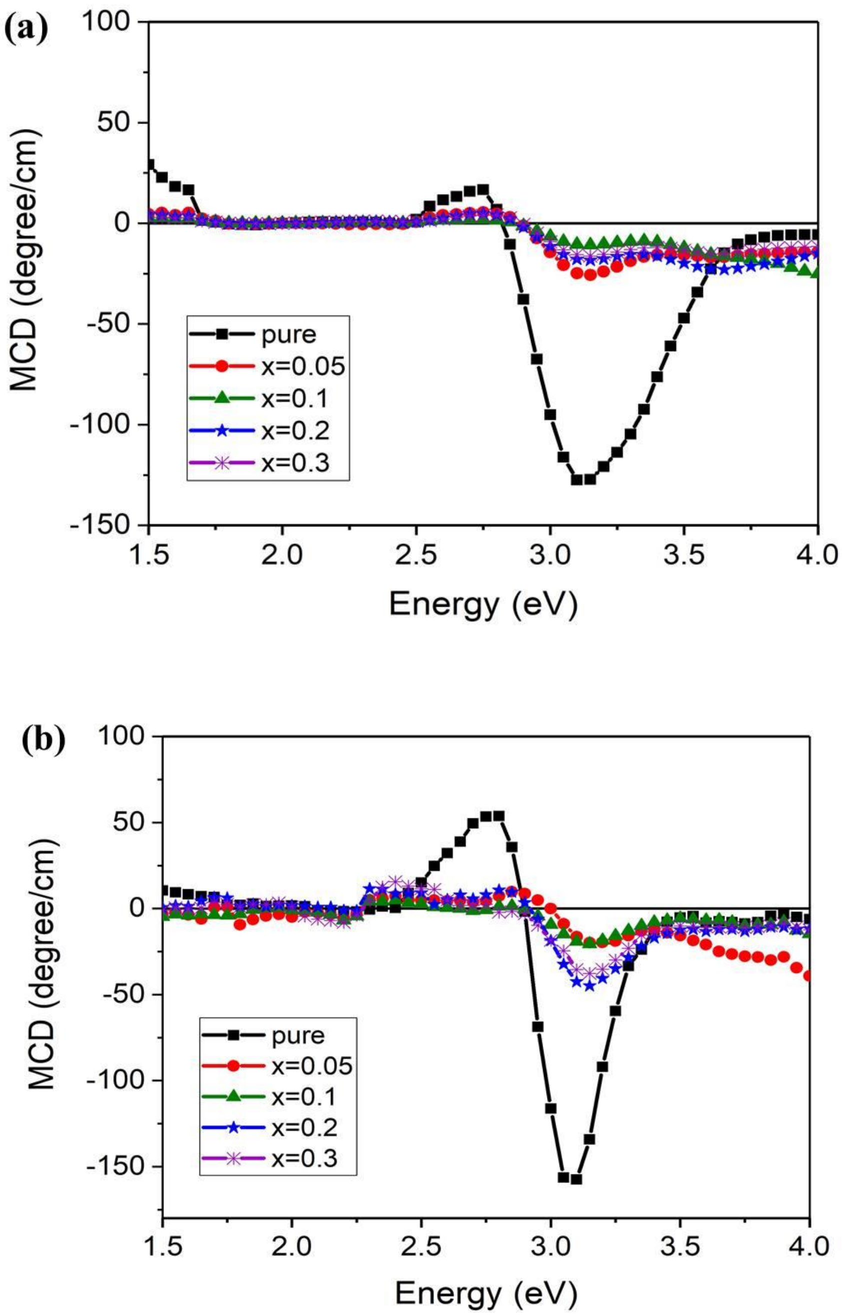

Figure 6.18: The MCD spectra for of Ca:YIG/YAG films with *x*=0, 0.05, 0.1and 0.2 with applied magnetic field of ±5000 Oe at temperature of (a) room temperature and (b) 10 K.

The MCD measurements detected the compensation of $Ca^{2+}$ ions in Ca:YIG thin film. The Ca doped YIG produced a broad band spectra in near infra-red region. However, the low temperature of the MCD show a high effect above 3.4 eV, whereas the absorption increased of Ca:YIG/GGG films, as shown in fig 6.17.

## 6.4 Conclusion:

The possibility of growing Ca:YIG thin films by PLD technique was investigated. Ca:YIG thin films were grown with different $Ca^{2+}$ concentrations (*x*= 0.05, 0.1, 0.2 and 0.3) on GGG and YAG substrates. The XRD spectra revealed a shift in the peaks of YIG to lower 2θ angles. This shift increased with increasing the $Ca^{2+}$ concentration. Accordingly, the lattice strain also increased up to 2.03 for Ca:YIG/GGG (*x*=0.3) thin film, whereas it became 2.1 for Ca:YIG/YAG (x=0.3) thin film. The higher strain for the films grown with YAG substrate is due to the larger mismatch between Ca:YIG film and YAG substrate. The EXAFS measurements indicated that all the films have a good fit with $Fe^{3+}$ ions of YIG with small shift toward $Fe^{2+}$ ions. It also suggests that $Ca^{2+}$ ions of Ca:YIG thin films substituted for $Y^{3+}$ ions of YIG.

The magnetic properties of the films revealed a reduction in the magnetisation with increasing the $Ca^{2+}$ concentration due to the appearance of $Fe^{2+}$ ions in the tetrahedral sites with oxygen vacancies. In addition, the magnetisation of Ca:YIG thin films as a function of temperature was found to decrease at lower than a specific temperature. This behaviour was explained to be a result of the frustration due to $Fe^{2+}$ ions and the oxygen vacancies that led to the decreased magnetisation. The temperature that marks the magnetisation drop is dependent on the $Ca^{2+}$ concentration. When the Ca concentration increased; the number of oxygen vacancies also increased.

This work also focused on exploring the contribution of non-magnetic $Ca^{2+}$ ions to the magnetisation in order to explain the change in magnetisation of ferrimagnetic materials when doped with non-magnetic ions. It revealed that non-magnetic $Ca^{2+}$ ions substituted non-magnetic $Y^{3+}$ ions, which affected the magnetisation by the appearance of paramagnetic iron $Fe^{2+}$ ions, which are frustration, and oxygen vacancies.

The magneto optics measurements showed a high negative signal of MCD band spectra at 3.1 eV, which referred to biexciton transition. The intensity of this transition found to decrease with increasing the $Ca^{2+}$ concentration due to the presence of $Fe^{2+}$ ions and oxygen vacancies. The MCD intensity increased with the reduction of the temperature and showed a different behaviour from room temperature above 3.4 eV. The magnetic and magneto optics measurements together demonstrated that the magnetisation behaviour of Ca:YIG thin films is affected by the formation of $Fe^{2+}$ ions at the tetrahedral sites, which determines the magnetic properties of the material.

## 6.5 References:

1- Pardavi-Horváth, M., Wigen, P. E. and G. Vértesy. *Journal of Applied Physics* **63.8** (1988): 3110-3112.

2- Thavendrarajah, A., Song, Y. and P. E. Wigen. *Journal of applied physics* **70.10** (1991): 6389-6391.

3- Pardavi-Horvath, M., *et al. IEEE Transactions on Magnetics* **23.5** (1987): 3730-3732.

4- Song, Y. J., *et al. Journal of magnetism and magnetic materials* **154.1** (1996): 37-53.

5- D'Amico, A., and P. De Gasperis. *Journal of Applied Physics* **53.11** (1982): 8225-8227.

6- De Gasperis, P. and A. D'Amico. *Applied Physics Letters* **42.1** (1983): 111-113.

7- Gehring, G. A., *et al. Physica status solidi (b)* **243.1** (2006): 255-258.

8- Milani, E., and P. Paroli. *Journal of magnetism and magnetic materials* **72.2** (1988): 209-214.

9- Bornfreund, R. E., and P. E. Wigen. *Journal of applied physics* **79.8** (1996): 5191-5192.

10- Song, Y.J. Ph.D. Thesis, the Ohio State University (1993).

11- Pardavi-Horvath, M., *et al. Journal of Applied Physics* **63.8** (1988): 3107-3109.

12- Lehmann-Szweykowska, A., *et al. Physical Review B* **43.4** (1991): 3500.

13- Kucera, M., *et al. Le Journal de Physique* IV **7.C1** (1997): C1-709.

14- Kučera, M., *et al*. *Journal of magnetism and magnetic materials* **157** (1996): 323-325.

15- Turpin, G. B., *et al*. *Journal of applied physics* **81.8** (1997): 4872-4874.

16- Al-Omari, I. A., Skomski, R. and D. J. Sellmyer. *Advances in Materials Physics and Chemistry* **2** (2012): 116-120.

17- Chen, Fu, *et al*. *Scientific reports* **6** (2016): 28206.

18- Popova, E., *et al*. *Journal of Applied Physics* **90.3** (2001): 1422-1428.

19- Cerijem *et al*. *Materiali in tehnologije* **47.1** (2013): 59-63.

20- Thavendrarajah, A. Ph.D thesis, Ohio State University, (1992).

# 7. Summary and Future Recommendations.

## 7.1 Summary:

This study focused on preparing magnetic oxides thin films using pulsed laser deposition technique (PLD), which is a line of research that the University of Baghdad is trying to establish. The preparation of high quality and lower cost of iron oxides, YIG and Ca:YIG thin films were investigated. The structural properties of these films were examined by x-ray diffraction and extended X-ray absorption fine structure (EXAFS) measurements, while superconducting quantum interference (SQUID) was used to measure their magnetisation. Faraday geometry was used to characterise the magneto-optical properties through magnetic circular dichroism (MCD) spectra.

The studies revealed that it is possible to control the PLD conditions in order to produce the required composition of the thin films. These conditions include: the oxygen pressure, the annealing temperature for the target and the film, the doping elements and the substrate type. These conditions could control the number on iron valences of the film. For example, an oxygen pressure higher than 400 mTorr is likely to lead to produce YIG films with pure amount of $Fe^{3+}$ iron ion due to reduce the number of oxygen vacancies in the films hence; a magnetisation close to the bulk YIG. This is accompanied by a low amount of lattice strain. The simultaneous and non- simultaneous variation of these conditions can lead to substantially different structural, magnetic and magneto-optical and electronic properties.

**Iron oxides** thin films were prepared at different oxygen pressures and from two targets that were annealed at different temperatures and oxygen pressure of range 0.03 (base) – 100 mTorr. The data obtained from this study showed that an annealing temperature of the target at 500 °C will produce a higher presence of $Fe_3O_4$ phase, which transforms into $\gamma$-$Fe_2O_3$ phase at an oxygen pressure higher than the base values up to more than 100 mTorr. This is a direct consequence of the formation of $Fe^{3+}$ ions in $\gamma$-$Fe_2O_3$. That was useful for forming YIG, which contains $Fe^{3+}$ ions. On the other hand, increasing the annealing temperature of targets to up to 1200 °C will increase the content of the FeO phase in the films produced at base pressure. That means the majority of the iron in the film is $Fe^{2+}$ ions. Increasing the oxygen pressure to higher levels than base pressure is likely to increase the content of the $Fe_3O_4$ phase in these films but no transformation into $\gamma$-$Fe_2O_3$ phase was observed. The results also showed that the lattice structure of sapphire substrates have a significant mismatch with all iron oxides, which leads to a drop in $M_s$ for the film contains both $\gamma$-$Fe_2O_3$ and $Fe_3O_4$ phases. This was also evidenced by an exchange bias in films with higher $Fe_3O_4$ than $\gamma$-$Fe_2O_3$ content. In addition, some films showed a decrease in $M_s$ with temperature due to the present of an amount of canted antiferromagnetic $\alpha$-$Fe_2O_3$ phase on it. However, the films that contained $Fe_3O_4$ showed a Verwey transition $T_V$ close to this in bulk magnetite. The MCD spectra showed a high two features at energies of 2.2 eV and 3.2 eV for the films that contained $Fe_3O_4$, whereas the films contain $\gamma$-$Fe_2O_3$ showed one transition feature at energy of 3.2.

YAG and GGG substrates were used in **YIG** thin films deposition at different oxygen pressure in order to test their suitability in terms of the amount of lattice strain at the interface with YIG phase. A high lattice strain in YIG phase was observed when deposited on YAG substrates. This strain is a direct consequence of the lattice mismatch between the two phases. On the other hand, YIG thin films deposited on GGG substrates noticed a significantly lower lattice strain compared to YIG films deposited on YAG films. The composition of YIG on GGG films showed a strong dependence on the oxygen pressure in the PLD chamber. For example, films grown at an oxygen pressure of 100 mTorr showed a presence of metallic iron $Fe^0$, while an increased in $H_c$ of YIG phase was observed when using an oxygen pressure of 500 mTorr. The most suitable oxygen pressure for producing high quality YIG on GGG thin films was found to be 400 mTorr, which had a structural, magnetic and magneto optical properties close to the bulk YIG.

**Ca:YIG** thin films were grown on GGG and YAG with different Ca concentrations ($x$=0.05, 0.1, 0.2 and 0.3). These films were prepared at an oxygen pressure of 400 mTorr and an annealing temperature of 1000 °C. The structural and magnetic properties of Ca:YIG thin films on GGG substrates showed a strong dependence on the $Ca^{2+}$ concentration and are likely to have a higher number of oxygen vacancies increased with increasing the Ca concentrations. The higher amount of oxygen vacancies led to a higher lattice strain, a lower $M_s$ and a higher amount of frustration $Fe^{2+}$ ions in the tetrahedral site. The EXAFS measurements for the film indicated that the $Ca^{2+}$ ions are successfully occupied on dodecahedral sites instead of $Y^{3+}$ ions. The XANES detected an amount of 5% $Fe^{2+}$ ions for all films. The films were grown on YAG substrates showed high lattice strain. These films have multi-phase component that made the magnetic and MCD measurements are unreliable.

This work focused on improving the understanding of the effect of the processing conditions of PLD technique on the quality of YIG and Ca:YIG thin films. The combination of thins films fabrication and characterisation techniques was used to study the effect of these conditions on the films produced. It was found that the oxygen pressure is the most significant parameter in the deposition of Ca:YIG thin films. It determines the amount of oxygen vacancies in the produced film, which can directly affect $M_s$ of these films. In addition, the choice of the substrates can vital in reducing the amount of lattice strain in the produced film. Finally, the annealing temperature of thin films determines the amount of YIG in the produced films. These insights are essential for choosing the suitable conditions of PLD process needed for depositing Ca:YIG thin films with most preferred properties.

## 7.2 Future work:

The combination of PLD and the characterization techniques used in this work can be extended to perform further analysis of YIG and Ca:YIG thin films, which could be interesting for future research. The use of XRD and EXAFS provided a valuable tool to identify the main constituent phases in the produced films, while the use of SQUID to measure $M_s$ and Zero field cool/field cool (ZFC/FC) supported the structural and composition analysis of the films. These measurements are essential to understand the results of magneto optics and conductivity characterisation. This research approach can be extended to include further studies on magnetic oxides. In this sense, further research objectives have been proposed, which can be divided into two main groups:

1) Measurements at the University of Sheffield:
    - YIG thin films are important in spintronics and magnonics applications. These applications require YIG thin film with small damping. Measuring the damping for our films will be interesting to know if the damping is close to bulk YIG similar to other properties. The damping could be measured by ferromagnetic resonance (FMR) technique with antenna of spectra under microwave.
    - The resistivity of Ca:YIG thin films was difficult to investigate during this study due to high resistance of the films. We tried to measure the resistivity of the films without any success to find equipment that is measuring the resistance more than 20x $10^9$ Ω. Hence, it will be interesting to study the

behaviour of the resistivity as a function of the change in temperature and investigate the charge carriers of Ca:YIG thin films.

2) Measurements at the University of Baghdad, which can include:
    - Using Raman spectroscopy investigate the crystal structure of target **B** films.
    - Studying spin Hall Effect of Pt films grown on YIG films and investigate their magnetoresistance.
    - Enhanced Ca:YIG films can be grown using PLD with different concentrations and an oxygen pressure higher than the pressure was used in this study. The properties of these films will be investigated and compared with the results obtained from Ca:YIG thin films.